TO DR. SHELDON A. JOHNSON :

Dr. Sheldon A. Johnson and Mrs. Carrie W. Rudolf deserve special thanks for serving on my committee and advising me through the completion of my work.

FROM

HASAN MURSHED

4.19.93

HETEROGENEITY DOSE CORRECTION:

A DOSIMETRIC ANALYSIS OF EXTERNAL PHOTON IRRADIATION

A Thesis

Submitted to the Graduate Faculty of the
Louisiana State University and
Agricultural and Mechanical College
in partial fulfillment of the
requirements for the degree of
Master of Science

in

The Nuclear Science Center

by
Hasan Murshed
M.B.,B.S., University of Dhaka
May 1992

Dedicated to

all cancer patients

ACKNOWLEDGMENTS

It has been a very good experience for me at the LSU Nuclear Science Center and Mary Bird Perkins Cancer Center while undergoing my master's program in nuclear science, in the medical radiation sciences option. I have met all of the most wonderful people of my life, who, through their care, support, and encouragement kept me motivated through long hours of working on this thesis project. Their kindness and concern will not be forgotten.

My most sincere gratitude goes to my major professor, Dr. Oscar Hidalgo-Salvatierra, for whom no amount of thanks would be enough. It has been a most fortunate opportunity for me to work under his guidance for my thesis project. His interest, time and counseling given to me in my project is immeasurable. The many occasions of academic and non-academic discussions with him kept me active and stimulated my thesis work throughout. As I complete this thesis, I realize that at some point in our relationship, he surpassed the mere role of being major professor and became true mentor. I hope to enjoy many more years of friendship and guidance from him in the future.

I am also very fortunate to have Dr. Ronald M. Knaus on my committee, under whom I studied the very basics of radiation biology. The immense interest he took in my project is beyond all special thanks. He was not only my teacher but also a true and caring friend. His help in my academic studies and beyond will always be cherished in my memory.

Very special thanks go to Dr. Kenneth K. Lo, who helped me keep this project properly focused, and always found time for advising me whenever necessary. Dr. Sheldon A. Johnson and Mrs. Carrie W. Rudolf deserve special thanks for serving on my committee and advising me through the completion of my work.

One of the most unique persons I have ever met is Mr. Mike Martin, President and CEO of MBPCC. Mr. Martin kept me confident and motivated, and always advised me very properly in many aspects of life. I would like to take this opportunity to thank him for being there whenever I needed him.

John Paul Luckett, Jr. deserves very special thanks for being one of the most wonderful friends I have ever had, always teaching and encouraging me, as a true friend does. Ajaye Bloomstone, MBPCC Librarian, helped me with initial and follow-up literature searches which were the starting point of this project. She was also gracious enough to assist me while writing this thesis. I will never be able to thank her for her time and encouragement. Will Hall took a great deal of interest and also used his expertise to help build my lung phantom; a very special thanks to him. I would also like to thank Ms. Yvonne Thomas, whose typing expertise helped me finish this thesis.

Finally, I would like to thank the entire staff of MBPCC for their continuous encouragement and support during my entire internship. I would like to thank Pat Summers, Penny Culley, Edna Martin, Andrea Guba, Kathy Alello, Audrey Ardoin, C. W. Street, and Nikki Casanova. Along with many others, their help, encouragement and care will always be remembered. I hope to enjoy the best there is with all of them for many more years to come.

TABLE OF CONTENTS

Page

DEDICATION ii

ACKNOWLEDGMENTS iii

LIST OF TABLES vii

LIST OF FIGURES viii

ABSTRACT xii

INTRODUCTION 1

1. Statements of Problem 1
2. Objectives and Approach 11

MATERIALS AND METHODS 13

1. Phantom Construction 13
   - A) Selection of Materials 13
   - B) Phantom Fabrication 34
   - C) Phantom CT Scan 38
2. Phantom Irradiation Technique 39
3. Thermoluminescent Dosimetry 43
   - A) TLD System Setup 43
   - B) TLD Calibration 50
   - C) TLD Readout and Data Analysis 53
4. Data Generation from Computer 57

TABLE OF CONTENTS, CONTINUED

Page

RESULTS AND DISCUSSION 58
1. 6 MV X-Ray Energy 58
2. 15 MV X-Ray Energy 66
CONCLUSIONS 72
RECOMMENDATIONS 75
REFERENCES 76
APPENDIX A 80
APPENDIX B 117
VITA 125

LIST OF TABLES

Table		Page
1.	Breakdown of elemental composition. Percentage by weight of the RMI plug materials used in the CT phantom to generate the calibration curve of CT number versus relative electron density (relative of water)	19
2.	CT numbers [HU] shown read from different CT scanners and corresponding electron density, relative to water and physical density of various materials used in CT phantom for generating calibration curve of CT numbers versus relative electron density	20
3.	CT numbers [HU] and corresponding relative electron density read from calibration curve, of different materials scanned by inhouse somatom CR CT scanner	23
4.	Patients' mean CT number (HU) and corresponding relative electron density read from the calibration curve	25
5.	Physical and dosimetric properties of water, acrylic, polystyrene, and muscle	28
6.	Listing of average CT numbers [HU] of different regions of a midsagital section from a CT image of lung phantom	42
7.	TMR values for a 5 x 5, 10 x 10 and 20 x 20 cm field for 6 MV x-rays from the Clinac 600C, up to 20 cm depth are shown. All values are normalized to the d_{max} values for the respective field size	44

LIST OF FIGURES

Figure — Page

1. The dose distribution of the supraclavicular field using 4 MV photons. Picture [A] without heterogeneity correction compared to, [B] that after corrected by effective SSD method for heterogeneity . . . 4

2. Picture showing the CT phantom containing the plugs of different materials of known relative electron density, used to generate the calibration curve of CT numbers versus relative electron density. The little white circles are the plugs of simulated lung, hard bone, soft bone and fat. The brown [black in this picture] ring is solid water and the inner white circle is made of acrylic 17

3. Calibration curve, based on CT plugs of known relative electron density. The CT number are read by somatom CR, inhouse CT (MBPCC), mA = 550, KVp = 125. The X-axis shows the relative electron density [ρ_e, medium/ρ_e water] and the Y-axis shows the CT numbers in hounsfield units 21

4. Picture showing some of the materials scanned by inhouse (MBPCC) somatom CR CT scanner, to determine the relative electron density, for simulating lung tissue in the phantom. The materials shown here are different types and grades of cork and some different kinds of woods 22

5. Frequency of patients' mean CT number according to class. Maximum frequency occuring in classes 6 and 7, ranging from -752 (HU) to -841 (HU), and have a mean CT number of -798 (HU) . . . 26

6. Percent TMR in water for field sizes 5 x 5, 10 x 10, and 20 x 20 cm up to 20 cm of depth, for 6 MV x-rays from Clinac 600C 30

7. Percent TMR in polystyrene [the continuous line] and in water [the symbols] for field sizes of 5 x 5, 10 x 10, and 20 x 20 cm up to 20 cm of depth, for 6 MV x-rays from Clinac 600C. Polystyrene values are unscaled. The values in polystyrene are always within $\pm$ 2% of the water values 31

LIST OF FIGURES, CONTINUED

Figure — Page

8. Percent depth dose in polystyrene [the continuous line] and in water [the symbols] for field sizes of 5 x 5, 10 x 10, and 20 x 20 cm up to 20 cm of depth, for 6 MV x-rays from Clinac 600C. Water values are from scaled depth. The values in polystyrene are always within $\pm$ 2% of the water values 32

9. Picture [A] shows one poly and cork slab and also the frame in which all the poly and cork slabs fit in. Picture [B] shows two poly slabs with windows cut-in and a cork slab fitted into the windows . . 35

10. Pictures [A] and [B] displaying the different stages of the phantom construction 36

11. Picture of the final phantom ready for the experiment 37

12A. A CT image of the midsagital plane of phantom is shown. At the top is 1.5 cm of polystyrene for build-up, below is the cork simulating lung region. Below the cork a polystyrene again is used for simulating soft tissue. In the middle a vertical polystyrene slab with TLDs placed along the central axis can be seen. The average CT numbers over different regions of interest is extracted and is given in Table 6 40

12B. A negative CT image of midsagital plane of the lung phantom is shown here. At the top 1.5 cm of polystyrene, in the middle cork simulating lung and at the bottom polystyrene simulating soft tissue is shown. In the middle a vertical poly slab with TLDs placed along the central axis is also seen. Average CT numbers of different regions of interest is extracted and is shown on Table 6 . . . 41

13. This is a simple layer geometry phantom. $T_{B.U.}$ is the thickness of the build-up region, which is kept at 1.5 cm. T_{LUNG} is the thickness of simulated lung cork region, the thickness of this region varied from 10 to 20 cm. The density of this cork region is 0.15 [relative electron density]. The placement of TLDs are shown along the central axis circles 45

LIST OF FIGURES, CONTINUED

Figure — Page

14. This is a tumor geometry phantom, $T_{B.U.}$ is the thickness of lung, which varied from 10 to 20 cm. T_{TUMOR} is the thickness of the tumor at the middle of simulated lung. The tumor is 2 x 2 x 0.625 cm thick. The placements of TLDs along the central axis is shown by circles 46

15. Pictures showing different materials used for TLD dosimetry. The seasoned aluminum planchet and the poly phantom and the vacuum machine are seen in [A]. In [B], the oven is shown 49

16. Picture [A] showing the clear polystyrene phantom for TLD irradiation during calibration. Picture [B] shows the setup for TLD irradiation for calibration 51

17. A histogram showing frequency of occurrence according to class of integrated TLD reading in ncoul of 228 TLD rods 52

18. A histogram showing frequency of occurrence of final selected TLDs of classes 4, 5, and 6. The mean value of response of these three classes is 16822.868 (ncoul) 54

19. Percent depth dose in polystyrene using TLD dosimeter [continuous line] and using ion chamber [square marks] for a field size 10 x 10 cm up to 20 cm depth, for 6 MV x-rays from the Clinac 600C. The values in polystyrene are always within $\pm$ 2.5% of the water values 56

20. Measured and calculated central axis percent depth dose for a 6 MV x-ray from a Clinac 600C for a 10 cm thick non-tumor lung phantom composed of cork with 1.5 cm overlay of build-up. The field size is 5 x 5 cm 59

21. Measured and calculated central axis percent depth dose for a 15 MV x-ray from a Clinac 20 for a 10 cm thick non-tumor lung phantom composed of cork with 1.5 cm overlay of build-up. The field size is 5 x 5 cm 60

LIST OF FIGURES, CONTINUED

Figure		Page
22.	Correction factors for 6 MV x-rays, 10 cm lung depth for [A] non-tumor geometry, and [B] tumor geometry. The depth (cm) is shown in the x-axis and CF is shown in the y-axis	61
23.	Correction factors for 6 MV x-rays, 20 cm lung depth for [A] non-tumor geometry, and [B] tumor geometry. The depth (cm) is shown in the x-axis and CF is shown in the y-axis	62
24.	Correction factors for 15 MV x-rays, 10 cm lung depth for [A] non-tumor geometry, and [B] tumor geometry. The depth (cm) is shown in the x-axis and CF is shown in the y-axis	67
25.	Correction factors for 15 MV x-rays, 20 cm lung depth for [A] non-tumor geometry, and [B] tumor geometry. The depth (cm) is shown in the x-axis and CF is shown in the y-axis	68

ABSTRACT

The purpose of this study was to measure photon dose distribution in the presence of low density lung tissue for several clinically relevant situations. A special lung phantom was constructed to facilitate the measurements of dose to the lung. The measurements were made for 6 MV and 15 MV x-ray beams in low electron density lung-equivalent material (0.15 relative to water) as well as in water-equivalent polystyrene. The doses were measured by using 1 x 1 x 6 mm LiF thermoluminescent dosimeters. The data are reported as % of the central axis depth doses and heterogeneity correction factors. The measured dose distributions were compared to calculations using the effective source surface distance (ESSD) and generalized Batho power law (BPL) inhomogeneity correction method algorithm incorporated in CAP-PLAN RT110 treatment planning computer system and with a modified power law (MPL) algorithm developed by Thomas (1991), for high energy x-rays.

The effective SSD algorithm overestimated depth doses in all situation inside and beyond the lung for both 6 MV and 15 MV x-rays. The generalized BPL overestimated depth doses in all situations for small 5 x 5 cm field sizes. In large 20 x 20 cm fields, BPL predicted depth doses quite accurately inside the lung for both geometries and behind the lung in the non-tumor geometry for both 6 MV and 15 MV x-rays. The accuracy of the BPL calculated values for the 20 x 20 cm fields was always within +/-3% of the measured values. The MPL method overestimated the

correction factors in all situations calculated, and for both 6 MV and 15 MV x-rays. The overpredictions of the MPL correction factors were always more than 5%, except in two cases, and the maximum error was 24%.

INTRODUCTION

1. Statement of Problem

Today amidst the increase incidence of all cancers, lung cancer in its worldwide occurrence ranked first in males and sixth in females (Parkin et al. 1988). In the United States, lung cancer was the leading cause of cancer death in both males and females in 1990 (Silverberg et al. 1990). In spite of this wide spread prevalence, surgery and chemotherapy have failed to accomplish a reasonable survival benefit. Radiation therapy remains (largely) an acceptable choice of treatment, both for cure and palliation in lung cancer patients.

Even though the recent technological advances have revolutionized the field of radiation therapy, management of lung cancer still remains a difficult one. Among other reasons, the presence of inhomogeneity due to low density lung tissue and unit density (1 g/cc) tumor inside the lung causes a complex and significant problem in radiation therapy dosimetry. The alteration in primary and secondary radiation makes the accurate calculation of the dose distribution very complex (Johns and Cunningham 1983). The increased transmission of radiation inside and beyond the lung due to low density lung tissues causes higher dose in surrounding organs. The problem of inhomogeneity is more compounded at the interfaces of low density lung and unit density tissue or tumors. Immediately beyond this interface, the predictable electronic equilibrium is lost. The size of this region of electronic disequilibrium varies with different energy photons, increasing with higher energies. Thus, another

build-up region is observed at the lung tissue-soft tissue/tumor junction. This rebuild-up causes dose variations resulting in lower doses at the interfaces or at the tumor surfaces (Laughlin et al. 1980). Unawareness of these two effects and not correcting for these phenomena may lead to significant dose calculation errors. The increased range of secondary electrons inside the lung tissue is an associated problem which causes the loss of beam flatness and results in increase of the penumbra (Ekstrand et al. 1990). Because dose distribution varies in and around lung tissue, a correction for prescribed doses is necessary.

Ever since Batho (1964) proposed a correction method for low density lung inhomogeneity, alternate opinions been expressed and numerous papers published on the subject. Orton et al. (1984) relate several reasons for implementing lung dose corrections. They are: (1) gradual introduction of inhomogeneity-corrected data to replace the empirical clinical experience will help gain and accumulate more accurate data, (2) approximated dose corrections are better than no correction, (3) fairly accurate hand calculation methods and treatment planning computers incorporating inhomogeneity correction algorithms are available, (4) computed tomography (which is essential for inhomogeneity correction methods) is widely available and in general use, and finally (5) continued cataloging of clinically imprecise data is unreasonable. Even though the matter of lung dose correction in photon beam treatment planning has not been resolved among clinical medical physicists and oncologists, it seems important to perfect a scheme to correct for lung inhomogeneity.

It has been reported that a 5% increase in dose causes a 20% increase in

radiation induced lung pneumonitis (Van Dyk et al. 1981). Increased incidences of transverse myelitis from thoracic irradiation has been documented (Philips et al. 1969). These complications of increased radiaton can be avoided by precise individualized dosage calculation with lung inhomogeneity corrections. Additionally, after making correction for low density lung inhomogeneity, improved isodose distributions for tangential-field breast irradiation for reducing hot spots have been observed (Kuchnir et al. 1989). Figure 1 shows dose distributions for a supraclavicular field calculated on a Capintec CAP-PLAN RT110 treatment planning computer (MBPCC) for anterior and posterior SAD irradiation. A prescribed dose of 112 cGy and 65 cGy isocenter given dose (GD_{iso}) is used for anterior and posterior fields, respectively, in which a considerable amount of lung is also irradiated by using 4 MV photons from a linear accelerator Clinac 4. None of the plans has been normalized, so that actual dose distribution without inhomogeneity and after inhomogeneity correction can be observed. With the inhomogeneity correction by effective SSD method it is seen that the dose inside the lung increases by more than 10%. It is imperative that dose corrections for low density inhomogeneous lung tissue should be evaluated and practiced.

The main constraints in calculating a meaningful correction factor for lung inhomogeneity are due largely to the unavailability of an accurate anatomical description of the lung and the tumor inside the lung and also the uncertainty of the relative electron density of lung tissue to that of water. The relative electron density of lung tissue on which the attenuation of the primary and also the secondary scatter

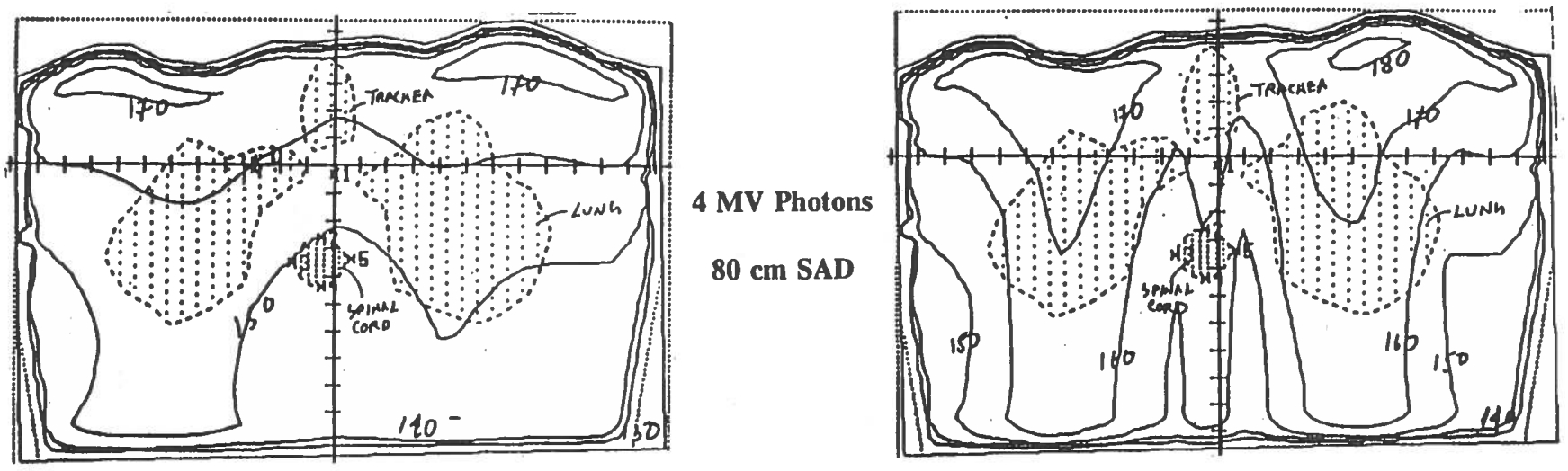

FIGURE 1. The dose distribution of the supraclavicular field using 4 MV photons. Picture [A] without heterogeneity correction compared to, [B] that after corrected by effective SSD method for heterogeneity.

component of radiation depends, ultimately effects the correction factor for that particular photon energy and that particular patient (Sontag et al. 1977; Geise et al. 1977). Also, the electron density of lung relative to water varies in a wide range from patient to patient, depending on many different factors (Van Dyk et al. 1982). Therefore, an assumed value of lung density may lead to consistently significant errors while treating lung cancer patients. With the advent of computed tomography (CT), it is now possible to acquire detailed anatomical information of individual patients and a more precise estimate of the electron density in inhomogeneous tissue for each patient (Sontag et al. 1977). Though the level of sophistication and accuracy of lung dose correction methods vary considerably, to date there are many methods for lung inhomogeneity corrections available. Eight of the common clinically applicable methods of inhomogeneity correction are described as follows.

Linear Attenuation Coefficient Method (Sontag and Cunningham 1977)

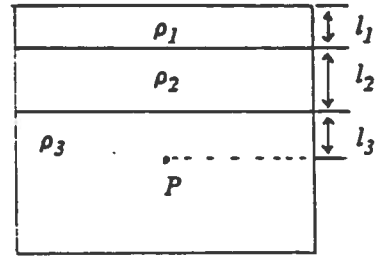

The correction factor (CF) is

$$CF = e^{\mu'(d-d_{eff})},$$

where $d_{eff} = l_1 * \rho_1 + l_2 * \rho_2 + l_3 * \rho_3 + \ldots$. l_1 is the thickness of the region with mass density ρ_1, l_2 is the thickness of the next underlying region with mass density

ρ_2. μ' is emperically determined effective attenuation coefficient. The effective depth (d_{eff}) determined is used to modify the tissue attenuation through the inhomogeneity for calculating the correction factor *(CF)* at the point of interest *P*.

Effective SSD Method (Thacer and Palti 1981)

The correction factor (CF) is

$$CF = \frac{\%dd[W,d']}{\%dd[W,d]} * \left[\frac{SSD+d'}{SSD+d}\right]^2 .$$

This method uses water equivalent effective depth and is also referred to as effective path length (EPL) method by the Capintec CAP-PLAN RT100 treatment planning computer system. *CF* is the ratio of the dose in water at the effective depth to the dose in water at the actual physical depth multiplied by an inverse square factor; $d' = \Sigma d_i * \rho_i$, and d_i is the thickness of tissue with mass density ρ.

Isodose Shift Method (Cunningham 1982)

The correction factor (CF) is

$$CF = \frac{\%dd[d'', W, SSD]}{\%dd[d, W, SSD]} .$$

This method corrects standard isodose charts for the presence of inhomogeneity. This is an extension of the empirical isodose curve displacement method for correction of oblique beams. $d'' = d\text{-}n(d\text{-}d')$, where d is the physical depth, d' is the effective depth, and n is a fraction, the value which is dependent on beam energy.

Ratio of TAR (Tang et al. 1986)

The correction factor (CF) is

$$CF = \frac{TAR(d', r_d)}{TAR(d, r_d)} ,$$

where d is the physical depth below the body surface, d' is the effective depth to the point of calculation. Effective depth is the physical depth scaled by the relative electron density of the medium along the primary photon path, r_d is the field size at depth d.

Original Batho Method (Sontag and Cunningham 1977)

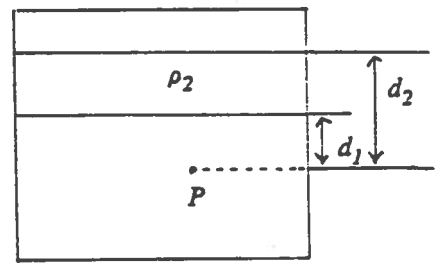

The correction factor (CF) is

$$CF = \left\{ \frac{TAR(d_1, A)}{TAR(d_2, A)} \right\}^{1-\rho_2} ,$$

where the relative electron density of the material where point P is located in unity (1 g/cc), d_1 is the distance from the point of calculation to the front of the material, A is the field size at the point of calculation, and d_2 is the distance from the point to the front of the overlying material.

Generalized Batho Method (Sontag and Cunningham 1977)

The correction factor (CF) is

$$CF = \frac{TAR(d_1, A)^{\rho_1 - \rho_2}}{TAR(d_2, A)^{1-\rho_2}},$$

where ρ_1 is the relative electron density of the material where point P is located, d_1 is the distance from the point to the front of the material, ρ_2 is the relative electron density of the overlying material, d_2 is the distance from the point to the front of the overlying material, and A is the field size at the point of calculation.

Equivalent TAR (Songtag and Cunningham 1978)

The correction factor (CF) is

$$CF = \frac{TAR(d', \bar{r})}{TAR(d, r)}, \quad d' = \frac{d * \sum_{i=1}^{n} \rho_i}{n}, \quad \bar{\rho} = \frac{\sum_i \sum_j \sum_k \rho_{ijk} * W_{ijk}}{\sum_i \sum_j \sum_k W_{ijk}},$$

where d' is the effective depth (physical depth scaled by relative electron density of the medium to the water), d is the physical depth, r is the beam dimension at depth d, $\bar{r} = r * \bar{\rho}$ scaled beam dimension to account for scatter radiation, and $\bar{\rho}$ is the weighed density of the irradiated tissue volume.

Modified Batho Power Law Method (Thomas 1991):

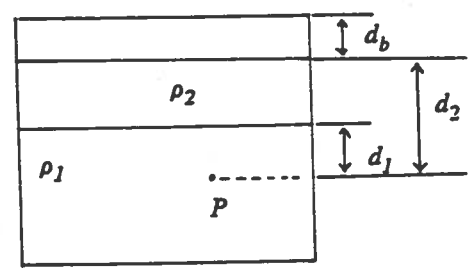

The correction factor (CF) is

$$CF = \frac{TMR\left[d_1 + d_b, A\right]^{\rho_1 - \rho_2}}{TMR\left[d_2 + d_b, A\right]^{1-\rho_2}} ,$$

where ρ_1 is the relative electron density of the material were point P is located, d_1 is the distance from the point to the front of the material, ρ_2 is the relative electron density of the overlying material, d_2 is the distance from the point to the front of the overlying material, d_b is the build-up depth, and A is the field size at the point of calculation.

The aid of computers for performing individual patient treatment plans was one of the most important events in the radiation therapy field to come into general use, after the availibility and application of megavoltage beam for treatments. Based mostly on wide acceptance and popularity, several of the above-mentioned correction methods for lung inhomogeneity have already been incorporated in many different computer treatment planning systems (Orton et al. 1984). Mary Bird Perkins Cancer Center (MBPCC) in Baton Rouge, Louisiana, uses the computer treatment planning system developed by Capintec Company (Ramsey, New Jersey) called the CAP-PLAN RT110. This treatment planning system uses effective SSD and the generalized Batho power law (BPL) correction methods to calculate doses in and around low density inhomogeneous lung tissue (Operator's Manual, Cap-Plan, MBPCC, 1991).

The effective SSD method corrects for the attenuation of the primary beam of radiation. It does not take into account the changes in the scatter component of

the radiation, the shape and the size of the inhomogeneity, the electronic disequilibrium at the lung-soft tissue or tumor interface, and the density of the material below the inhomogeneity (Johns and Cunningham 1983). As such, effective SSD method has been found to overestimate the dose in and beyond the lung.

The Batho power law method accounts for changes in primary component of radiation and indirectly takes into account the scatter component of the radiation beam and the position of the point of calculation relative to the inhomogeneity. It does not take into account the lateral dimensions and the shape of the inhomogeneity, the existence of the electronic disequilibrium at the interface, and it does not recognize the material below the point of interest (Sontag and Cunningham 1978). The original Batho Power Law can only calculate correction factors when the point of calculation is below (or beyond) the inhomogeneity and lies within the unit density (1 g/cc) tissue (Sontag et al. 1977). In the generalized form of the Batho Power Law (BPL), correction factors can be calculated for points both within the inhomogeneity and also below (or beyond) the inhomogeneity (Sontag et al. 1977). The BPL method has been found to agree well with measured doses within and below the lung for simple geometries (Wong and Henkelman 1982; Van de Geijin 1987; El-Khatib and Battista 1986). It has been reported, however, that as the energy of the photons is increased and the field sizes are decreased, accuracy decreases (Wong et al. 1982; Sontag et al. 1977).

The modified power law (MPL) heterogeneity correction method is a simple alternative of applying the generalized Batho power law in regions where longitudinal

electronic equilibrium has not been established. It has been reported that this method is in agreement with the measured data to within 2% for a range of field sizes from 5 x 5 cm to 16 x 16 cm for Cobalt-60 gamma-rays, 8 MV x-rays, and 16 MV x-rays (Thomas 1991).

Extensive studies have been done to test the validity of the effective SSD and BPL method for Cobalt-60; for both lower and higher energy photons, the ion chamber was the choice of dosimeter to do so. Accordingly, dose distribution at the interface of the two inhomogenous tissues is either absent or unreliable. Also, the investigation of a re-buildup region, if any, at the surface of the tumor inside the lung is impossible with ion chamber measurements. Dose distribution in low density with a proper dosimeter, due to different field sizes and different depths of lung must be investigated systematically, with and without the presence of simulated tumor.

2. Objectives and Approach

The objectives of the present study are three-fold. The first is to measure and understand the complex process of dose distribution in and beyond low density lung tissue. Special attention will be given to the interface of unit density soft tissue and the lower density lung tissue, where electronic disequilibria exist. The reason for this is the frequent presence of tumors in this disequilibrium region and the lack of proper dosimetry in these situations. Small thermoluminescent dosimeters will be used to overcome the disadvantage of the ion chambers.

The second objective is to evaluate the lung dose correction algorithms

(effective SSD and generalized BPL methods) incorporated in the Capintec developed CAP-PLAN RT110 treatment planning system. Neither of these correction methods takes into account of the electronic disequilibrium at the interface, and using instead an average density of lung. To design an accurate plan for lung cancer patients, it is essential to investigate the uncertainity associated with the algorithm's ability to handle the lung inhomogeneity correction for points within the build-up region and beyond.

The third objective is to determine what other algorithm may better fit the experimental data. To fulfill the third objective, a recently developed modified Batho power law algorithm (MPL) was chosen for verification.

A phantom was constructed using polystyrene as the tissue-equivalent material and cork as the low density material simulating the lung. Dose distributions were measured in the central axis of the phantom after photon irradiation. The dose was delivered using the 6 MV photon beam from a Varian Clinac 600C and 15 MV photon beam from Varian Clinac 20. TLD-100 Harshaw rods were used as dosimeters. Correction factors due to low density lung were determined from the dose distribution measured in the central axis of the phantom. The measured dose distribution was then compared with the calculations using effective SSD and generalized BPL methods algorithms using CAP-PLAN RT110 treatment planning system, and with a MPL algorithm developed recently (Thomas 1991) for high energy x-rays using hand calculations.

MATERIALS AND METHODS

1. Phantom Construction

A) Selection of Materials

Lung tissue has a lower electron density (relative to water) than normal soft tissue of the body. It is also often reported that the lung electron density varies over a range from 0.15 to 0.35 relative to water (Kean and Van Dyk 1985). To simulate lung tissue for dosimetric purposes, many different materials have been used. Lung equivalent plastic developed by Radiation Measurement Incorporated (RMI), cedar wood, balsa wood, cork, and in-house made materials are some of examples. Cork is the most widely used material for simulating lung tissue. Because there are many grades and types of cork available in the market, it is very important to select and use an appropriate cork having relevant electron density relative to water found in patients.

There are many different ways of determining the relative electron density of a material. Besides doing calculations based on elemental compositions, measuring the attenuation of a narrow beam of gamma rays from a monoenergetic radioactive source through an absorber is probably one of the most accurate ways. In the energy range from 100 keV to 10 MeV, the interaction of x-rays with matter is through Compton collisions (with a very negligible amount of photoelectric effect). The probability of Compton interaction is approximately independent of atomic number (Z) and depends mainly on the electron density of the material (Attix 1986; Perez and

Brady 1987). The measured ratio of a well collimated beam through the same thickness of cork and water under the condition of good geometry will thus reflect the relative electron density of cork. We know that a fraction of a photon beam attenuated per unit thickness of absorber which is defined as linear attenuation coefficient, is given by:

$$\lim_{\Delta t \to 0} \frac{\frac{\Delta I}{I}}{\Delta t} = -\mu(\rho, z) ; \qquad (1)$$

solving the equation we find:

$$I = I_0 * e^{-\mu(\rho,z) * t} , \qquad (2)$$

where ΔI is the fractional change in the intensity of beam due to the fractional change in thickness of absorber Δt, and μ is the linear attenuation coefficient which is a function of the density and the effective atomic number of the material. It is clear from Eq.(2) that the transmitted intensity on the other side of the absorber can be changed by either an alteration in the atomic composition, the density, or the thickness of the absorber. The effective atomic number of cork and water differs by less than 10%. Because the ratio of the mass energy absorption coefficients and mass stopping power varies slowly with the atomic number, the atomic composition of the cork and water may be considered the same for the purpose of this study (Thacher and Palti 1981). If thickness remains the same and the atomic composition is also the same, then the emerging intensity of the I/I_0 transmittance will only depend on the electron density (electron/cc) of the material. Under good geometry, taking the ratio of transmittance through cork and water will give us the relative electron density of

the material relative to water. The following equation expresses the above-mentioned idea:

$$\rho_{e,cork} = \frac{\frac{I}{I_{0,cork}}}{\frac{I}{I_{0,water}}} = \frac{e^{-\mu(\rho,z)_{cork} * t}}{e^{-\mu(\rho,z)_{water} * t}} . \quad (3)$$

Note that the thickness of the cork and water is kept the same in accordance with Eq.(2).

Shortly after the advent of the computed tomography (CT) and its use in radiation therapy, it was realized that the CT numbers can also be successfully converted to relative electron density of a scanning material (Geise and McCullough 1977; Prasad et al. 1979). Today many investigators have related CT numbers with the relative electron densities obtained directly by using a Compton scanner, proving the validity of this technique (Van Dyk et al. 1982; Battista et al. 1980). CT numbers are essentially attenuation coefficients for x-rays of diagnostic energies. CT scanners use a fixed CT number equal to zero for water and -1000 for air so that in the Hounsfield unit (HU) it is quantified by the following equation:

$$CT\ number\ (HU) = \left[\frac{\mu_m - \mu_w}{\mu_w}\right] * 1000 , \quad (4)$$

where μ_m is the linear attenuation coefficient for a material scanned and μ_w is the linear attenuation coefficient of water. The number 1000 is the scaling factor. According to Battista et al. (1980) the CT numbers can be converted to electron density, relative to water, by using the following equation:

$$\rho_{e,soft} = 1.000 + 0.001\ N_{CT}, \qquad -1000 < N_{CT} < 100\ ; \tag{5}$$

$$\rho_{e,bone} = 1.052 + 0.00048\ N_{CT}, \qquad N_{CT} \geq 100\ ; \tag{6}$$

where $\rho_{e,soft}$ and $\rho_{e,bone}$ are the electron densities of soft tissue and bone tissue, relative to water, and N_{CT} is the CT numbers, in Hounsfield units. The overall estimated uncertainty of this method in the CT-derived electron density is about +/- 3%.

Alternatively, a calibration curve can also be generated from data obtained by scanning a phantom containing plugs of different materials of known relative electron density. However, extreme caution must be taken while generating a calibration curve using both low and high Z materials, since the slope of the curve will differ depending on the Z of the material. For the use of radiation therapy treatment planning, linear interpolation between data points of the straight portion of the curve can be used to convert CT numbers directly to relative electron density of any other materials or tissues having a Z number close to water. This technique is used to select a cork of proper density and all other materials needed for the construction of a phantom for this work.

A CT phantom containing several plug materials of known relative electron density and water was used to generate a calibration curve of CT numbers versus relative electron density. The phantom along with the plugs are shown in Figure 2. Plug materials were supplied by Radiation Measurements Inc. (RMI), Middelton, Wisconsin. A set of reference CT numbers and relative electron density of the plugs

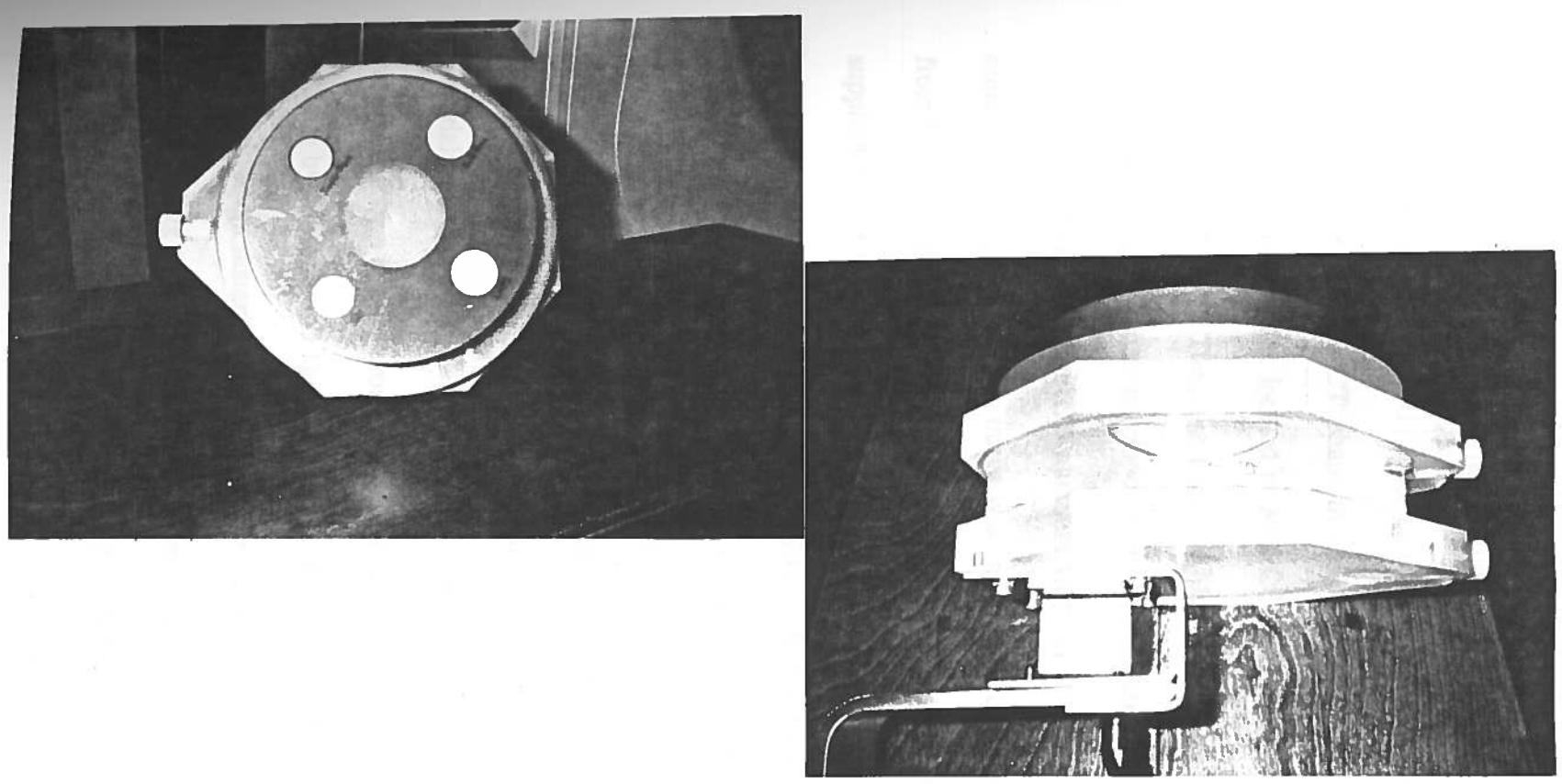

FIGURE 2. Picture showing the CT phantom containing the plugs of different materials of known relative electron density, used to generate the calibration curve of CT numbers versus relative electron density. The little white circles are the plugs of simulated lung, hard bone, soft bone and fat. The brown [black in this picture] ring is solid water and the inner white circle is made of acrylic.

were also supplied by RMI. The relative electron densities were calculated and determined (Constantinou 1991) based on the elemental compositions of plugs and are shown in Table 1. The CT phantom and the plugs were scanned by several CT scanners: a Somatom CR located at MBPCC, and a GE 9000 and Somatom DRH located at Our Lady of The Lake Regional Medical Center, Baton Rouge, Louisiana. The CT numbers and their corresponding densities are shown in Table 2.

It is found that the CT numbers from different scanners corroborate each other. As such, a calibration curve was then drawn based on CT numbers obtained from in-house (MBPCC) Somatom CR CT scanner and the relative electron densities supplied by the manufacturer. This curve is shown in Figure 3; it is similar to the one published by Ten Haken et al. (1991). It can be seen from the curve that materials having the average Z numbers close to water fall in a straight line. Many different types of cork, woods, and other materials showing promise for simulating lung tissue in the phantom were then scanned, and the average CT numbers obtained were converted to relative electron densities using the calibration curve. Some of the materials scanned are shown in Figure 4. None were found to have the desired mean relative electron density around of 0.25 as reported to be the relative electron density of lung by Mustafa and Daphr (1983). The data in Table 3 shows the CT numbers of the different materials scanned and their corresponding relative electron densities.

Failing to find a cork having a density around 0.25, mean CT numbers of 30 different lung carcinoma patients were gathered. CT numbers were read over the whole lung, averaging an irregular field, always avoiding the grossly diseased lung.

TABLE 1

Breakdown of elemental composition. Percentage by weight of the RMI plug materials used in the CT phantom to generate the calibration curve of CT number versus relative electron density (relative of water).

Tissue Substitute (Plastic)	Hydrogen [H] Atomic #1	Carbon [C] Atomic #6	Nitrogen [N] Atomic #7	Oxygen [O] Atomic #8	Chlorine [Cl] Atomic #17	Calcium [Ca] Atomic #20	Fluorine [F] Atomic #9	Magnesium [Mg] Atomic #12	Silicon [Si] Atomic #14	Specific Gravity [g/cc]
SB3 (Cortical Bone)	3.10	31.26	0.99	37.57	0.095	27.03	—	—	—	1.84
IB (Inner Bone)	7.90	63.79	4.23	9.88	14.20	—	—	—	—	1.16
AP6 (Adipose Tissue)	8.36	69.14	2.36	16.93	0.14	—	3.07	—	—	0.92
LN300 (Lung)	8.26	60.41	1.67	17.33	0.15	—	—	11.36	0.72	0.30

TABLE 2

CT numbers [HU] shown read from different CT scanners and corresponding electron density, relative to water and physical density of various materials used in CT phantom for generating calibration curve of CT numbers versus relative electron density.

MATERIALS AND TISSUE SUBSTITUTE	SIEMENS DR3 [RMI] CT # in HU	SOMATOM DRH [OLOL] CT # in HU	GE9000 [OLOL] CT # in HU	SOMATOM CR [MBPCC] CT # in HU	RELATIVE ELECTRON DENSITY RELATIVE TO WATER [RMI]	PHYSICAL DENSITY [g/cc]
Lung Tissue	-700 [± 40]	-664	-636	-679	0.292	0.3
Adipose Tissue	-105 [± 20]	-118	-105	-121	0.892	0.92
Inner Bone	240 [± 10]	254	279	248	1.081	1.12
Cortical Bone	1350 [± 20]	1435	1521	1429	1.707	1.84
Acrylic	—	92	99	92	1.147	1.18
Solid Water	—	2	8	1	1	1.0

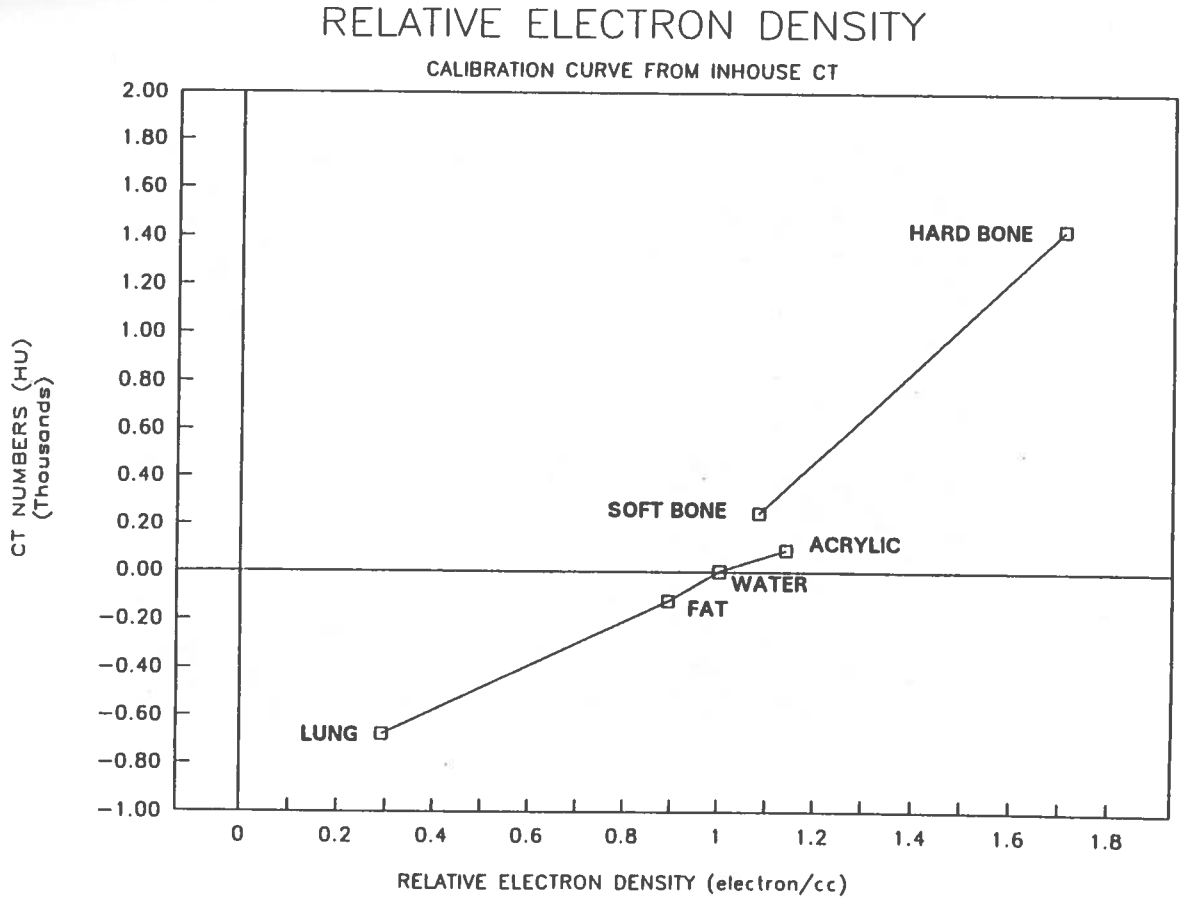

FIGURE 3. Calibration curve, based on CT plugs of known relative electron density. The CT number are read by somatom CR, inhouse CT (MBPCC), mA = 550, KVp = 125. The X-axis shows the relative electron density [ρ_e, medium/ρ_e water] and the Y-axis shows the CT numbers in hounsfield units.

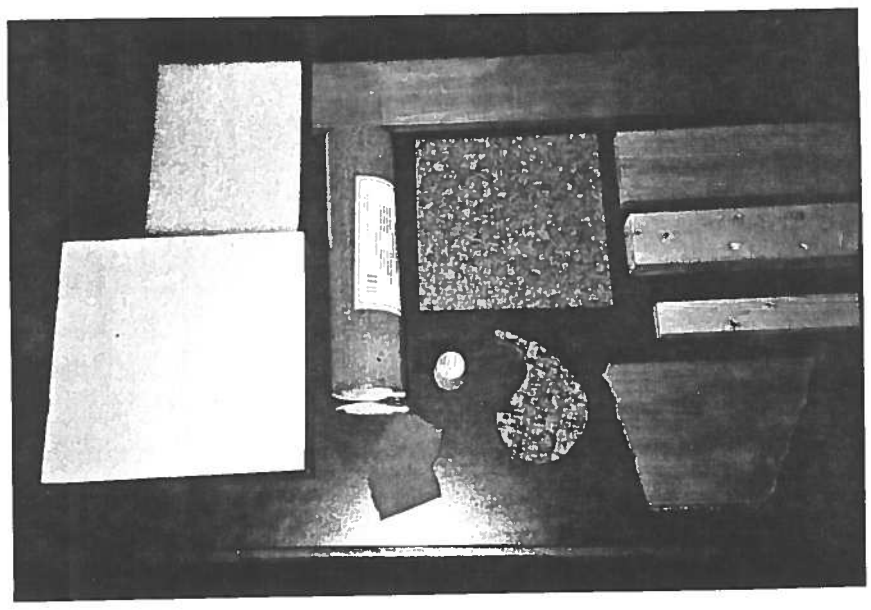

FIGURE 4. Picture showing some of the materials scanned by inhouse (MBPCC) somatom CR CT scanner, to determine the relative electron density, for simulating lung tissue in the phantom. The materials shown here are different types and grades of cork and some different kinds of woods.

TABLE 3

CT numbers [HU] and corresponding relative electron density read from calibration curve, of different materials scanned by inhouse somatom CR CT scanner.

MATERIALS SCANNED BY INHOUSE SOMATOM CR CT SCANNER [MBPCC]	MEAN CT NUMBERS [HU]	ELECTRON DENSITY RELATIVE TO WATER
Cork Stopper	-815	0.14
Cork Inhouse Chest Phantom	-775	0.185
Hard Cork	-770	0.185
Cork Sheet [0.625 cm thick] *(Michael's Arts & Crafts)*	-794	0.15
Cork Bulletin Board	-776	0.19
Soft Cork Tiles *(Home Depot)*	-872	0.08
Hard Board, Type I	-362	0.62
Hard Board, Type II	-396	0.60
Styrofoam	-977	0.001
Soft Poly Bubble	-927	0.02
Cedar Wood	-637	0.33
Red Wood	-552	0.43
SPF Wood [spruce, pine, fur]	-674	0.29
Floor Cork Tiles [clay building]	-635	0.33
White Polystyrene	-11	0.999

The mean CT number and the corresponding electron density, relative to water, are shown in Table 4. The mean CT numbers were all divided into classes having an interval of 50. A frequency and distribution analysis on these patient data were done, and it was found that the maximum distribution occurs in classes 6 and 7. The CT numbers falling in these two classes ranges from -752 (HU) to -841 (HU), and have a mean CT number of -798 (HU). The corresponding electron density read from the calibration curve is 0.15. A histogram based on frequency of CT numbers according to class is shown in Figure 5. This mean CT number obtained from patients' lungs and the corresponding density seems a little lower than expected. But Robinson and Kreel (1979), have reported CT numbers ranging from -622 to -894 (HU) of lung tissues after scanning 17 patients of different ages. Also, Rosenblum et al. (1978) observed and reported a mean CT numbers of -742 (HU) after scanning 29 patients; all these corroborated the data of this study. To exclude any probable artifacts arising from the CT couch, the CT phantom and plugs and all other materials were scanned on the top of the CT table. No significant difference was found in CT numbers. A 0.625 cm (1/4") thick cork sheet, 30 x 60 cm, locally available at Michaels Arts and Crafts store, Baton Rouge, Louisiana, was found to have the average CT number of -800 (HU) and therefore was used for constructing the lung phantom.

High-impact white polystyrene was the other material used to simulate soft tissue, for constructing the phantom. According to the manufacturer's claim (Westlake Plastics, Lenni, Philadelphia), its atomic and electron composition and

TABLE 4

Patients' mean CT number (HU) and corresponding relative electron density read from the calibration curve.

SERIAL NUMBER OF PATIENTS	SOMATOM CR CT NUMBER [HU] (MBPCC)	RELATIVE ELECTRON DENSITY
10	-543	0.44
14	-608	0.37
13	-688	0.28
2	-701	0.26
16	-705	0.26
19	-730	0.23
25	-736	0.21
30	-752	0.20
1	-754	0.20
28	-758	0.20
23	-758	0.19
22	-760	0.19
18	-787	0.16
27	-788	0.16
17	-789	0.17
4	-791	0.15
20	-798	0.15
8	-798	0.15
5	-803	0.14
6	-818	0.14
12	-826	0.14
11	-827	0.14
3	-835	0.11
29	-836	0.11
15	-838	0.11
26	-841	0.11
21	-849	0.10
24	-856	0.10
7	-858	0.10
9	-861	0.10

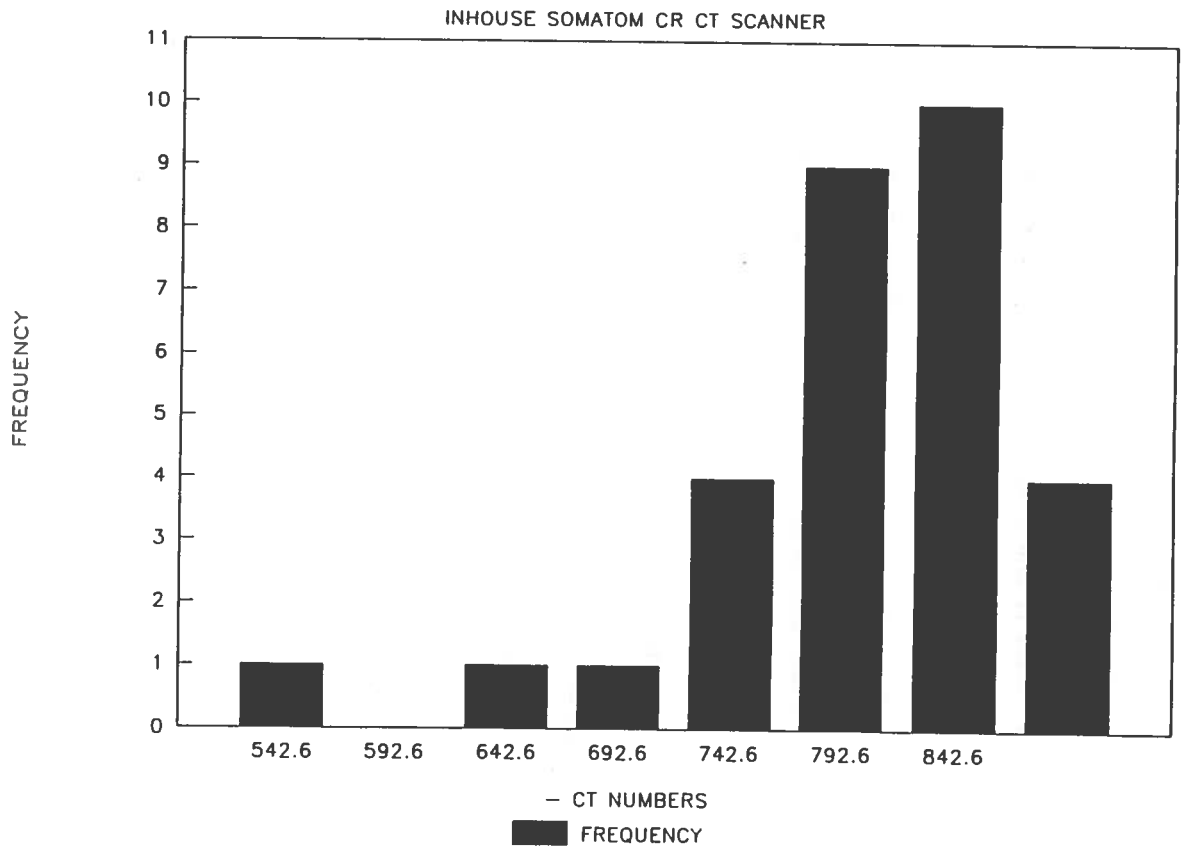

FIGURE 5. **Frequency of patients' mean CT number according to class. Maximum frequency occuring in classes 6 and 7, ranging from -752 (HU) to -841 (HU), and have a mean CT number of -798 (HU).**

density are similar to the water found in human tissue, which makes it an ideal medium for radiology dosimetry applications. The physical density supplied by the manufacturer of this white high-impact polystyrene is 1.04 (g/cc). The American Association of Physicists in Medicine Task Group 21 (TG21), documents the relative electron density of polystyrene to be 1.008, and is shown in Table 5. Nevertheless, to verify the manufacturer's claim, the white polystyrene was scanned by the Somatom CR CT (MBPCC) and it can be seen from Table 3 that the average CT number was -11 (HU). Even though polystyrene has a higher mass density and electron density than water, its average CT number is less than the CT number of water. If all interactions were through Compton scattering, then water should have a lower CT number than polystyrene. But water also has a higher effective atomic number than polystyrene (Table 5), which would cause some photoelectric interaction and would increase beam attenuation and subsequently give a higher CT number than polystyrene. This phenomenon has been observed by Phelps et al. (1975) and documented in detail. He indicated that the value of attenuation coefficients in CT using approximately 120 KVp does not depend on a single parameter of tissue, such as electron density or the average Z number, but in reality depends on the composite effects of electron density and the average atomic number of tissue or materials being scanned. Though one needs to be aware of this composite effects on CT number, the difference of attenuation is due to both density and average Z number rather than only density is probably within clinically acceptable criteria.

To confirm that polystyrene is equivalent to water, the dosimetric parameter

TABLE 5

Physical and dosimetric properties of water, acrylic, polystyrene, and muscle.[a]

	WATER H_2O	ACRYLIC $C_3H_RO_2$	POLYSTYRENE C_RH_R	ICRU MUSCLE
Density [g/cm^3]	1.00	1.17[b]	1.04[b]	1.00
Average atomic number $\bar{Z}$[c]	7.22	6.24	5.62	7.10
$\bar{Z}$ relative to water	1.000	0.86	0.78	0.98
Electron density [e^-/g^3]	3.346×10^{23}	3.253×10^{23}	3.243×10^{23}	3.32×10^{23}
Electron concentration [e^-/cm^3]	3.346×10^{23}	3.806×10^{23}	3.373×10^{23}	3.32×10^{23}
Electron concentration relative to water	1.000	1.37[a]	1.008	0.992

[a]Ref. American Association of Physicists in Medicine, Task Group 21, 1983

[b]Nominal values; the mass density of each dosimetry phantom should be individually determined

[c]The average atomic number $\bar{Z}$ is calculated by weighting the component atomic numbers by parts by weight

of the polystyrene was also investigated. Percent depth dose (%dd) and percent tissue maximum ratio (TMR) for 6 MV x-ray (Clinac 600C) were measured using an acrylic ion chamber for field sizes ranging from 5 x 5 cm to 20 x 20 cm in water phantom and in polystyrene phantom, up to 20 cm depth. Percent depth doses and percent TMRs are shown in Figures 6 through 8 as a function of depth. From these graphs it can be seen that there is essentially no difference in the central axis depth dose distribution between water and polystyrene phantom. The polystyrene phantom values are within experimental uncertainty of 2% of water phantom values.

The validity of conversion from percent ionization to %dd was also investigated. From AAPM Task Group 21 (1983), it is known that for example, that for a 10 x 10 cm field size and at depth 10 cm, the %dd for photon is shown in the following relationship:

$$\%dd = \frac{\dot{D}\left[10\times10\,(FS),\ 10(d)\right]}{\dot{D}\left[10\times10\,(FS),\ d_{\max}\right]}$$

$$= \frac{\left\{\bar{M} * TPC * ECF * N_{gas} * P_{ion} * P_{wall} * P_{repl} * \left[\frac{\bar{L}}{\rho}\right]_{air}^{medium}\right\}_{10\times10(FS),\,10(d)}}{\left\{\bar{M} * TPC * ECF * N_{gas} * P_{ion} * P_{wall} * P_{repl} * \left[\frac{\bar{L}}{\rho}\right]_{air}^{medium}\right\}_{10\times10(FS),\,d_{\max}}} \qquad (7)$$

where $\bar{M}$ is the average reading from the ion chamber, TPC is the temperature and pressure correction factor, N_{gas} is the cavity gas calibration factor in Gy/c determined at a standardizing laboratory or calculated from exposure factor N_x, P_{ion} is the ionization correction factor, P_{wall} is the wall correction factor, P_{repl} is the

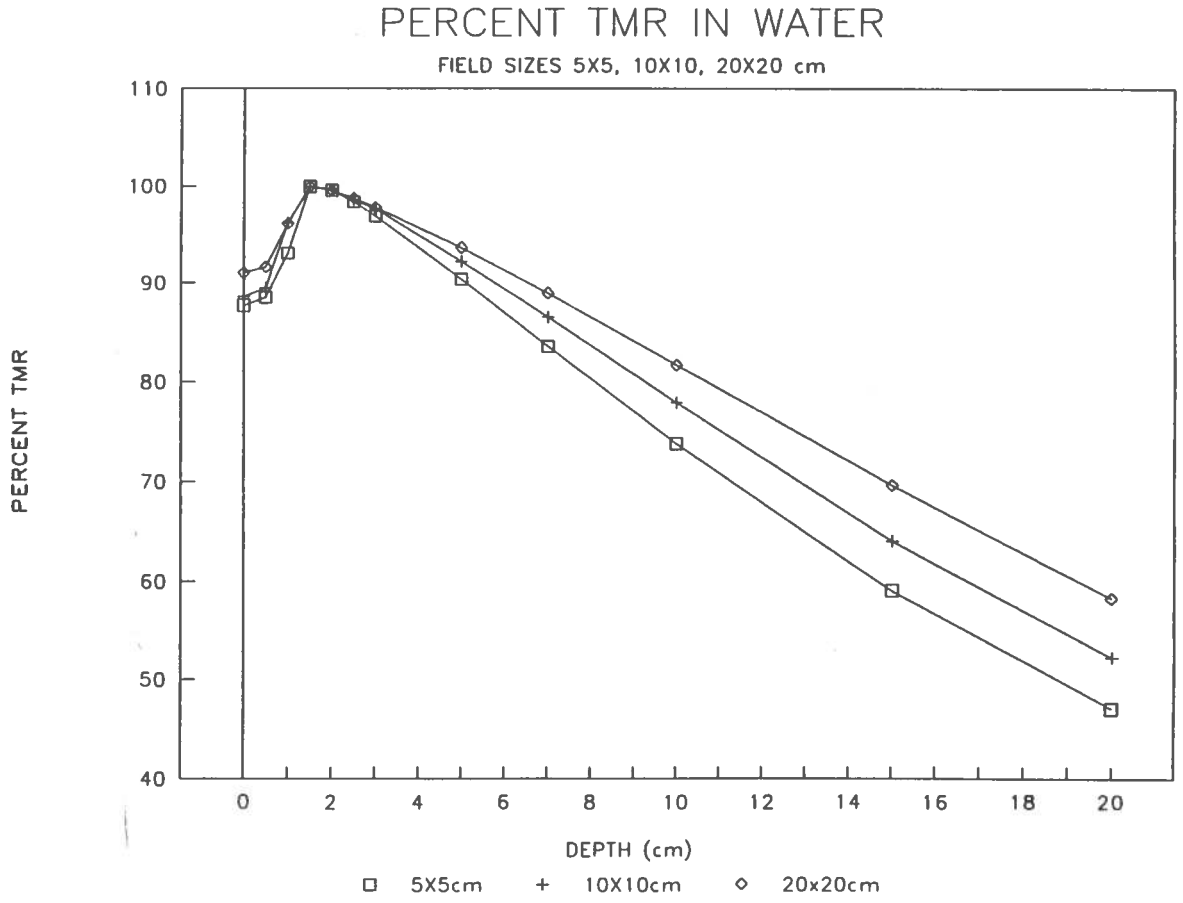

FIGURE 6. **Percent TMR in water for field sizes 5 x 5, 10 x 10, and 20 x 20 cm^2 up to 20 cm of depth, for 6 MV x-rays from Clinac 600C.**

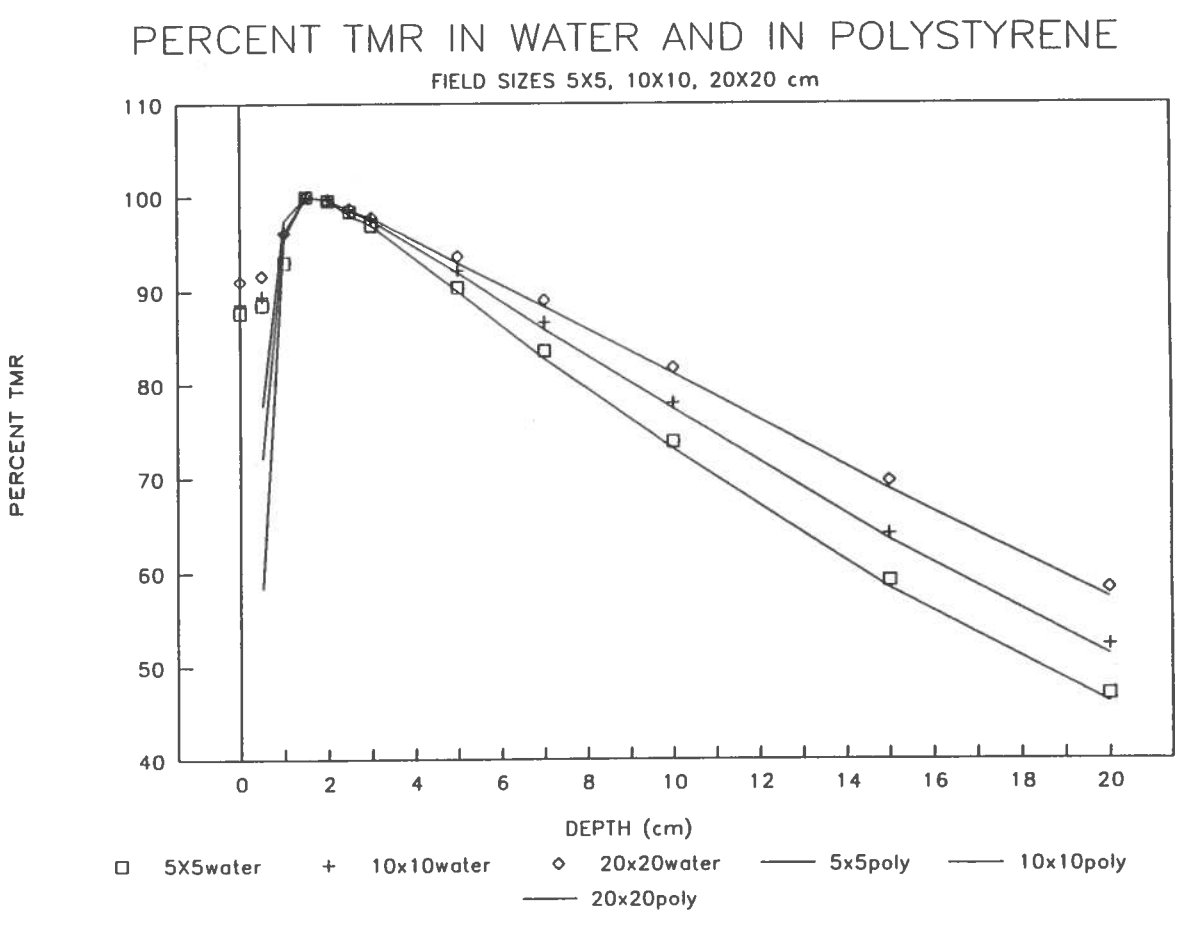

FIGURE 7. **Percent TMR in polystyrene [the continuous line] and in water [the symbols] for field sizes of 5 x 5, 10 x 10, and 20 x 20 cm^2 up to 20 cm of depth, for 6 MV x-rays from Clinac 600C. Polystyrene values are unscaled. The values in polystyrene are always within $\pm$ 2% of the water values.**

FIGURE 8. **Percent depth dose in polystyrene [the continuous line] and in water [the symbols] for field sizes of 5 x 5, 10 x 10, and 20 x 20 cm^2 up to 20 cm of depth, for 6 MV x-rays from Clinac 600C. Water values are from scaled depth. The values in polystyrene are always within $\pm$ 2% of the water values.**

replacement correction factor, and $\left[\frac{\bar{L}}{\rho}\right]_{air}^{medium}$ is the mean restricted stopping power ratio of the phantom medium to air.

From the above equation it can be seen that if the electrometer, ion chamber, and the phantom remain the same, then all the factors cancel each other, except the ionization readings $\bar{M}$ and the P_{ion}, which is the ionization recombination factor. If all the charges produced by radiation in the chamber are not collected, the dose calculated at any point will be smaller than the actual dose. Accordingly, a correction factor, which will account for ions that recombine is necessary for proper dose computation. Therefore, the only factor that should be considered while converting the ionization reading directly to dose, is the respective P_{ion}, which in turn is a function of the dose rate at depth.

P_{ion} at depth 1.5 cm and 20 cm in a polystyrene phantom was then determined following the steps of AAPM TG 21, which is based on Boag's two-voltage technique (Horton 1987). The collection efficiency is determined by making ionization measurements at two-voltage, V1 and 1/2V1. The ratio of the charge collected at V1 is referred to as Q1, and the charged collected at 1/2V1 reffered to as Q2 is plotted versus the quantity P_{ion} in AAPM TG 21. It was found that for 6 MV x-ray, at 1.5 cm, P_{ion} is 1.008 and at 20 cm depth P_{ion} is 1.006. The ratio of P_{ions} at these two different depths is 1.0019. While converting percent ionizations to %dd at 20 cm, which is the maximum experimental depth, there should be a difference of 0.19%, which by all practical means is negligible for the purpose of this study.

B) PHANTOM FABRICATION

Figures 9, 10, and 11 picture a lung phantom and its different parts during and after its construction. Polystyrene slabs of 0.625 cm (1/4") and 0.313 cm (1/8") thick were cut into pieces of dimensions 25.1 x 12.2 cm. Cork sheets were also cut into pieces of the same dimensions. All cork sheets were 0.625 cm (1/4") thick. All polystyrene and cork slabs were then placed horizontally inside a 25 x 25 x 27 cm of clear acrylic frame. In one polystyrene slab, horizontal holes of 1.6 mm diameter were drilled in a vertical arrangement 0.5 cm apart along the central axis for the placement of TLD rods. Holes were drilled at different depths starting from the surface up to a maximum of 20 cm depth. In one geometry, the polystyrene slab with TLDs were placed vertically inbetween other horizontally arranged polystyrene slabs as shown in Figure 9. After final arrangement, the whole phantom will have one vertical slab with TLDs at the central axis, sandwiched between horizontally arranged polystyrene slabs on both sides. Extra care was taken not to leave any air gaps in between the slabs. This particular arrangement was used to measure the percent depth dose in the homogenous polystyrene phantom using LiF thermoluminescent dosimeters.

Two other poly slabs were then used to make windows, shown in Figure 9, [B]. All had 1.5 cm polystyrene at the top, representing chest wall for the build-up region. In a previous observation, after measuring CT scans of 17 patients it was found that on an average, the thickness of anterior chest wall is anywhere between 1.5 to 2.5 cm. On the basis of this finding, 1.5 cm thickness of polystyrene was

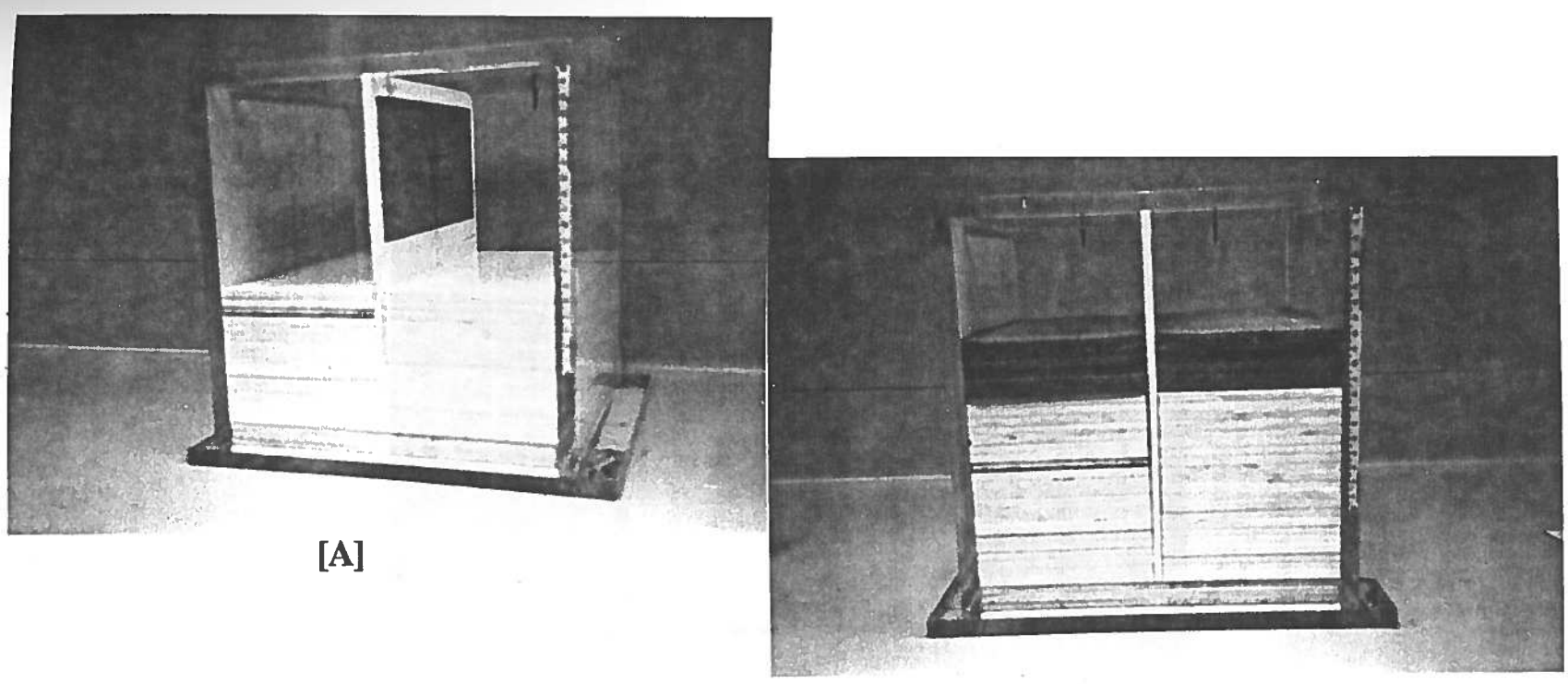

[A] [B]

FIGURE 10. Pictures [A] and [B] displaying the different stages of the phantom construction.

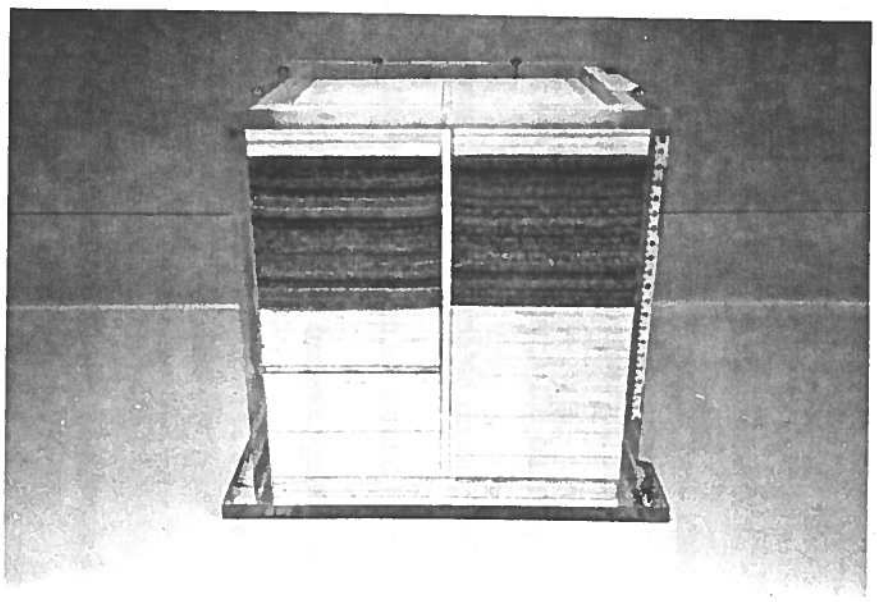

FIGURE 11. Picture of the final phantom ready for the experiment.

utilized as anterior chest wall for fabricating the phantom of this study. The windows have 1 cm of polystyrene on both sides and variable depths ranging from 10 cm to 20 cm. The windows were then closed by corresponding cork sheets of the same dimension. Holes for TLD placement were drilled along the central axis from the surface to variable depths, the deepest one being at 24.5 cm.

The polystyrene slab with the window was then vertically placed at the center of the phantom, between the horizontally placed polystyrene and cork, on both sides. The thickness of the horizontally placed cork slabs were of the exact depth of the corresponding cork window of the vertical slab. At the top of the cork slab, 1.5 cm of polystyrene was placed to match the build-up region. This arrangement gave a uniform thickness of cork of variable depths, simulating lung tissue and 1.5 cm of polystyrene as the build-up region all around the phantom. This vertical polystyrene slab with the window and other interchangable and horizontally placed polystyrene and cork slabs allowed the construction of a wide range of phantom geometries with different lung depths.

For simulating tumor inside the lung, a 2 x 2 x 0.625 cm piece of polystyrene was cut. Corresponding holes were made at the middle of the cork window. Holes were drilled along the central axis and both sides of the tumor for TLD placement.

C) Phantom CT Scan

A thorough CT scan was done before doing any dose measurements. This was done to ensure that the relative electron density converted from CT number for cork simulating lung tissue, and for polystyrene simulating soft tissue, represent the

true state of the phantom during measurement. Also, the effect of holes with TLDs, if any, on CT numbers and the corresponding electron densities were observed. Figures 12A and 12B show a CT image of the sagittal midplane of the lung phantom. Average CT numbers for various regions were determined. These CT numbers are given in Table 6.

In the build-up region of polystyrene, the average CT number ranged from -5.0 to -14.0. In the simulated lung, (cork region) the average CT number ranged from -830.0 to -790.0. For the polystyrene beyond the lung, the average CT number ranged from -10.0 to -5.0. All numbers are in Hounsfield units (HU). This data agrees well with the CT numbers measured previously and represents a relative electron density of 1.008 and 0.15, respectively, for polystyrene and cork. Along the central axis, where holes and TLD's are present, the average CT number in the build-up region was -30.0, indicating a slight presence of air between the polystyrene slabs. In the simulated lung (cork region), the average CT number was -820.0, again indicating a slight presence of air between the cork slabs. In the polystyrene beyond the lung, the average CT number along the central axis was -5.0 to -11.0. Above all, no significant difference is seen in CT numbers due to the placement of TLDs inside the phantom, indicating there should be negligible or no perturbation due to the presence of the TLDs in the radiation field, on the dose distribution, inside the phantom.

2. Phantom Irradiation Technique

Measurements were performed with 6 MV and 15 MV x-ray beams from a

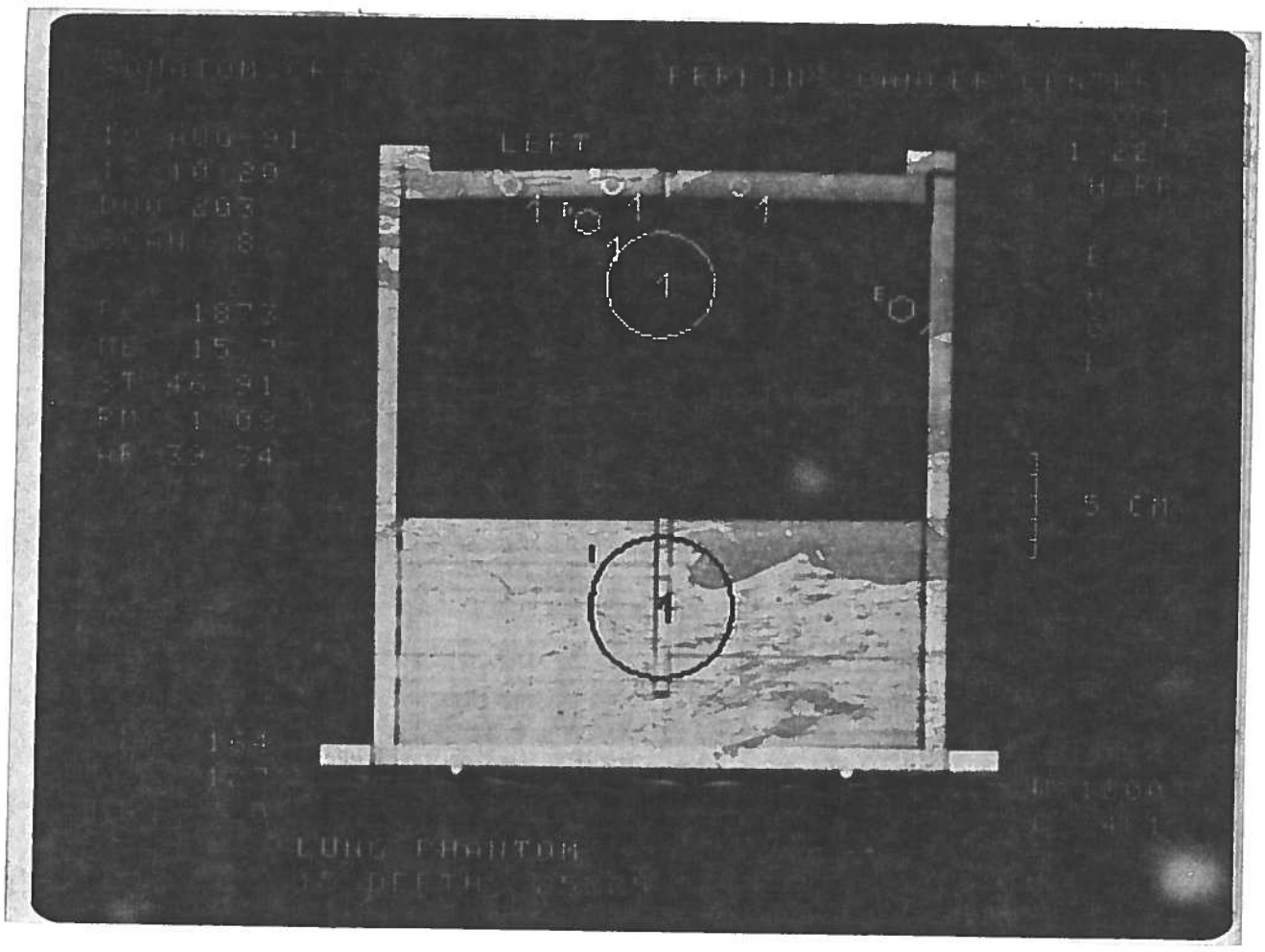

FIGURE 12A. A CT image of the midsagital plane of phantom is shown. At the top is 1.5 cm of polystyrene for build-up, below is the cork simulating lung region. Below the cork a polystyrene again is used for simulating soft tissue. In the middle a vertical polystyrene slab with TLDs placed along the central axis can be seen. The average CT numbers over different regions of interest is extracted and is given in Table 6.

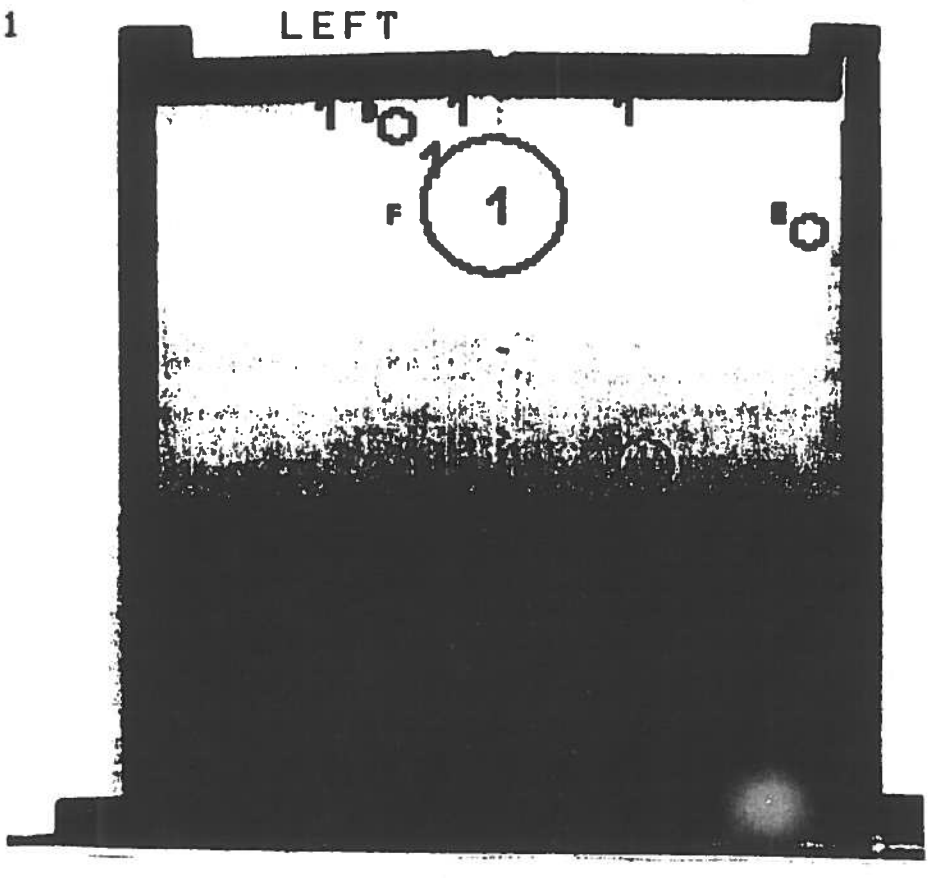

FIGURE 12B. A negative CT image of midsagital plane of the lung phantom is shown here. At the top 1.5 cm of polystyrene, in the middle cork simulating lung and at the bottom polystyrene simulating soft tissue is shown. In the middle a vertical poly slab with TLDs placed along the central axis is also seen. Average CT numbers of different regions of interest is extracted and is shown on Table 6.

TABLE 6

Listing of average CT numbers [HU] of different regions of a midsagital section from a CT image of lung phantom.

REGION IDENTIFICATION	DESCRIPTION OF REGION	AVERAGE CT NUMBER [HU]
A	IN THE ANTERIOR BUILDUP REGION OF POLYSTYRENE	-14.6
B	IN THE ANTERIOR BUILDUP REGION OF POLYSTYRENE	-14.6
C	IN THE ANTERIOR BUILDUP REGION OF POLYSTYRENE	-11.1
D	IN THE SIMULATED LUNG REGION OF CORK	-809.0
E	IN THE SIMULATED LUNG REGION OF CORK	-805.2
F	IN THE SIMULATED LUNG REGION OF CORK	-808.4
G	IN THE SIMULATED LUNG REGION OF CORK	-809.8
H	IN THE SIMULATED LUNG REGION OF CORK	-806.4
I	IN THE POLYSTYRENE BELOW CORK REGION	-15.0
J	IN THE POLYSTYRENE BELOW CORK REGION	-8.9

Varian Clinac 600C and a Clinac 20, respectively. All measurements were made at a fixed SSD or a fixed SAD of 100 cm. The experiments were carried out with the field sizes ranging from 5 x 5 cm to 20 x 20 cm. TMR values measured in an homogenous polystyrene phantom for these beams are given in Table 7. Graphs based on these values were shown before in Figures 6 and 7.

The geometries studied are shown in Figures 13 and 14. Figure 13 is a simple layer geometry which has been used extensively to test correction techniques by many investigators. The buildup region of polystyrene $T_{B.U.}$ is used to simulate chest wall to obtain electronic equlibrium before entering into the low density cork layer. The thickness of the low density cork layer was either 10 cm or 20 cm. The lateral extent of all layers is 25 x 25 cm, which exceeds the largest field sizes used of 20 x 20 cm by an amount necessary to achieve full scatter condition at the central axis.

Figure 14 shows a simulated tumor in lung geometry containing a piece of polystyrene in the center of the low density cork material. The dimension of the tumor was kept at constant 2 x 2 x 0.625 cm. The distance of the tumor from the surface of the phantom varied correspondingly with the different depth of lung, as it was placed at the center of the lung.

3. Thermoluminescent Dosimetry

A) TLD System Setup

Thermoluminescent dosimetry was the choice for this project, due to its many

TABLE 7

TMR values for a 5 x 5, 10 x 10 and 20 x 20 cm field for 6 MV x-rays from the Clinac 600C, up to 20 cm depth are shown. All values are normalized to the d_{max} values for the respective field size.

	6 MV X-RAY (d_{max} = 1.5 cm)		
DEPTH (cm)	**5 x 5 cm**	**10 x 10 cm**	**20 x 20 cm**
0.3	0.44	0.48	0.56
0.5	0.58	0.72	0.81
1.0	0.95	0.96	0.97
1.5	1.00	1.000	1.000
2.0	0.99	0.99	0.99
2.5	0.975	0.98	0.98
3.0	0.96	0.97	0.97
5.0	0.90	0.925	0.93
10.0	0.73	0.77	0.81
15.0	0.58	0.63	0.68
20.0	0.46	0.51	0.57

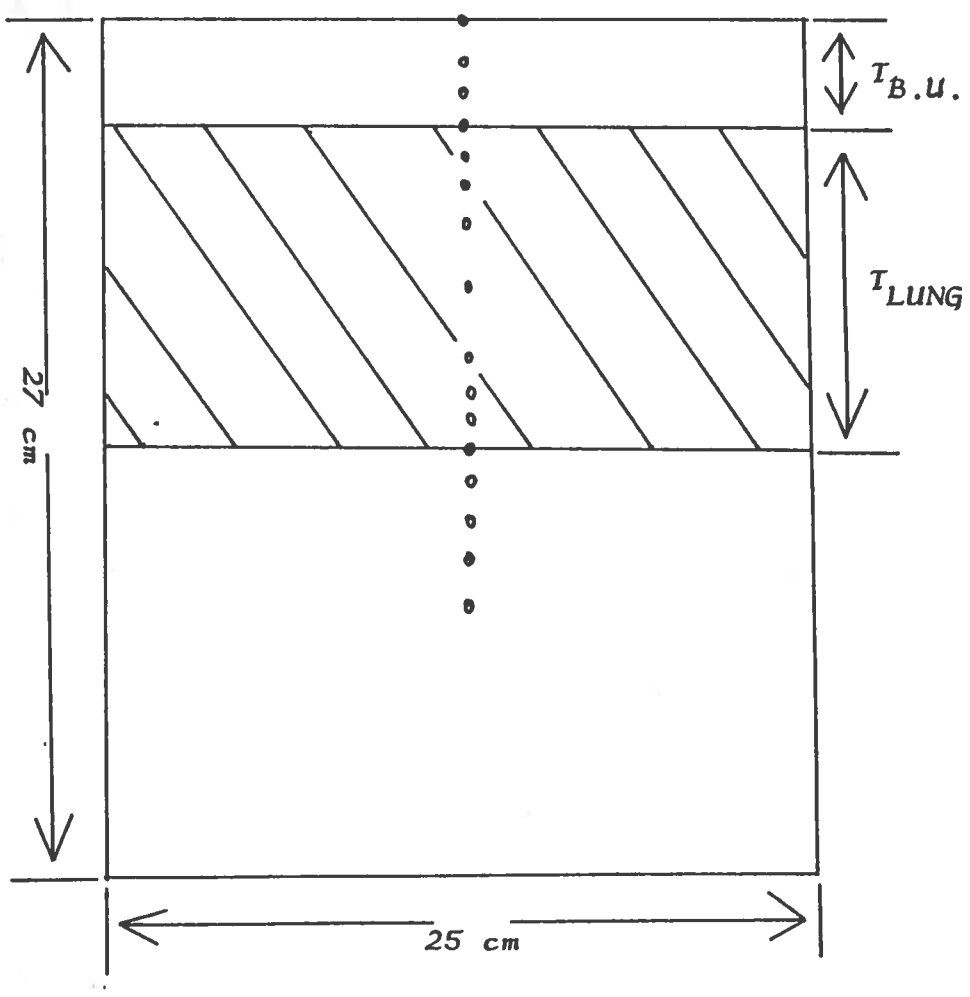

FIGURE 13. This is a simple layer geometry phantom. $T_{B.U.}$ is the thickness of the build-up region, which is kept at 1.5 cm. T_{LUNG} is the thickness of simulated lung cork region, the thickness of this region varied from 10 to 20 cm. The density of this cork region is 0.15 [relative electron density]. The placement of TLDs are shown along the central axis circles.

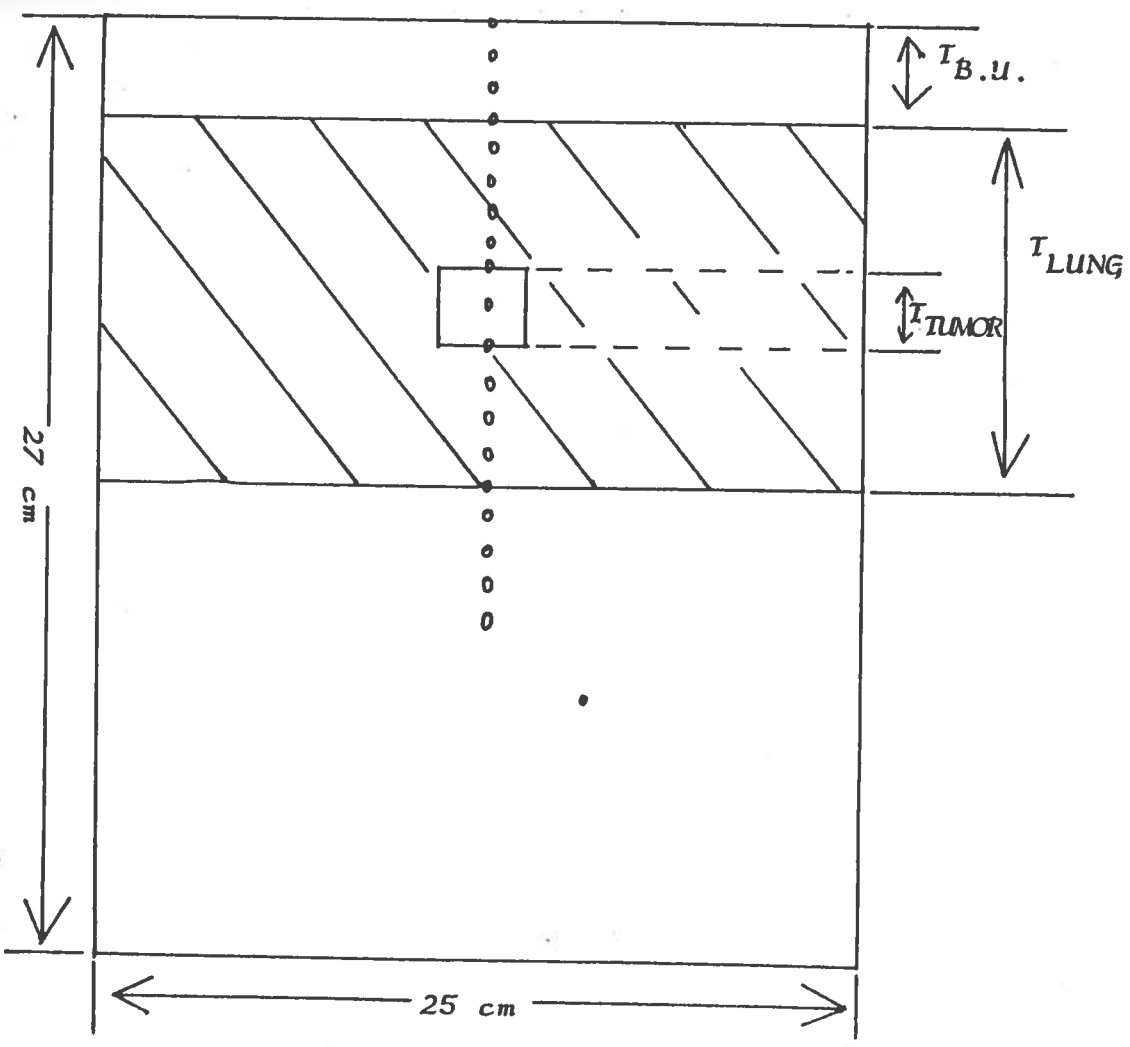

FIGURE 14. This is a tumor geometry phantom, $T_{B.U.}$ is the thickness of the build-up region, T_{LUNG} is the thickness of lung, which varied from 10 to 20 cm. T_{TUMOR} is the thickness of the tumor at the middle of simulated lung. The tumor is 2 x 2 x 0.625 cm thick. The placements of TLDs along the central axis is shown by circles.

used. This same aluminium tray then can be used for annealing purposes. Seasoning of the tray is necessary to avoid contamination of TLD rods by a freshly machined, chemically reactive alumunium tray. Dosimeters can then be placed in a polystyrene tray with shallow holes and irradiated uniformly by a large field. From this procedure a relative factor for the sensitivity of each dosimeter can be determined by comparing the ratios of the individual TLD response to that of the average response for the entire batch.

The annealing, irradiation and readout sequence practiced at MBPCC is followed for this work; LiF is to anneal at 400 degrees centigrade for 1 hour and at 80 degrees for 24 hours before irradiation, and finally to wait 24 hours after irradiation before readout. It is important that all TLD dosimeters and calibrations undergo the identical anneal and readout cycle. The dose response curve for all TLD phosphor is nearly linear only over a limited dose range. For LiF, the TLD response increases linearly with dose up to a value of 10 cGy and then increases with dose by a power greater than unity. For this reason, the calibration should be performed in approximately the same dose range as that intended for use.

All TLD rods were annealed before irradiation at 400 degrees centigrade for one hour followed by 80 degrees centigrade for 24 hours. TLD rods were annealed in a heat seasoned aluminium planchet (Figure 15). After irradiation, the rods were sent to M.D. Anderson Hospital, Houston, Texas, to be read by a TLD reader, a Harshaw 2000, greatly modified in-house (MDAHH). For readout procedure, the phosphor is heated electrically and the intensity of resulting luminescent is measured

[A]

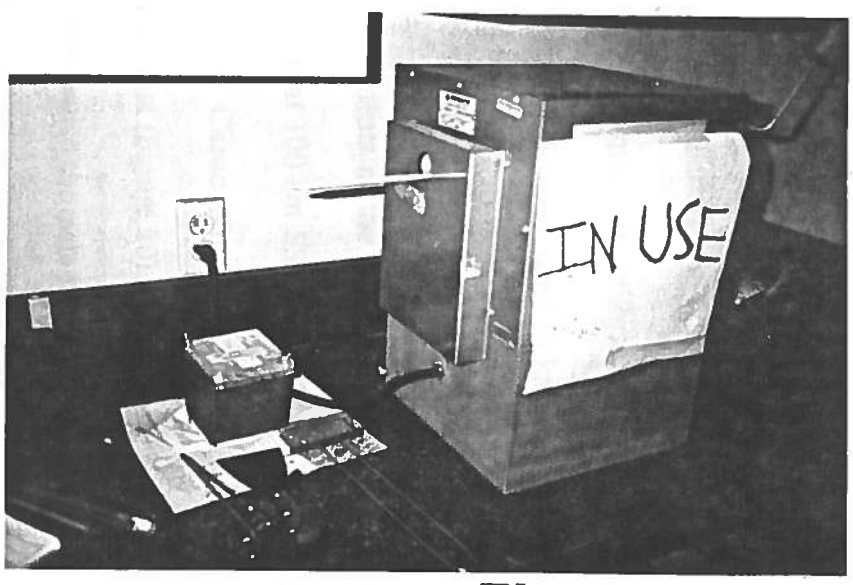

[B]

FIGURE 15. Pictures showing different materials used for TLD dosimetry. The seasoned aluminum planchet and the poly phantom and the vacuum machine are seen in [A]. In [B], the oven is shown.

by a photomultipier tube. The output signal after amplification is applied to a suitable readout instrument, such as a digital voltmeter and expressed in an appropriate unit (ncoul). The instrument is calibrated by measuring the intensity of light from phosphors that have been exposed to known doses of radiation.

B) TLD CALIBRATION

Measurements of the dose response curve were carried out using a 10 x 10 cm field defined at 100 cm SSD using 6 MV x-ray beam on a Clinac 600C and for 15 MV x-ray on Clinac 20. The TLD rods were placed in a clear polystyrene irradiation phantom (Figure 16). The phantom measures 1 x 25 x 25 cm. It contains a middle section which the rods occupy and a 6.73 mm upper section. Additional 0.8 cm and 2.1 cm of clear polystyrene was used to achieve 1.5 and 2.8 cm of buildup region respectively for 6 MV and 15 MV x-rays (Figure 16). Fifty TLDs in a batch were irradiated at a time. The orientation of the phantom with the gantry was kept constant for all the irradiation.

The integral reading in ncoul of all 228 TLDs were divided into classes having an interval of 300. A histogram (Figure 17) based on the occurrence of frequency shows that the maximum frequency occurs in classes 4, 5 and 6. After further removing more TLDs from these classes, it was found that the minimum and maximum response of all TLD of these classes are within +/- 2.5% of the average response. The final selection of 169 TLDs shows a mean value of response in nanocoulomb is 16822.868. The minimum value is 16416.324, 2.5% less than the average value; the maximum value of response is 17242.039, 2.49% higher above the

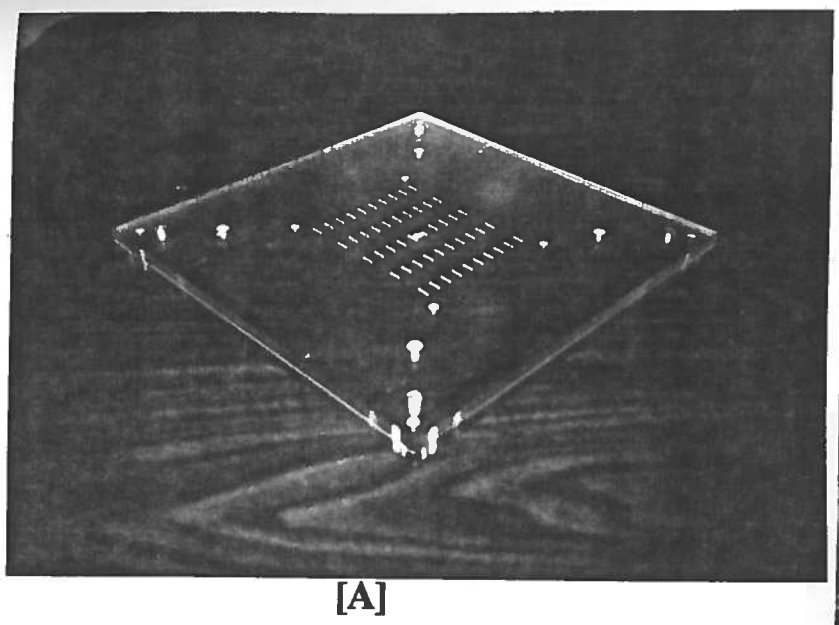

[A]

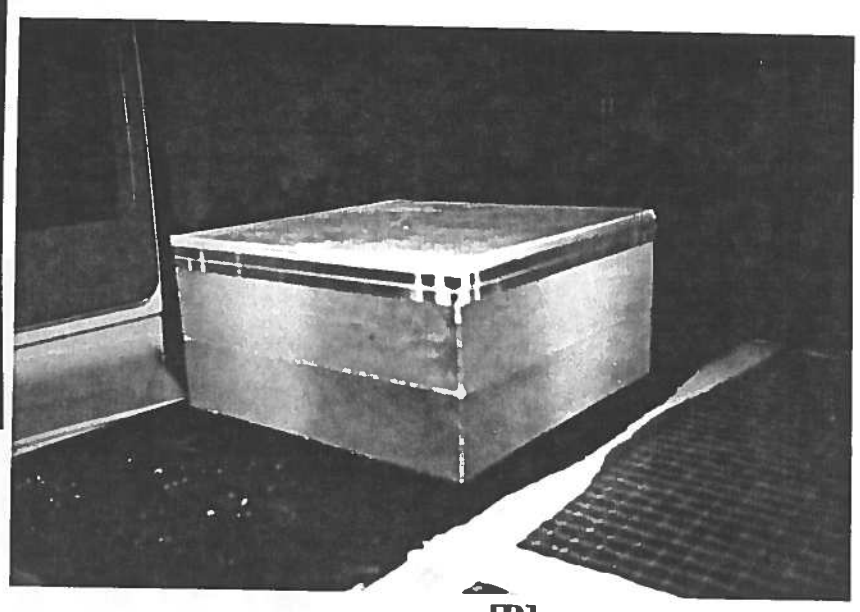

[B]

FIGURE 16. Picture [A] showing the clear polystyrene phantom for TLD irradiation during calibration. Picture [B] shows the setup for TLD irradiation for calibration.

average. A histogram of the selected TLDs frequency of occurence is shown in Figure 18.

The mean response value in ncoul was divided by the response of each of the selected TLDs to determine the sensitivity correction factor for the individual rods. The response from an exposure was then mutiplied by the sensitivity of the rod to obtain a corrected reading. A dose response curve was generated for each energy, 6 MV and 15 MV x-rays. The slope of that curve was then used for calculating the dose of other TLDs of the experiment.

C) TLD Readout and Data Analysis

TLD-100 Harshaw rods were placed in the holes drilled along the central axis of irradiation of the phantom. The TLDs were 1 x 1 x 6 mm and the holes drilled were 1.6 mm in diameter. Experiments and measurements were done on different days. A dose of 200 cGy was delivered at d_{max} for all the experiments. A total of sixteen experiments were done; eight experiments without tumor and the remaining eight experiments with tumor in the middle of the lung. Two different photon energies, 6 MV and 15 MV, two field sizes 5 x 5 and 20 x 20 cm, and two depths of lungs 10 and 20 cm were used. Necessary corrections for field size dependency in air (FSDA) and normalized peak scatter factor (NPSF) and for daily constancy were done in order to calculate monitor units, so that 200 cGy at d_{max} can be given for all experiments.

The TLD readings were converted to dose using the following equation:

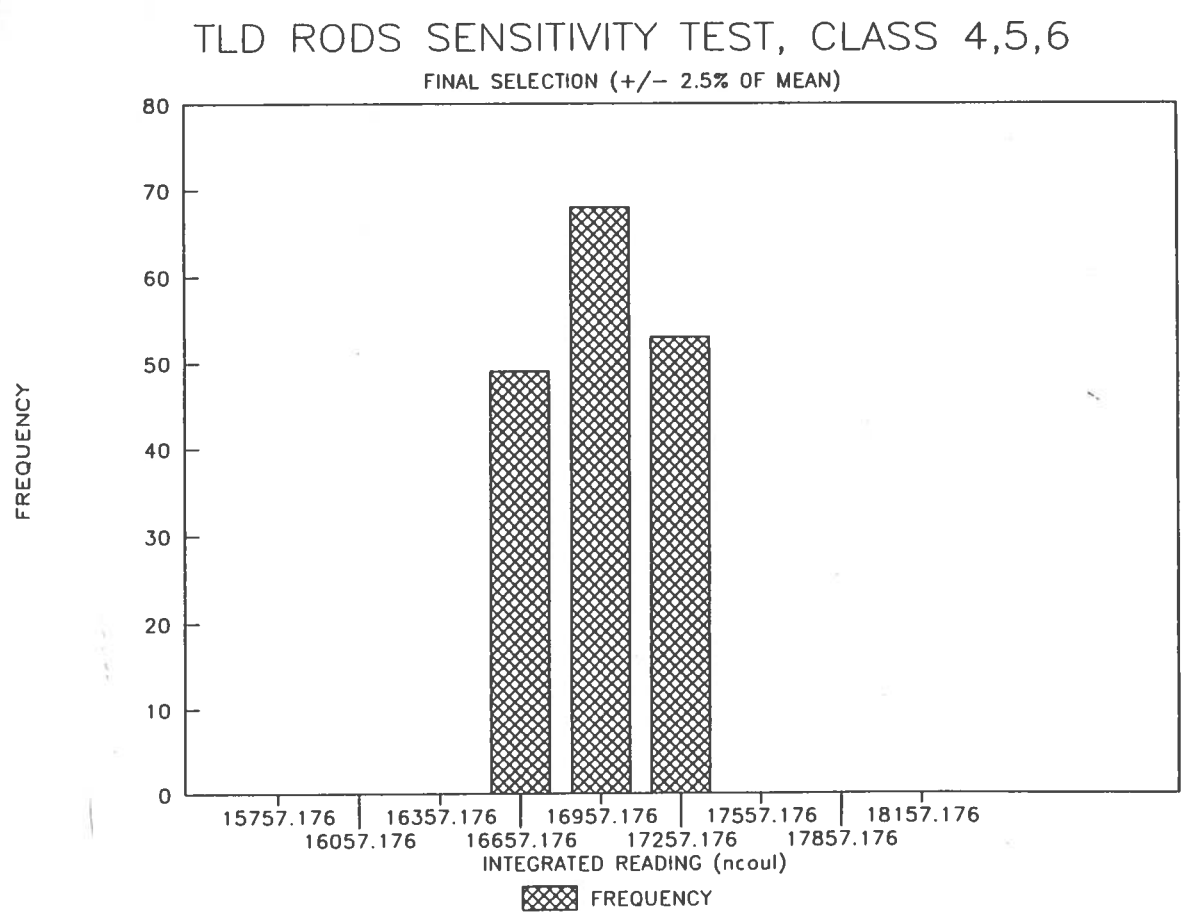

FIGURE 18. **A histogram showing frequency of occurrence of final selected TLDs of classes 4, 5, and 6. The mean value of response of these three classes is 16822.868 (ncoul).**

$$\hat{D} = \left[\frac{RDG^*}{RDG_c}\right]^{1/m} * D_c \,, \tag{8}$$

where RDG^* is the sensitivity corrected reading of the dosimeter, RDG_c is the sensitivity corrected reading of the control *TLD*, D_c is the dose delivered to the control, and $1/m$ is the inverse of the slope of the best fit line, obtained from the respective dose response curve.

The lung phantom TLD readings were then converted to percent depth dose using the following equation:

$$\%dd = \frac{D_{LUNG}[x,y]}{D_{POLY}[d_{max}]} * 100 \,, \tag{9}$$

where D_{LUNG} is the dose at point x,y from lung phantom TLDs and $D_{POLY}\,(d_{max})$ is the dose at central axis maximum from the homogenous polystyrene phantom for the respective field size at the same point.

Dose measurements in polystyrene require only 1% correction for composition and density differences with water (AAPM TG 21 1983). This was verified for 6 MV x-ray beam. Percent depth dose was measured up to 20 cm depth along the central axis of the beam in a homogenous polystyrene phantom using TLD and found to agree within 2% of the percent depth dose measured in water with an acrylic ion chamber, shown in Figure 19.

Lung dose correction factors, (*CF*), were finally calculated as the ratio of the dose in the heterogenous phantom, to the dose at the same point in the water equivalent homogenous polystyrene phantom:

FIGURE 19. **Percent depth dose in polystyrene using TLD dosimeter [continuous line] and using ion chamber [square marks] for a field size 10 x 10 cm^2 up to 20 cm depth, for 6 MV x-rays from the Clinac 600C. The values in polystyrene are always within $\pm$ 2.5% of the water values.**

$$CF = \frac{\textit{dose in heterogenous phantom}}{\textit{dose at same place in homogenous water equivalent polystyrene phantom}} .$$

4. Data Generation from Computer and Hand Calculation

Two contours simulating experimental setups were drawn depicting the two phantom geometries, one without tumor and one with tumor, inside the lung. The contours were then entered into the CAP-PLAN RT110 treatment planning computer by hand digitization. A relative electron density of 1.0 and 0.15 was assigned respectively for soft tissue and lung tissue in the lung phantom contour. The irradiation technique used for experimental TLD measurement was followed to generate the computer data. Percent depth doses for different points, where actual measurements are performed, were then obtained. Depth doses both after heterogeneity correction by effective SSD and generalized BPL and without any heterogeneity correction were gathered. Correction factors (CF) based on these values were also calculated using the formula described in the previous section. Hand calculations were done to obtain correction factors using the modified power law method (MPL).

RESULTS AND DISCUSSION

The results of this study are divided into two sections based upon the energy of irradiation, 6 MV and 15 MV x-rays. These two sections are further divided into field sizes (5 x 5 and 20 x 20 cm), phantom geometries (non-tumor and tumor), and lung depths (10 and 20 cm). Percent depth doses (%dd) and correction factors (CF) based on depth doses were obtained from both measured and calculated data. Graphs showing %dd and CF as a function of depth for different phantom and irradiation parameters were drawn. All %dd and CF graphs are included in Appendix A. The %dd curves are generated by: (1) direct measurement, (2) calculation using BPL, (3) calculation using ESSD, (4) calculation with no heterogeneity correction. The %dd are shown as a function of depth, along the central axis through the lung. The %dd shown are for three different field sizes (5 x 5, 10 x 10, and 20 x 20 cm), two lung depths (10 and 20 cm), and two x-ray energies (6 and 15 MV). Figures 20 and 21 are examples drawn for a 5 x 5 cm field size using 6 MV and 15 MV.

The shaded areas in the graphs represents unit density polystyrene (simulating soft tissue and tumor) and the non-shaded area represents low density cork (simulated lung).

1. 6 MV X-RAYS

Figures 22 and 23 show the measured and calculated correction factors (BPL and ESSD) as a function of depth. For 10 cm lung depths (Figure 22, [A] and [B]),

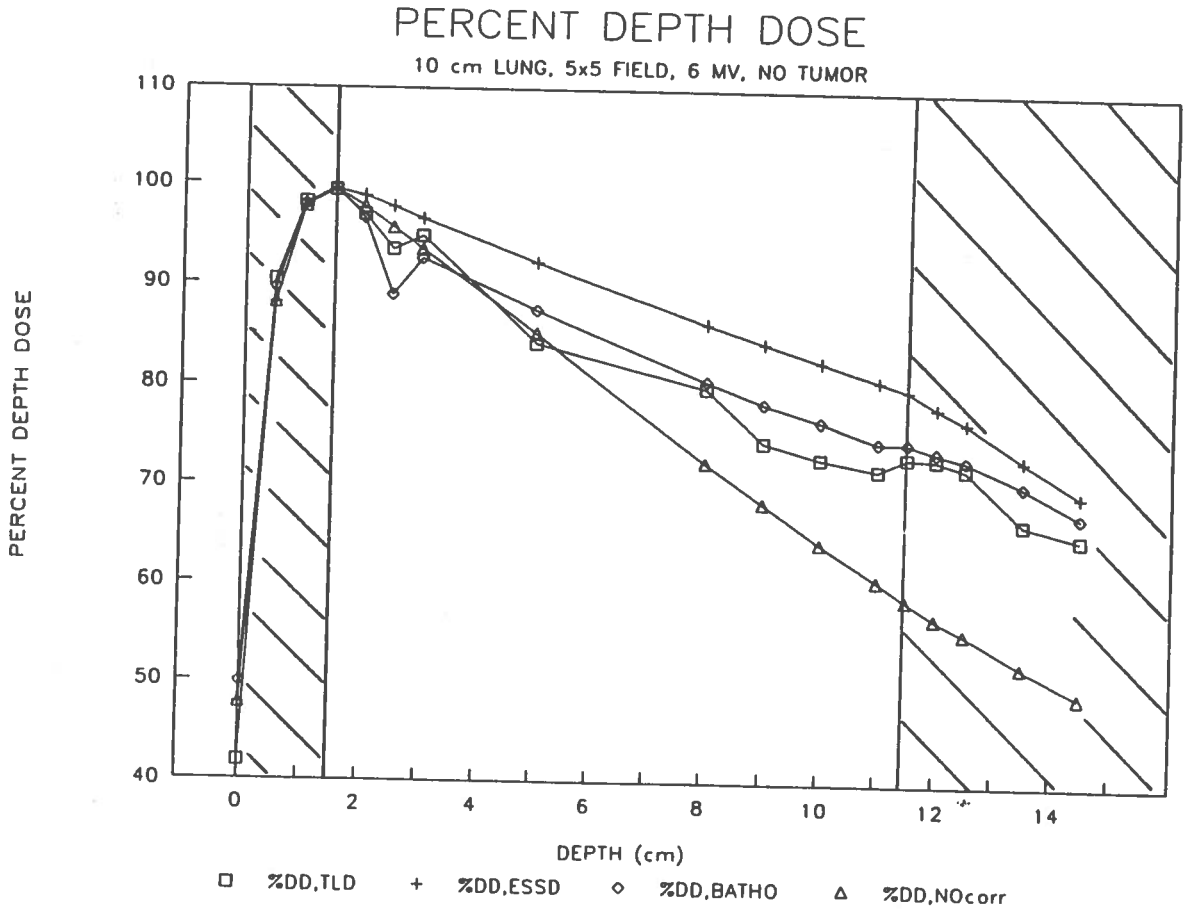

FIGURE 20. **Measured and calculated central axis percent depth dose for a 6 MV x-ray from a Clinac 600C for a 10 cm thick non-tumor lung phantom composed of cork with 1.5 cm overlay of build-up. The field size is 5 x 5 cm.**

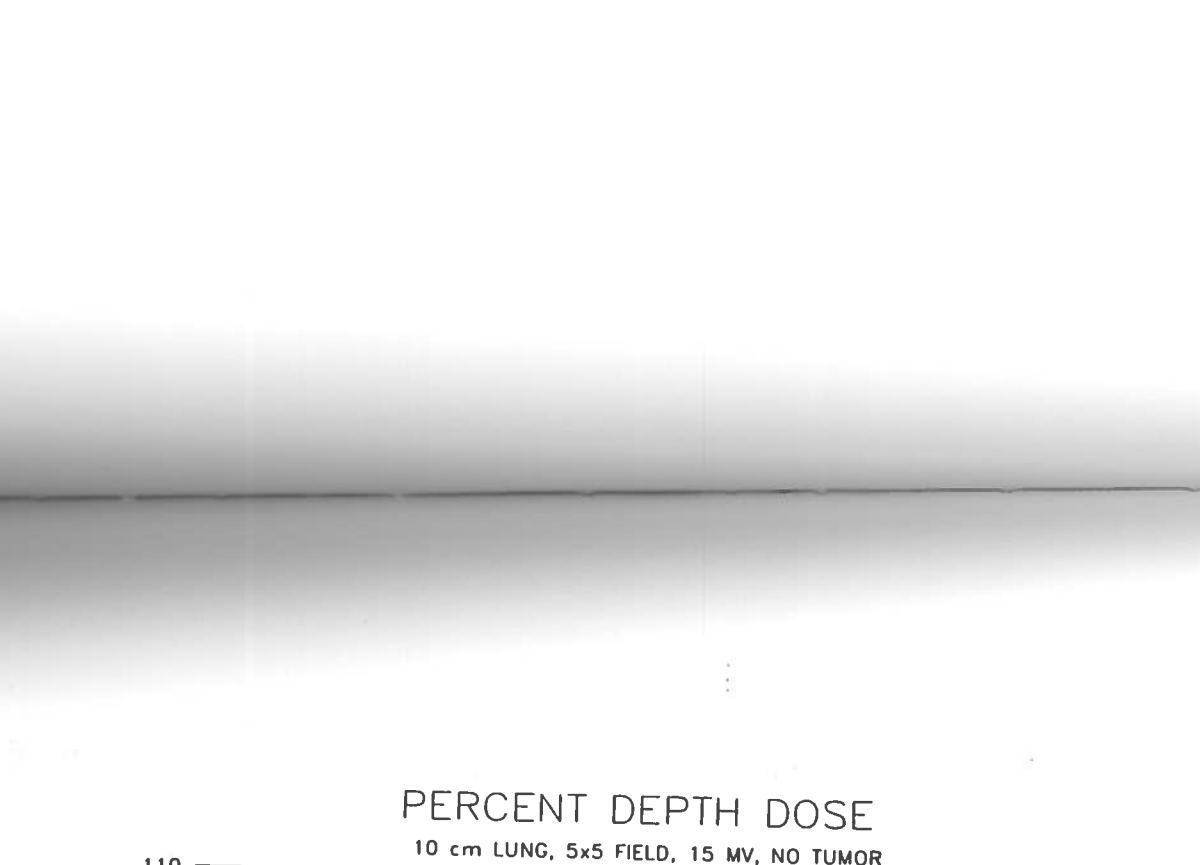

FIGURE 21. **Measured and calculated central axis percent depth dose for a 15 MV x-ray from a Clinac 20 for a 10 cm thick non-tumor lung phantom composed of cork with 1.5 cm overlay of build-up. The field size is 5 x 5 cm.**

FIGURE 22. Correction factors for 6 MV x-rays, 10 cm lung depth for [A] non-tumor geometry, and [B] tumor geometry. The depth (cm) is shown in the x-axis and CF is shown in the y-axis.

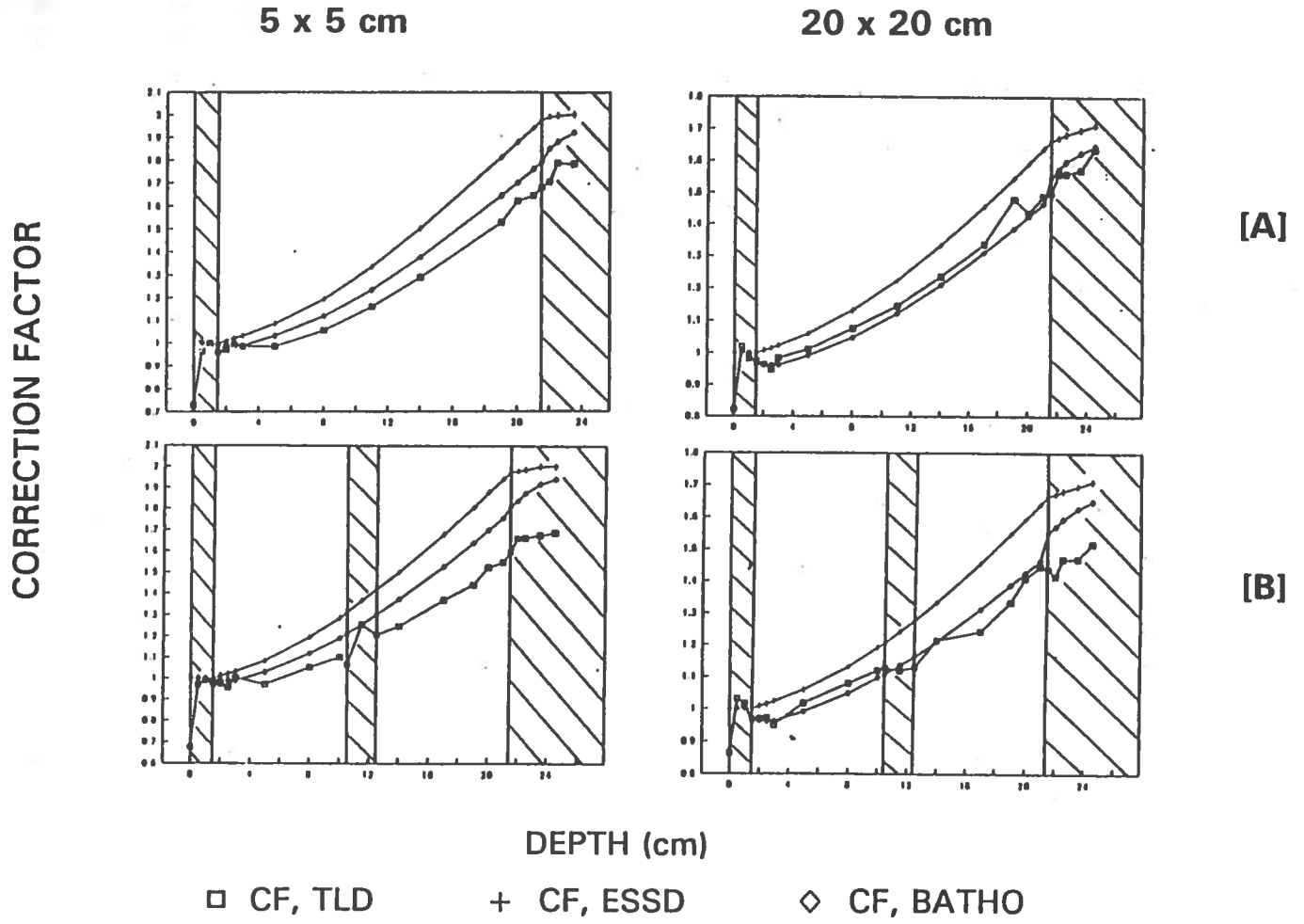

FIGURE 23. Correction factors for 6 MV x-rays, 20 cm lung depth for [A] non-tumor geometry, and [B] tumor geometry. The depth (cm) is shown in the x-axis and CF is shown in the y-axis.

the CFs are for three different field sizes (5 x 5, 10 x 10, and 20 x 20 cm) and for two phantom geometries (non-tumor and tumor). For 20 cm thick lung depth (Figure 23, [A] and [B]) the CFs are for two different field sizes (5 x 5 and 20 x 20 cm) and for two phantom geometries (non-tumor and tumor).

The measured CF for all field sizes, and for both geometries and lung depths increases almost linearly within the low density layer. The slope decreases upon entering the polystyrene layer below the heterogeneity. However, the correction factor decrease as the field size is increased from 5 x 5 cm to 20 x 20 cm. The decrease in CF with increasing the field size is caused by the scatter component of the radiation because the field size does not affect the primary component. Scatter component of the dose in the homogenous water phantom increases more with field size than the corresponding value for the heterogenous phantom situations. This results in smaller CF for the large field sizes than for a small field size (Rice et al. 1988).

The measured CF drops below unity in the first few centimeters in the lung for all field sizes and for both lung depths, resulting from the reduced scatter in the low density cork (simulated lung), which is not yet fully compensated by the increased primary radiation component of the beam.

In Figure 22, [A], for 5 x 5 cm field size, behind the low density cork layer, a partial build-up curve can be seen. As the beam enters a higher density medium from a lower density medium, electronic equilibrium will be re-established (Tang et al. 1986). This results in dose increase at points below the posterior lung interface.

This build-up becomes less prominent as the field size and lung thickness is increased. This observation indicates that the partial build-up depends on the field size, and the thickness of the low density layer in the lung phantom itself (Rice et al. 1988).

The CF calculated by BPL method follows the measured curve in the first few centimeters inside the lung. However, the BPL calculated values are slightly higher than the measured ones for 5 x 5 cm field sizes for both geometries and for both lung depths. As the field size is increased from 5 x 5 cm for both geometries and lung depths, the BPL curve is nearly superimposed on the measured curves and always remain within +/-3% of the measured values. The BPL as a correction method takes into account the primary radiation over the distance between the inhomogeneity that is traversed by the primary beam and the point of calculation. The BPL method also considers the size of the beam and, thus, indirectly accounts for the scatter radiation as corroborated by Sontag and Cunningham (1977). The BPL calculation assumes electronic equilibrium at the point of calculation and, as such, is less accurate for dose calculation in places where there is no electronic equilibrium (Young and Kornelsen 1983). In normal unit density soft tissue below the maximum build-up depth, for all field sizes, transient electronic equilibrium exists along the central axis. Whenever the x-ray beam enters a low density region, however, the effects of lateral electron scatter, combined with increased range of the secondary electrons, causes a significant number of electrons to travel outside the geometrical limits of the beam. This phenomenon degrades the beam profile and, for the smaller fields, results in an

electronic disequilibrium on the central axis. The BPL method is unable to correct for these disequilibria phenomena and predicts doses higher than measured values for a 5 x 5 cm small field where the electronic disequilibria exists. When the field size is increased to 20 x 20 cm, an increasing number of electrons generated mainly in the anterior polystyrene slab and a relatively small number in the increasing volume of irradiated lung, reach the point of calculation and re-establishes the electronic equilibrium. Therefore the BPL method agrees well with the measured values (Epp et al. 1977). This is evident both for 10 and 20 cm depth lung. This observation agrees well with those of Leung et al. (1970), and Tang et al. (1986), who demonstrated that the generalized Batho method is quite accurate for high energy 6 MV to 24 MV x-rays for a 10 x 10 cm field.

The ESSD method continuously gives a higher CF in all situations for both geometry, all field sizes and for both lung depths. This observation is in agreement with El-khatib et al. 1989, and Thomas 1991, who observed over a range of energies from Co-60 to 16 MV x-rays from 5 x 5 cm to 30 x 30 cm field sizes, that the effective SSD method over estimates the CFs. The only exemption is in Thomas data (1991), for 16 MV x-ray in 16 x 16 cm field size, where ESSD method calculated CF agrees well with that of the measured data. This agreement which Thomas (1991), observed for only this particular field size and high energy 16 MV x-ray, may be due to the different phantom geometry, where he used 4 cm of anterior build-up made of polystyrene and a much higher electron dense cork of 0.4 compared to 0.15 in the present study. The over estimation by ESSD continues to increase at the

posterior edge of the lung as the thickness of lung depth is increased. While calculating dose, ESSD accounts for the depth of the point. The ESSD method accounts for increased transmission of the primary radiation caused by low density lung, but measures the scatter radiation coming from the unit density material (El-khatib et al. 1989; Cunningham 1982). The assumption of scattering radiation coming from unit density material, when in reality scattering is reduced due to low density causes the ESSD method to overpredict in all situations.

None of the calculation methods (BPL and ESSD), takes into account the electronic disequilibrium present at the interfaces. Therefore not only do they fail to predict the partial build-up at the posterior interface of the lung, but also at the anterior build-up region.

2. 15 MV X-Rays

Figures 24 and 25 show the measured and calculated correction factors (BPL and ESSD) as a function of depth. The CFs are for two different field sizes (5 x 5 and 20 x 20 cm), two phantom geometries (non-tumor and tumor) and two lung depths (10 and 20 cm).

The measured CF drops below unity in the first few centimeters inside the lung for both field sizes and for both phantom geometries and lung depths. This phenomenon results from the lack of complete build-up in the 1.5 cm layer of polystyrene in front of the cork. So, the lung is underdosed especially for small lung, and small field size. For a small field size (5 x 5 cm) and a small lung (10 cm) in

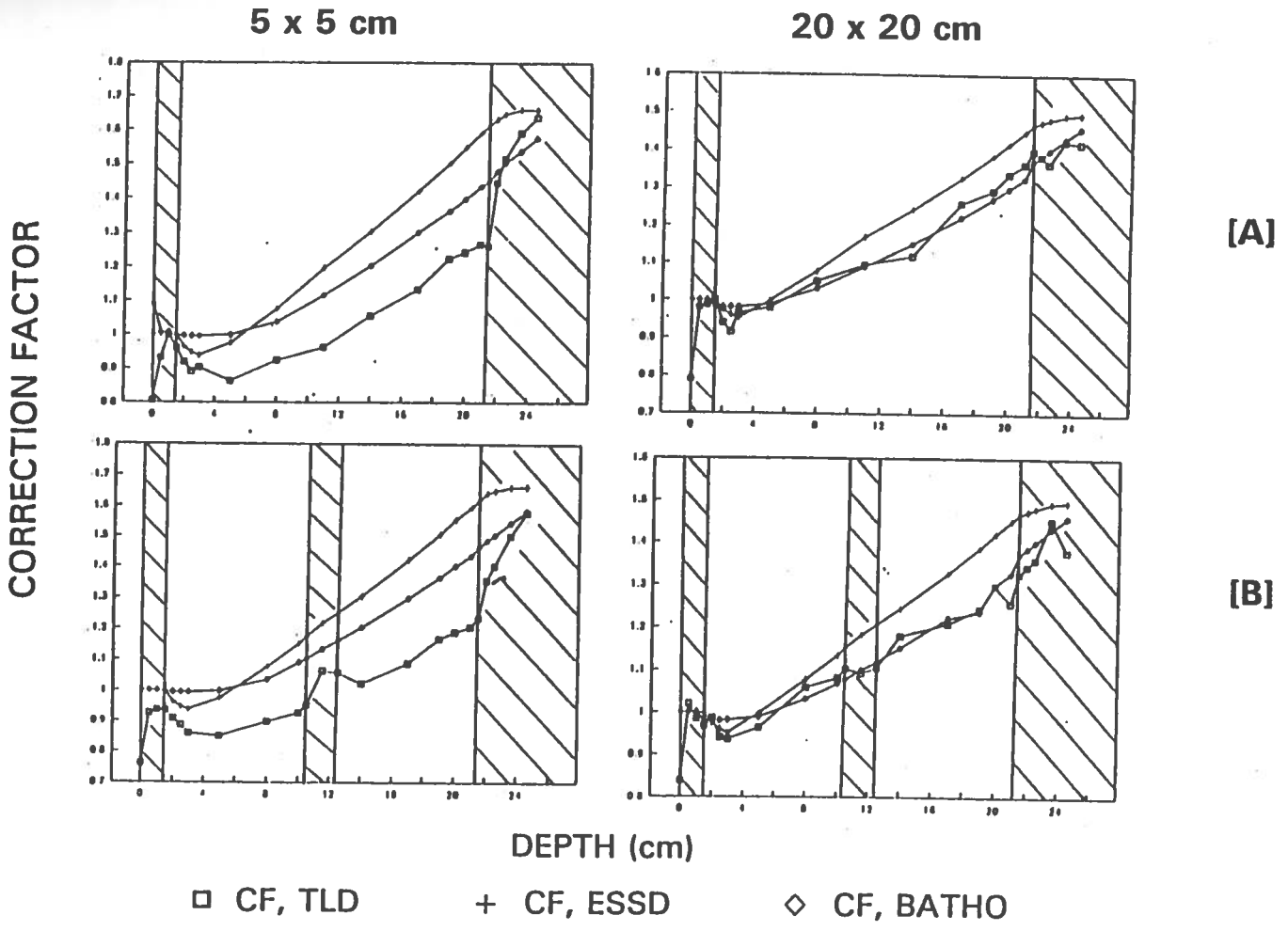

FIGURE 24. Correction factors for 15 MV x-rays, 10 cm lung depth for [A] non-tumor geometry, and [B] tumor geometry. The depth (cm) is shown in the x-axis and CF is shown in the y-axis.

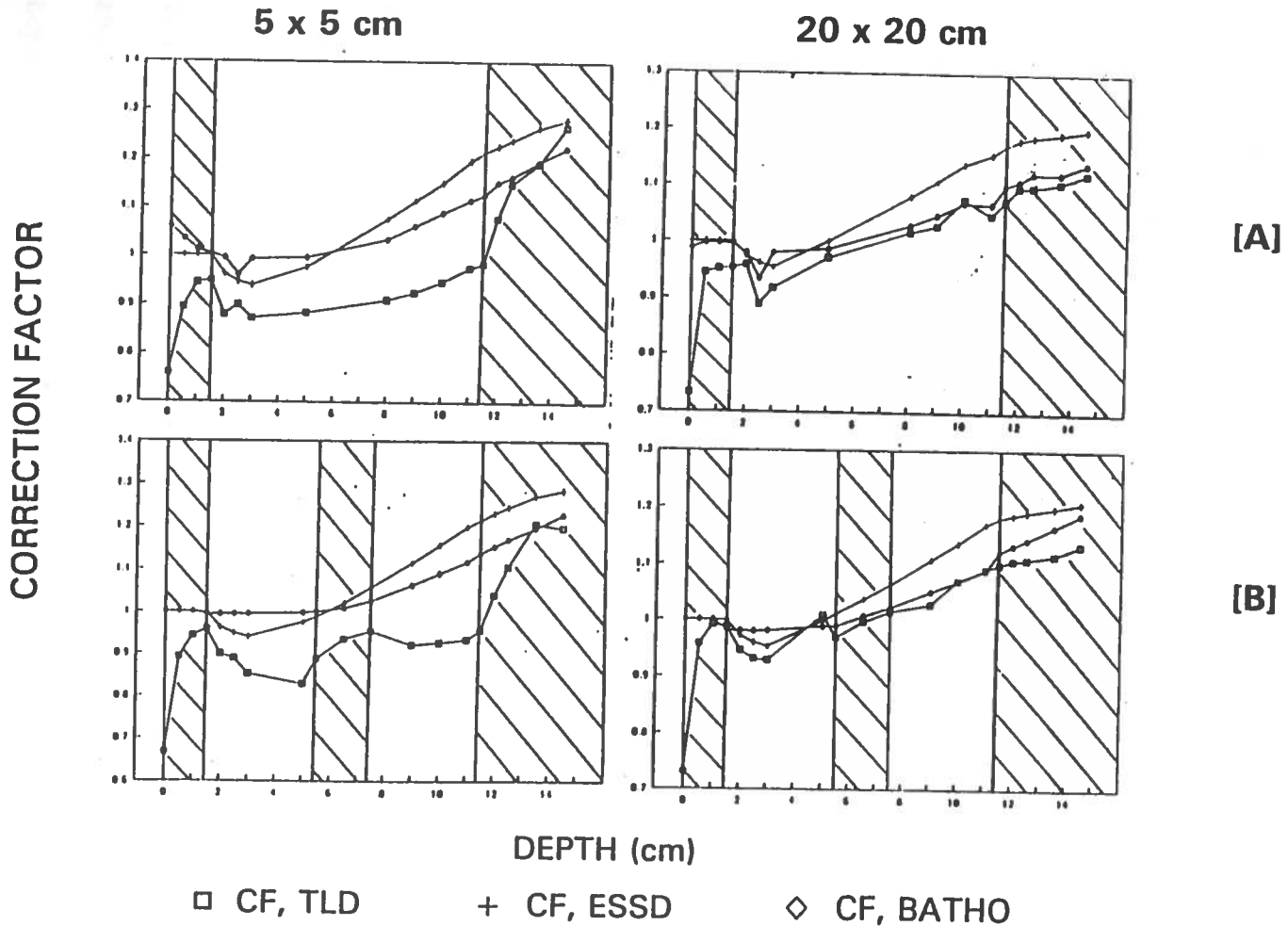

FIGURE 25. Correction factors for 15 MV x-rays, 20 cm lung depth for [A] non-tumor geometry, and [B] tumor geometry. The depth (cm) is shown in the x-axis and CF is shown in the y-axis.

Figure 24 [A]) there is a 10% underdosing at the middle of the lung, but the effect becomes less pronounced as the field size increases to 20 x 20 cm (Figure 24 [B]).

A significant drop of measured CF occurs throughout the lung for the small 5 x 5 cm field size due to the lack of the lateral electronic equilibrium. Small field size 5 x 5 cm is of particular interest because CF always remains below unity throughout the lung, indicating that the electronic equilibrium is never established and causes a significant dose reduction inside the lung.

As the field size is increased, more secondary electron originates both from the anterior polystyrene slab, and from the increased irradiated volume of lung. Behind the low density layer, for 5 x 5 cm field sizes in both lung geometries and depths, a partial build-up can be seen. This build-up becomes less prominent with larger 20 x 20 cm field sizes.

In the tumor volume a partial build-up can be seen in the 5 x 5 cm field size, indicating that the dose at the surface of the tumor will be less than in the middle of the tumor. The maximum difference is observed in Figure 25, [B], for a 5 x 5 cm field size, where the tumor surface dose is 10% less than the dose from the middle of the tumor. As the field size is increased to 20 x 20 cm for both geometries and lung depths, the BPL curve is nearly superimposed on the measured curves and always remains within +/-3% of the measured values, and is true for volumes in and beyond the lung.

The ESSD method continuously gives a higher calculated CF in all situations for both geometries, field sizes and lung depths. As explained before, the ESSD

method does not allow for the reduced scatter from the lower density material surrounding the point of calculation and consequently predicts a higher CF. The ESSD curves overestimate the CFs above the measured and BPL calculated values.

None of the calculation methods takes into account the electronic disequilibrium, and as such, both fails to predict the partial build-up in tumor volume and the posterior interface of the lung.

The results for both 6 MV and 15 MV x-ray energies of all experiments show that BPL predicted values, while disagreeing with measured values in small 5 x 5 cm field sizes, agrees with measured values in large 20 x 20 cm fields. This indicates that the BPL method works well when the electronic equilibrium (lateral and longitudinal) exists inside the low density lung material. The average maximum longitudinal range of an electron released by 6 MV x-ray is 1.5 cm (equal to d_{max}) in a homogenous water phantom. The longitudinal range will be further extended in a low density medium. In cork with a density of 0.15, the longitudinal range of an electron released by 6 MV x-ray will be approximately 10 cm. The electrons scattered laterally will have 1/3 to 1/2 of this 10 cm longitudinal range, approximately 3 to 5 cm. A field size equal to twice this lateral range, 6 to 10 cm, is necessary to achieve electronic equilibrium at the central axis of the beam, which will also maximize the dose along the central axis (Mackie et al. 1985). The agreement of the BPL predicted values with that of the experimental measured data shown in Appendix A indicated that for 6 MV x-ray, a 10 x 10 field size is sufficient for having electronic equilibrium inside 0.15 low dense lung material.

From Appendix B, Tables B-1 through B-7 show the results of hand calculated CFs using the modified power law algorithm (Thomas 1991). The CFs are calculated for the two x-ray energies used in this work (6 MV and 15 MV), three field sizes (5 x 5, 10 x 10, 20 x 20 cm), and two lung thicknessess (10 cm and 20 cm). This algorithm takes into account the longitudinal electronic disequilibrium by adding the build-up depth to all depths before calculating tissue maximum ratios (TMRs), which in turn is further used to calculate the CFs. The results show that the modified power law heterogeneity correction method overpredicts the CFs, in all situations calculated for both energies. This is true for points both inside and beyond the lung, and also near the interfaces. This overprediction of the calculated CFs are always more than 5%, except in two cases at 8 cm and 22 cm depths, for a 20 x 20 cm field size and for a 6 MV x-ray seen in Table B-5. In most cases, the overprediction of CFs calculated by modified power law method is far from the accuracy of +/- 2% which has been reported by Thomas (1991). Maximum overprediction of 24% is found in Table B-6 at 10 cm depth for a 5 x 5 field size for 15 MV x-rays. The reason for the disagreement between the hand calculated CF (modified power law) and the measured ones is unknown. It is probably that the different phantom geometry may have caused this discrepancy. Whereas Thomas (1991) used 4 cm of anterior build-up of polystyrene and cork with relative electron density of 0.4, in the present study 1.5 cm of polystyrene and 0.15 dense cork is used.

CONCLUSIONS

This study attempts to examine in detail the variation of percent depth dose and lung dose correction factor along the central axis of an x-ray beam for two geometries and two energies. Percent depth doses in lung-equivalent materials were measured in phantoms having dimensions and densities resembling those of human thorax region. The dose measurements were compared to calculations performed, using the lung correction algorithms available on a CAP-PLAN RT100 treatment planning computer and with hand calculations to evaluate calculation methods and develop recommendations. Although a large amount of data is presented, the main observations are summarized as follows:

1. If no correction is done for the presence of low density lung tissue and a dose calculation is performed assuming unit density throughout, the error in dose can be as high as 70%.
2. With 6 MV x-rays for a small lung the maximum correction factor inside the simulated lung goes from 1.3 for a 5 x 5 cm field size, to 1.1 for a 20 x 20 cm field size. For a large lung the correction factor goes from 1.7 for a 5 x 5 cm field size to 1.5 for a 20 x 20 cm field size.
3. With 15 MV x-rays and a small lung the maximum correction factor inside the simulated lung increases from 0.95 for a 5 x 5 cm to 1.05 for a 20 x 20 cm field size. For a large lung the correction factor increases from

1.25 for a 5 x 5 cm field size to 1.40 for a 20 x 20 cm field size.

4. A partial build-up curve can be observed at the posterior interface of the lung, because electronic equilibrium was lost at the low density lung tissue. This build-up is dependent upon field size, beam energy, and lung depth.

5. If there is no full build-up layer present in front of the lung, then the dose will be lowered in the lung itself until full build-up is achieved.

6. Equivalent SSD method (ESSD) of heterogeneity correction overpredicts the correction factor in all the situation studied in this project.

7. The generalized Batho power law method (BPL) of heterogeneity correction overpredicts the correction factor by about 8% inside the lung for the 5 x 5 cm field size at the low energy. The BPL overprediction becomes larger about 18% with 15 MV x-ray energy. When the field size is increased from 5 x 5 to 20 x 20 cm, BPL method gives good results, for 6 MV and 15 MV x-ray energies, within a range of +/-3% of the measured values.

8. The modified power law (MPL) inhomogeneity method of Thomas does not give the desired accuracy of the 2% as have been reported earlier. The MPL overpredicts the CF for all field sizes of 5 x 5, 10 x 10 and 20 x 20 cm for both 6 MV and 15 MV x-ray energies. The overprediction of CFs mostly ranged from 5 to 24%.

9. The measured dose distribution and correction factor for tumor layer

geometry is similar to that of the non-tumor layer geometry.

10. For small field size and for both 6 MV and 15 MV x-rays, a partial build-up region in the tumor can be observed resulting in a maximum reduction of 10% dose at lung-tumor interface compared to the center of the tumor.
11. The effective SSD method (ESSD) continuously overestimated the CF in all situations. The magnitude of difference between measured and ESSD calculated CF decreases with increasing field sizes.

RECOMMENDATIONS

Based on the data presented in this study, several recommendations are made as follows:

1. Dose correction for low density lung tissue may be routinely employed for the purpose of dose calculations for radiotherapy in the thoracic region.
2. Generalized Batho power law correction method should be selected for heterogeneity dose correction, as it was found to be superior over the effective SSD method and the modified power law method of Thomas, in all the experimental and calculational situations.
3. An awareness of the limitation of the various correction methods is necessary, knowing when it will underpredict or overpredict the lung dose in a different situation.
4. High energy 15 MV x-rays are not recommended for irradiation of the thorax, because it will cause electronic disequilibrium within the lung leading to significant underdosing.
5. Future studies with different experimental geometries and lung densities should be performed in order to completely understand dose distribution inside and beyond the lung. Also, the predictability of any computer correction algorithm under different clinical situations should be evaluated for better appreciation of their performance in heterogeneity dose correction.

REFERENCES

Attix, F.H.: Introduction of Radiological Physics and Radiation Dosimetry, pp. 395-411, Wiley-Interscience Publication, New York, 1986.

Batho, H.F.: Lung Corrections in Cobalt-60 Beam Therapy. *J Can Asso Radiologists*, **15**:79-83, 1964.

Battista, J.J., Rider, W.D., Van Dyk, J.: Computed Tomography for Radiotherapy Planning. *Int. J. Radiation Oncol. Biol. Phys.* **6**:99-107, 1980.

Cap-Plan Radiation Treatment Planning Systems, Operator's Manual, pp.2-4 to 2-5. Mary Bird Perkins Cancer Center, Baton Rouge, Louisiana, total pp. 6-83.

Cember, H.: Introduction to Health Physics, 2nd Edition, pp. 261-262, Pergamon Press, New York, 1989.

Constantinou, C.: Personal Communication, 680 Centre Street, Brockton MA 02402, 1991.

Cunningham, J.R.: "Tissue Inhomogeneity Corrections in Photon-Beam Treatment Planning", in Progress in Medical Radiation Physics, edited by C. G. Orton (Plenum, New York, 1982), Ch. 2.

Ekstrand, K.E., Barnes, W.H.: Pitfalls in The Use of High Energy X-rays to Treat Tumors in the Lung. *Int. J. Radiation Oncol. Biol. Phys.* **18**:249-252, 1990.

El-Khatib, E., Battista, J.J.: Accuracy of Lung Dose Calculations for Large Field Irradiation With 6 MV X-rays. *Med. Phys.* **13**:111-116, 1986.

El-khatib, E.E., Evans, M., Marina Pla, Cunningham, R.J.: Evaluation of Lung Dose Correction Methods for Photon Irradiation of Thorax Phantoms. *Int. J. Radiation Oncol. Biol. Phys.* **17**:871-878, 1989.

Epp, E.R., Boyer, A.L., Doppke, K.P.: Underdosing of Lesions Resulting from Lack of Electronic Equilibrium in Upper Respiratory Air Cavities Irradiated by 10 MV X-Ray Beams. *Int. J. Oncol. Biol. Phys.* **2**:613-619, 1977.

Geise, R.A., McCullough, E.C.: The Use of CT Scanners in Megavoltage Photon Beam Therapy Planning. *Radiology* **12**:133-141, 1977.

Horton, J.L.: Handbook of Radiation Therapy Physics, pp. 175-176, Prentice-Hall, inc., Englewood Cliffs, NJ, 1987.

Johns, H.E., Cunningham, J.R.: The Physics of Radiology, 4th Edition. pp.391-395, Charles C. Thomas, Publisher, Springfield, IL, 1983.

Keane, T.J., Van Dyk, J.: Treatment Planning for Lung Cancer. *Cancer Treat. Symp.* 2:11-17, 1985.

Kuchnir, F.T., Van Huis, J.M., Pelizzari, C.A. : Effect of Lung-Density Correction Trearment Planning for Tangential Fields Breast Irradiation: A Case Report. *Med Dos.* 14:109-111,1989.

Laughlin, J.S., Mohan, R., Kutcher, G.J.: Choice of Optimum Megavoltage for Accelerators for Photon Beam Treatment. *Int. J Radiation Oncol. Biol. Phys.* 12: 1551-1557, 1980.

Leung, P.M.K., Seaman, B., Robinson, P.: Low Density Inhomogeneity Correction for 22 MV X-ray Therapy. *Radiology* 94:449-451, 1970.

Mackie, T.R., El-Khatib, E., Battista, J., Scrimger, J., Van Dyk, J., Cunningham, J.R.: Lung Dose Corrections for 6- and 15-MV X-Rays. *Med. Phys.* 12:327-332, 1985.

Mustafa, A.A., Jackson, D.F.: The Relation Between X-ray CT Number and Charged Particle Stopping Powers and its Significance for Radiotherapy Treatment Planning. *Phys. Med. Biol.* 28:169-176, 1983.

Orton, C.G., Mondalek, P.M., Spicka, J.T., Herron, D.S., Andres, L.I.: Lung Corrections in Photon Beam Treatment Planning: Are We Ready? *Int. J Rad. Onco. Biol. Phys.*, 10:191-2199, 1984.

Parkin, D.M., Laara, A., Muir, C.S.: Estimates of the Worldwide Frequency of Sixteen Major Cancers in 1980. *Int. J. Cancer* 41:184-197, 1988.

Perez, C.A., Brady, L.W.: Principles and Practice of Radiation Oncology, pp. 135-136, 1987.

Phelps, M.E., Gado, M.H., Hoffman, E.J.: Correlation of Effective Atomic Number and Electron Density With Attenuation Coefficients Measured With Polychromatic X-rays. *Radiology* 17:585-588, 1975.

Phillips, T.L., Bushke, F.: Radiation Tolerence of the Thoracic Spinal Cord. *Am. J. Roentgenol., Rad. Therapy & Nuclear Med.* **105**:659-664, 1969.

Prasad, S.C., Glasgow, G.P., Purdy, J.A.: Dosimetric Evaluation of a Computed Tomography Treatment System. *Radiology* **130**:777-781, 1979.

Rice, R.K., Mijnheer, B.J., Chin, L.M.: Benchmark Measurements for Lung Dose Corrections for X-ray Beams. *Int. J Radiat. Oncol. Biol. Phys.* **15**:399-409, 1988.

Robinson, P.J., Kreel, L.: Pulmonary Tissue Attenuation With Computer Tomography. *J. Comput. Asst. Tomog.* **3**:263-273, 1979.

Rosenblum, L.J., Mauceri, R.A., Wellenstein, D.E., Bassano, D.A., Cohen, W. N., Heitzman, E.R.: Computed Tomography of The Lung. *Radiology* **129**:521-524, 1978.

Siverberg, E., Boring, C.C., Squires, T.S.: Cancer Statistics 1990. *Ca-A Cancer Journal for Clinicians* **40**:9-26, 1990.

Sontag, M.R., Battista, J.J., Bronskill, M.J., Cunningham, J.R.: Implications of Computed Tomography for Inhomogeneity Correction in Photon Beam Dose Calculations. *Radiology* **124**:143-149, 1977.

Sontag, M.R., Cunningham, J.R.: Corrections to Absorbed Dose Calculations for Tissue Inhomogeneities. *Med. Phys.* **4**:431-436, 1977.

Sontag, M.R., Cunningham, J.R.: The Equivalent Tissue Air Ratio Method for Making Absorbed Dose Calculations in a Heterogeneous Medium. *Radiology* **129**: 787-794, 1978.

Tang, W. L., Khan, F. M., Gebri, B. J.: Validity of Lung Correction Algorithms. *Med. Phys.* **13**:683-686, 1986.

Task Group 21, Radiation Therapy Committee, American Association of Physicists in Medicine: A Protocol for the Determination of Absorbed Dose from High-Energy Photon and Electron Beam. *Med. Phys.* **10**:741-771, 1983.

Ten Haken, R.K., Kessler, M.L., Stern, R.L., Ellis, J.H., Niklason, L.T.: Quality of Assurance of CT and MRI for Radiation Therapy Treatment Planning. "Quality Assurance in Radiotherapy Physics", proceedings of an American College of Medical Physics Symposium, edited by G. Starkschall & J. Horton, 1991. Medical Physics Publishing, Madison, Wisconsin, 1991.

Thacer, M., Palti, S.: Evaluation of Density Correction Algorithms for Photon-Beam Dose Calculation. *Radiology* **141**:201-205, 1981.

Thomas, S.J.: A Modified Power-Law Formula for Inhomogeneity Corrections in Beams of High-Energy X-rays. *Med. Phys.* **18**:719-723, 1991.

Van Dyk, J., Keane, T.J., Kan, S., Rider, W.D., Fryer, C.J.H.: Radiation Pneumonities Following Large Single Dose Irradiation: A Revaluation Based on Absolute Dose to Lung. *Int. J Radiat. Oncol. Biol. Phys.* **7**:461-467, 1981.

Van Dyk, J., Keane, T.J., Rider, W.D.: Lung Density as Measured by Computerized Tomography: Implication for Radiotherapy. *Int. J. Radiation Oncol. Biol. Phys.* **8**:1363-1372, 1982.

Van de Geijn, J.: The Extended Net Fractional Depth Dose: Correction for Inhomogeneities, Including Effects of Electron Transport in Photon Beam Dose Calculation. *Med. Phys.* **14**:84-92, 1987.

Wong, J.W., Henkelman, R.M.: Reconsideration of the Power-Law (Batho) Equation for Inhomogeneity Correction. *Med. Phys.* **9**:521-530, 1982.

Young, M.E.J., Kornelsen, R.O.: Dose Corrections for Low-Density Tissue Inhomogeneities and Air Channels for 10 MV X-ray. *Med. Phys.* **10**:450-455, 1983.

APPENDIX A

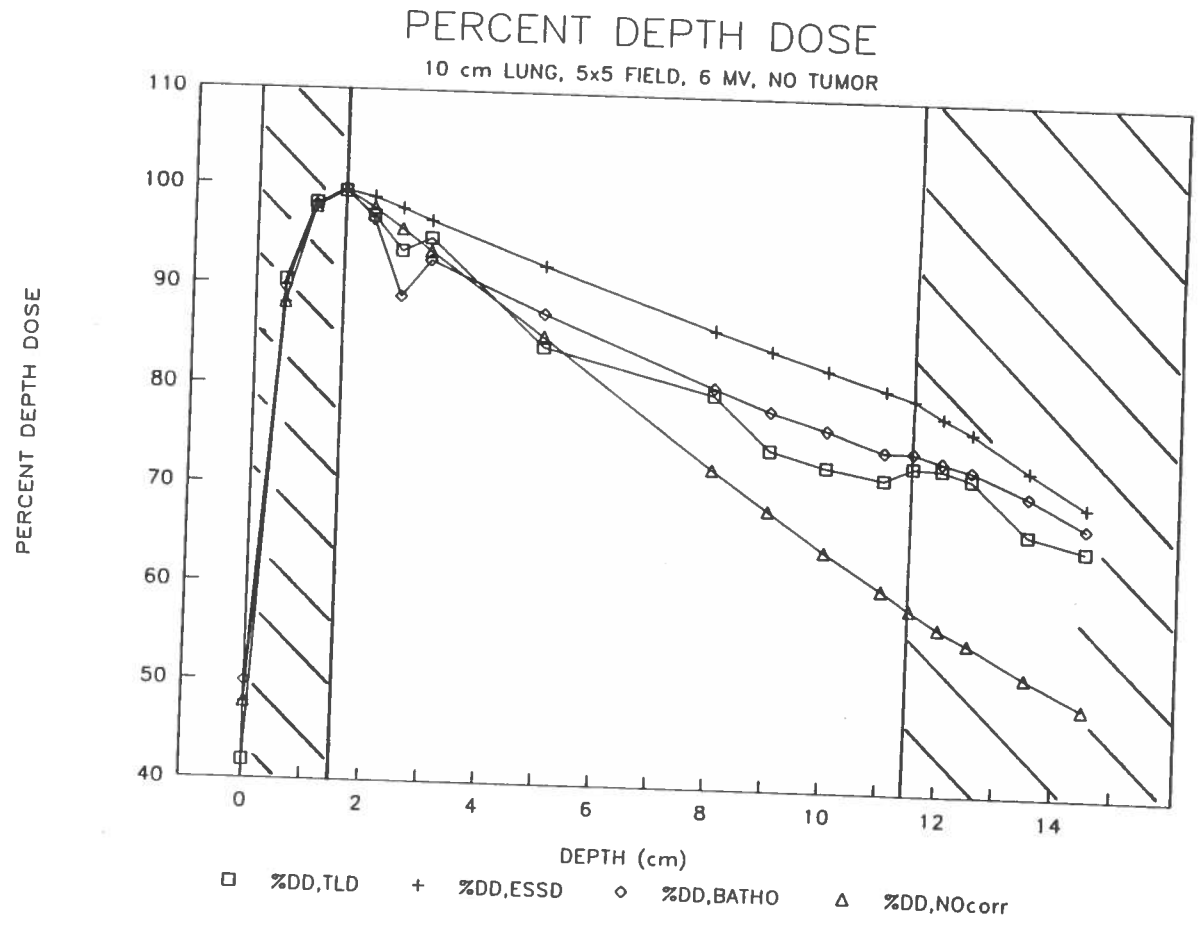

FIGURE A-1. **Measured and calculated central axis percent depth dose for a 6 MV x-ray from a Clinac 600C for a 10 cm thick non-tumor lung phantom composed of cork with 1.5 cm overlay of build-up. The field size is 5 x 5 cm.**

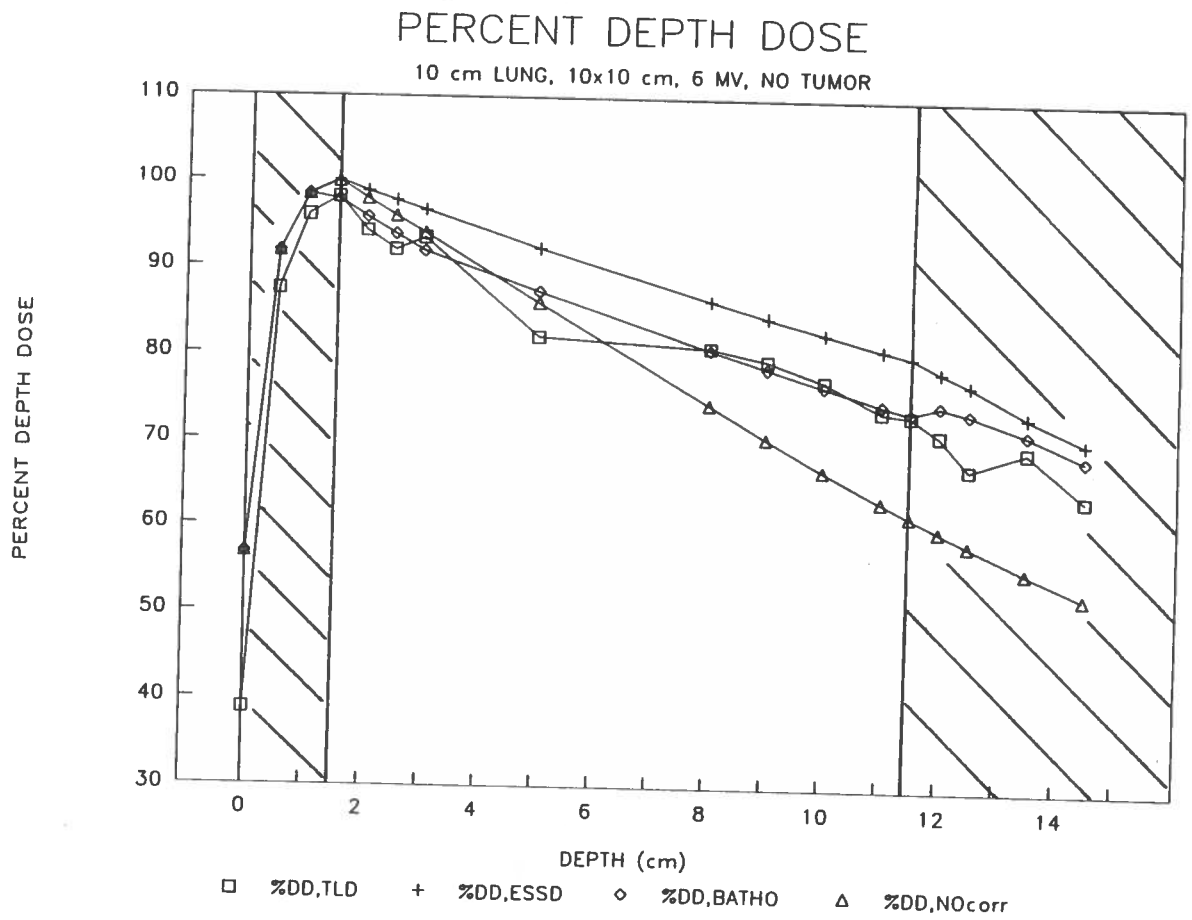

FIGURE A-2. **Measured and calculated central axis percent depth dose for a 6 MV x-ray from a Clinac 600C for a 10 cm thick non-tumor lung phantom composed of cork with 1.5 cm overlay of build-up. The field size is 10 x 10 cm.**

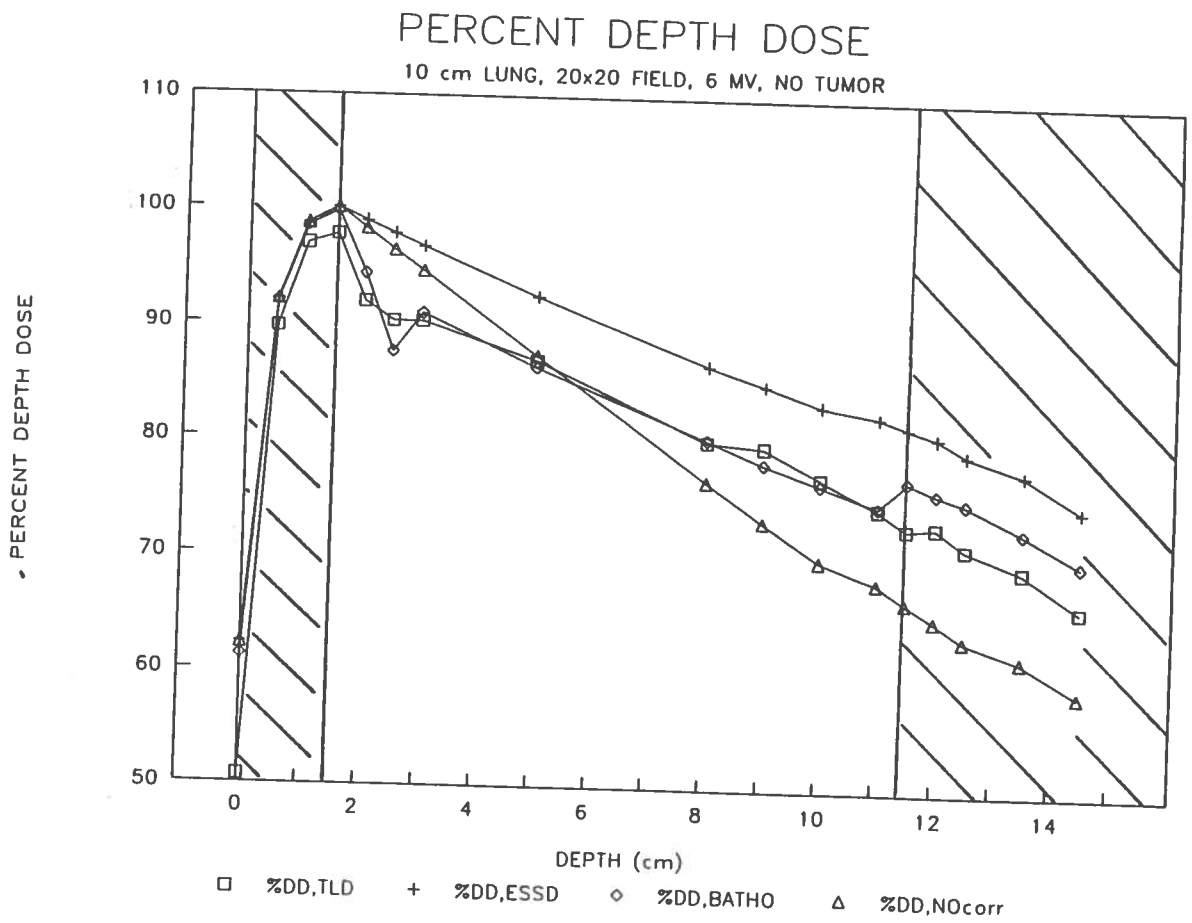

FIGURE A-3. **Measured and calculated central axis percent depth dose for a 6 MV x-ray from a Clinac 600C for a 10 cm thick non-tumor lung phantom composed of cork with 1.5 cm overlay of build-up. The field size is 20 x 20 cm.**

FIGURE A-4. **Measured and calculated central axis percent depth dose for a 6 MV x-ray from a Clinac 600C for a 10 cm thick tumor lung phantom composed of cork with 1.5 cm overlay of build-up. The field size is 5 x 5 cm.**

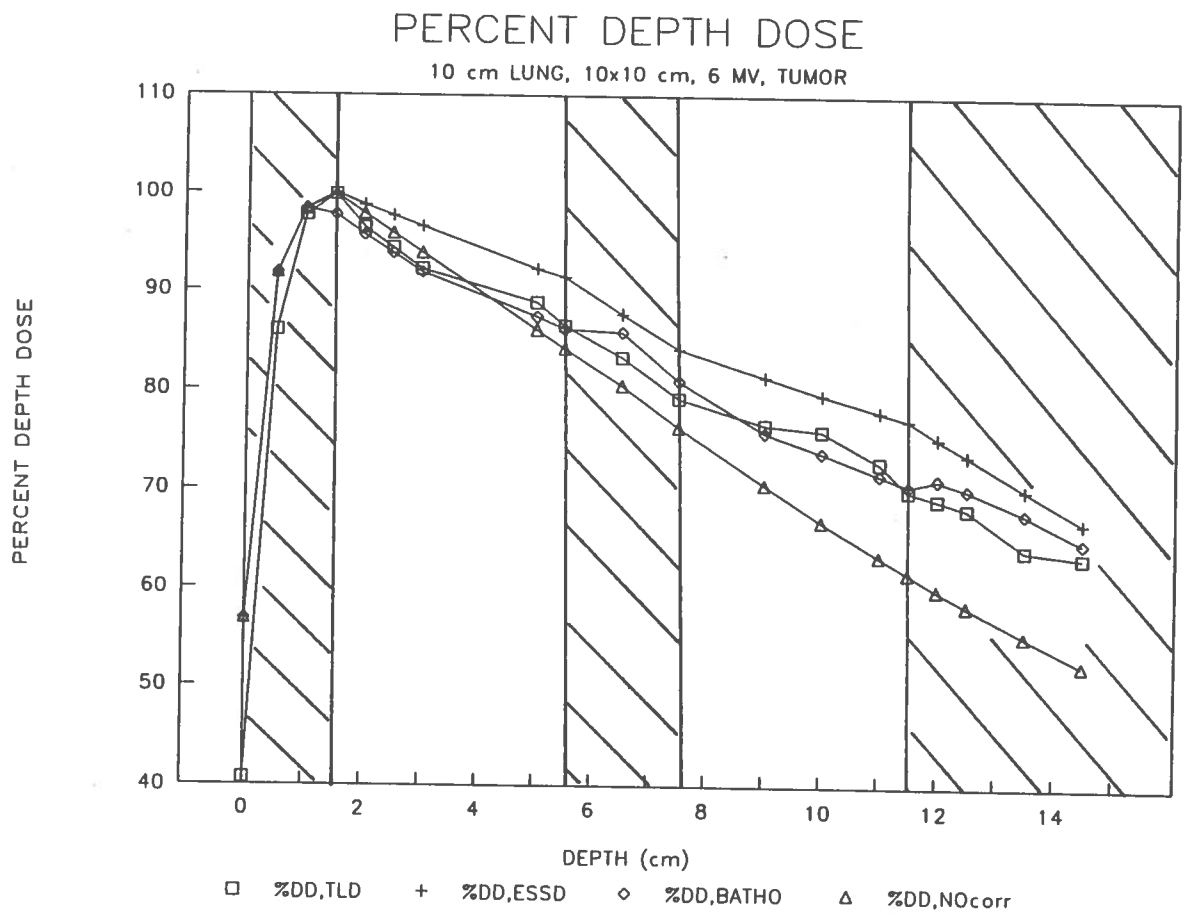

FIGURE A-5. **Measured and calculated central axis percent depth dose for a 6 MV x-ray from a Clinac 600C for a 10 cm thick tumor lung phantom composed of cork with 1.5 cm overlay of build-up. The field size is 10 x 10 cm.**

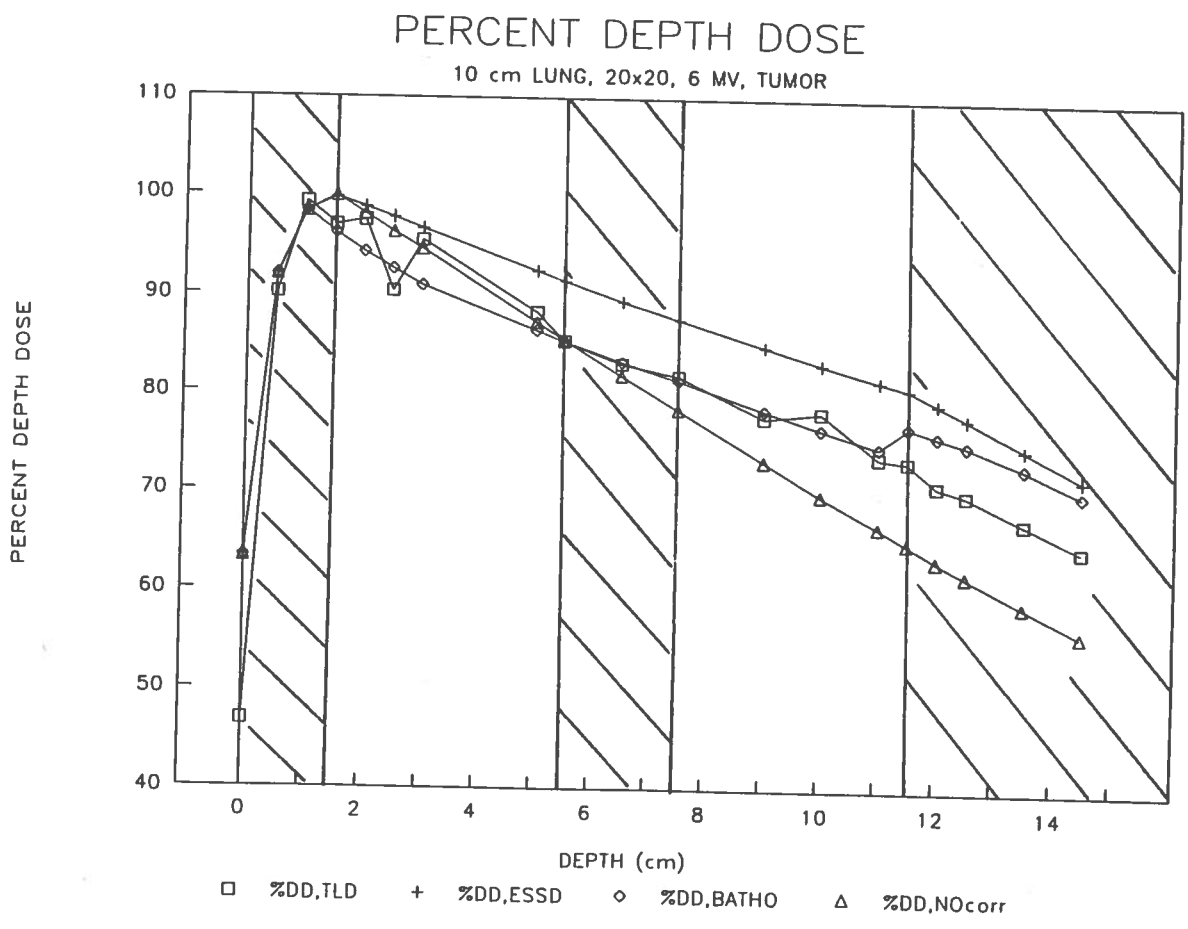

FIGURE A-6. **Measured and calculated central axis percent depth dose for a 6 MV x-ray from a Clinac 600C for a 10 cm thick tumor lung phantom composed of cork with 1.5 cm overlay of build-up. The field size is 20 x 20 cm.**

FIGURE A-7. **Measured and calculated central axis percent depth dose for a 6 MV x-ray from a Clinac 600C for a 20 cm thick non-tumor lung phantom composed of cork with 1.5 cm overlay of build-up. The field size is 5 x 5 cm.**

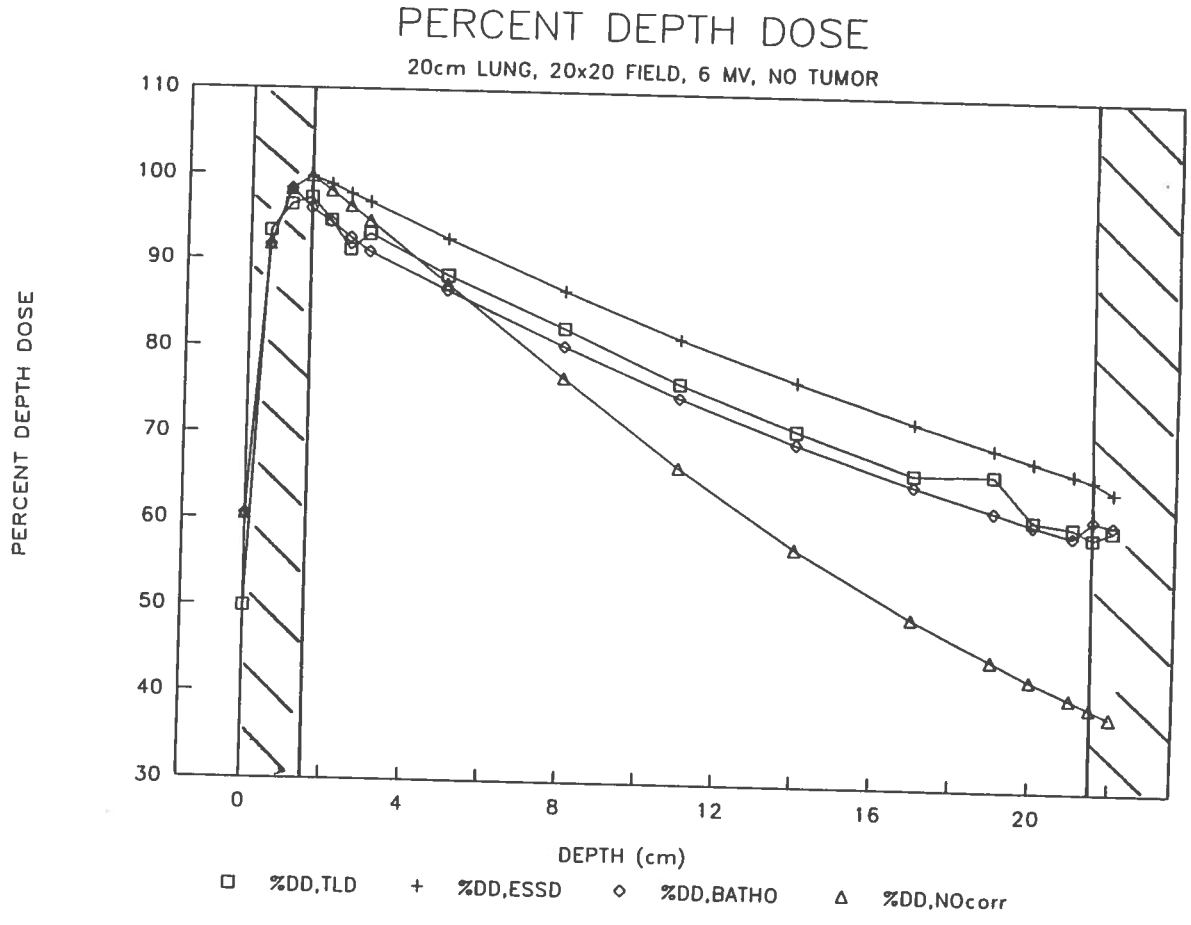

FIGURE A-8. **Measured and calculated central axis percent depth dose for a 6 MV x-ray from a Clinac 600C for a 20 cm thick non-tumor lung phantom composed of cork with 1.5 cm overlay of build-up. The field size is 20 x 20 cm.**

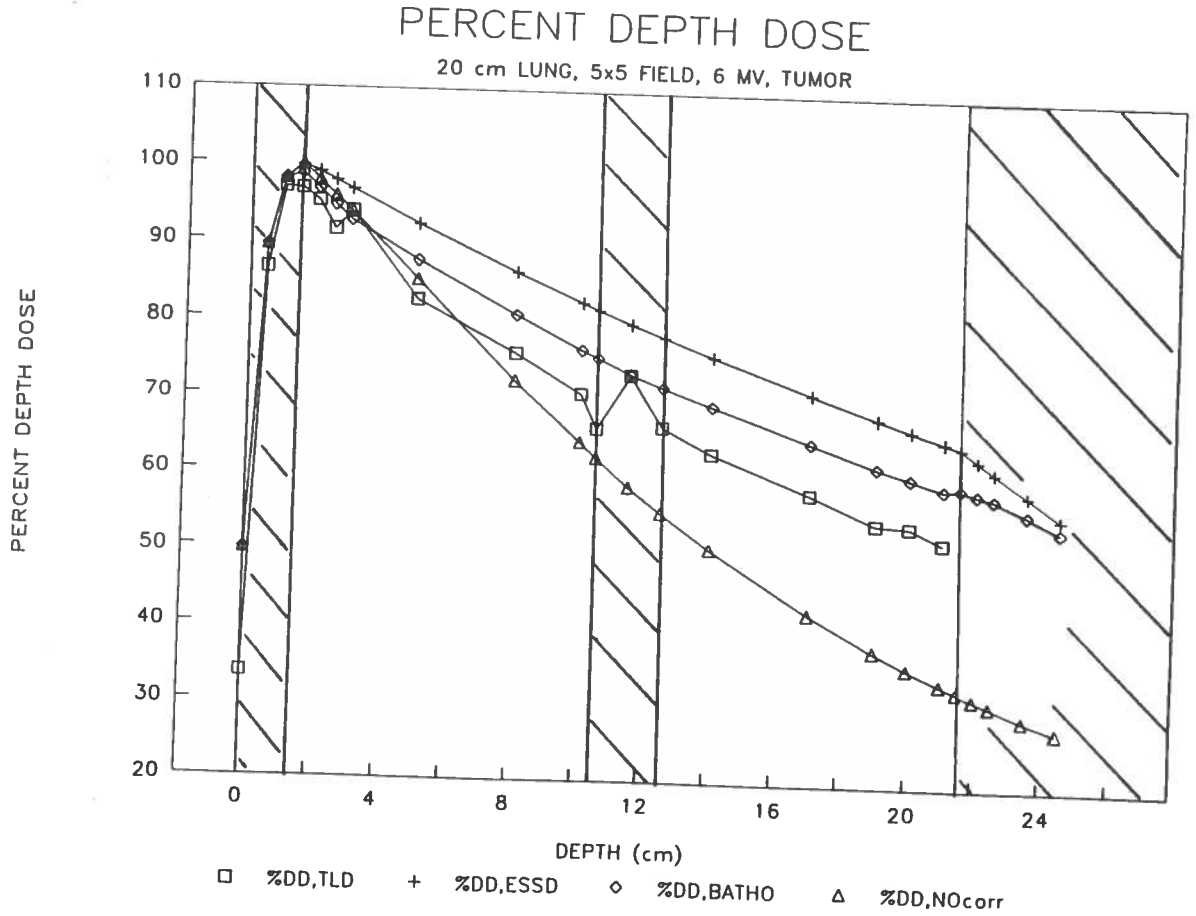

FIGURE A-9. **Measured and calculated central axis percent depth dose for a 6 MV x-ray from a Clinac 600C for a 20 cm thick tumor lung phantom composed of cork with 1.5 cm overlay of build-up. The field size is 5 x 5 cm.**

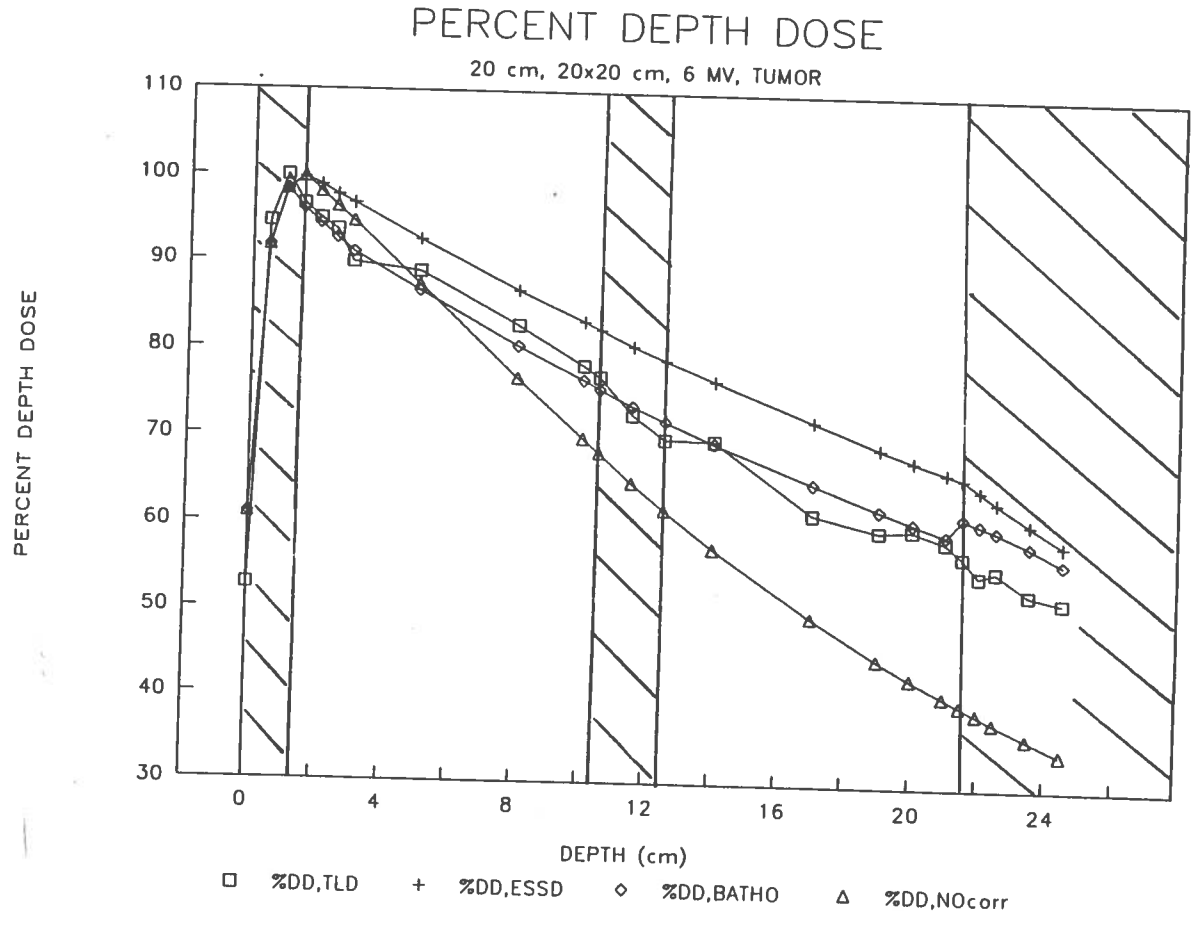

FIGURE A-10. **Measured and calculated central axis percent depth dose for a 6 MV x-ray from a Clinac 600C for a 20 cm thick tumor lung phantom composed of cork with 1.5 cm overlay of build-up. The field size is 20 x 20 cm.**

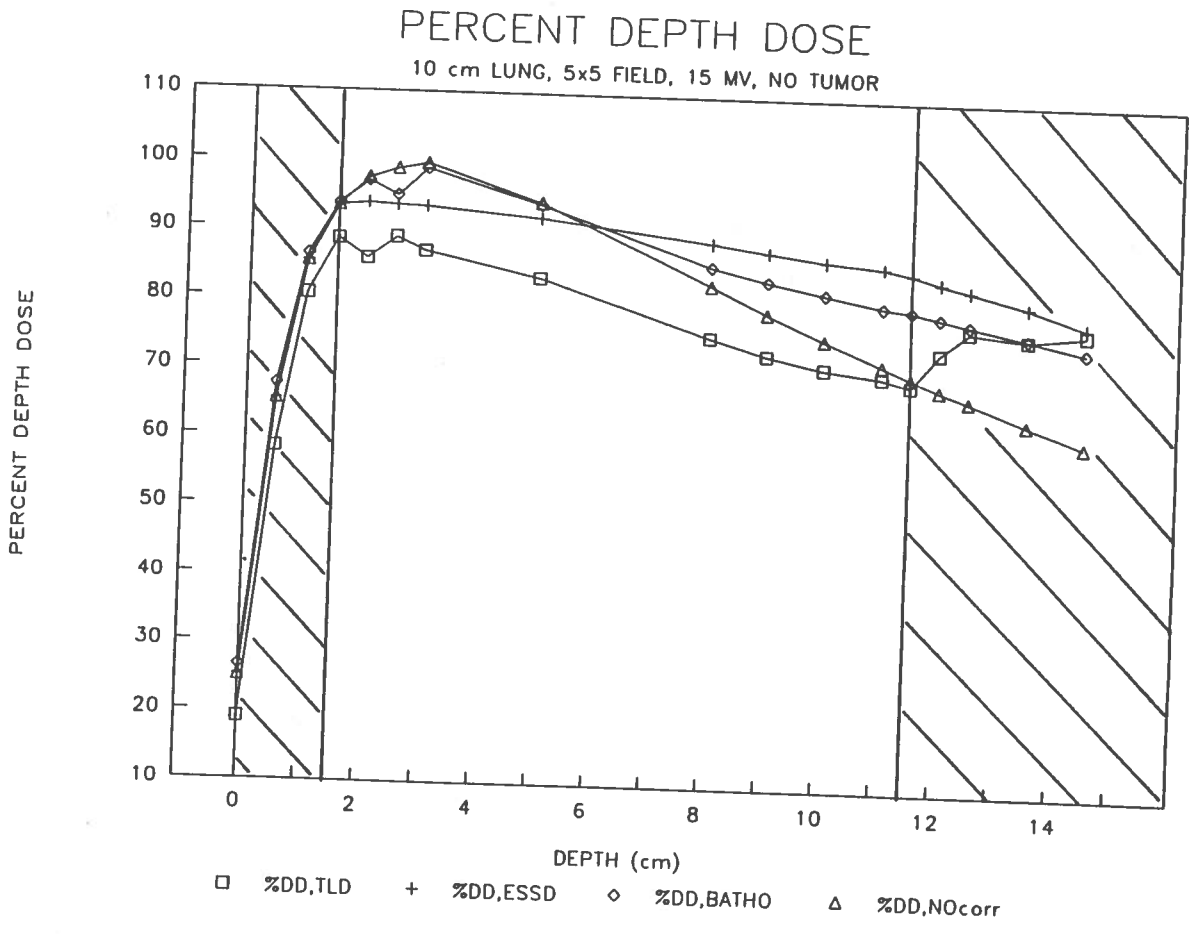

FIGURE A-11. **Measured and calculated central axis percent depth dose for a 15 MV x-ray from a Clinac 20 for a 10 cm thick non-tumor lung phantom composed of cork with 1.5 cm overlay of build-up. The field size is 5 x 5 cm.**

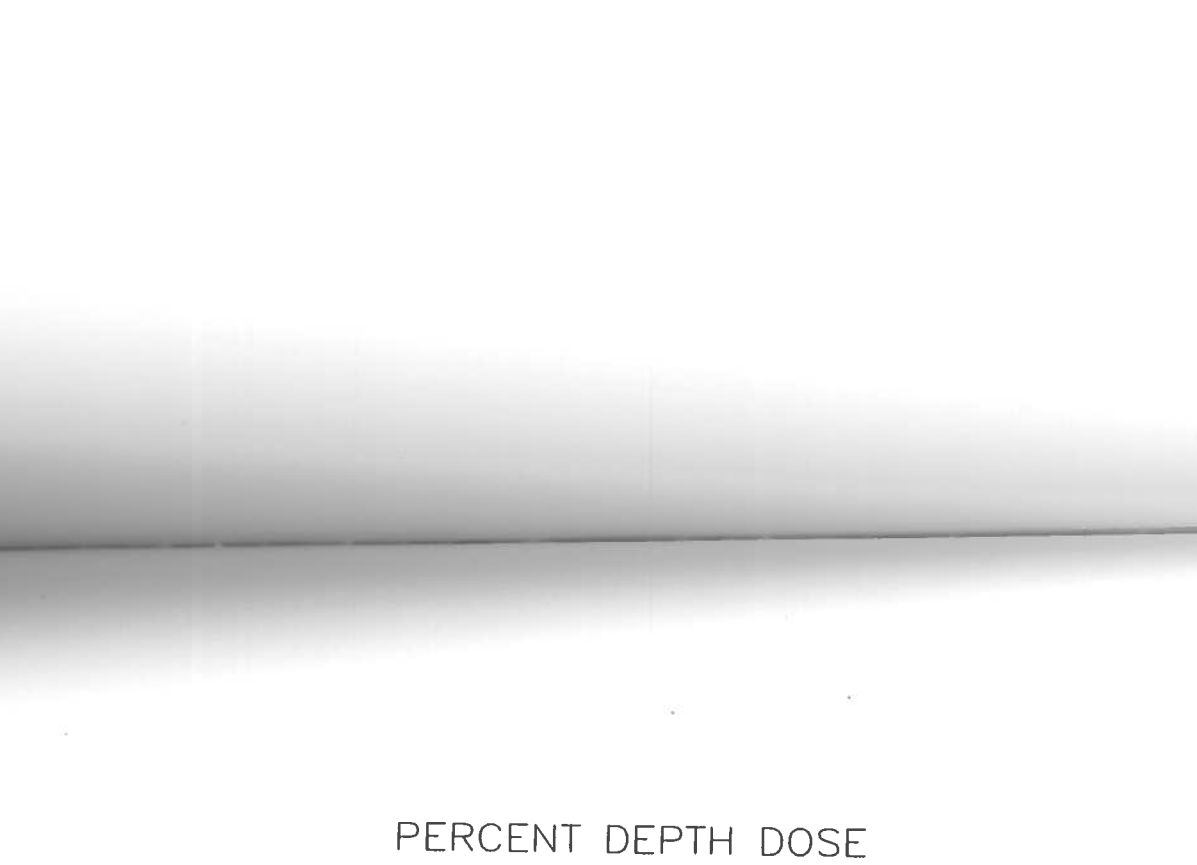

FIGURE A-12. **Measured and calculated central axis percent depth dose for a 15 MV x-ray from a Clinac 20 for a 10 cm thick non-tumor lung phantom composed of cork with 1.5 cm overlay of build-up. The field size is 20 x 20 cm.**

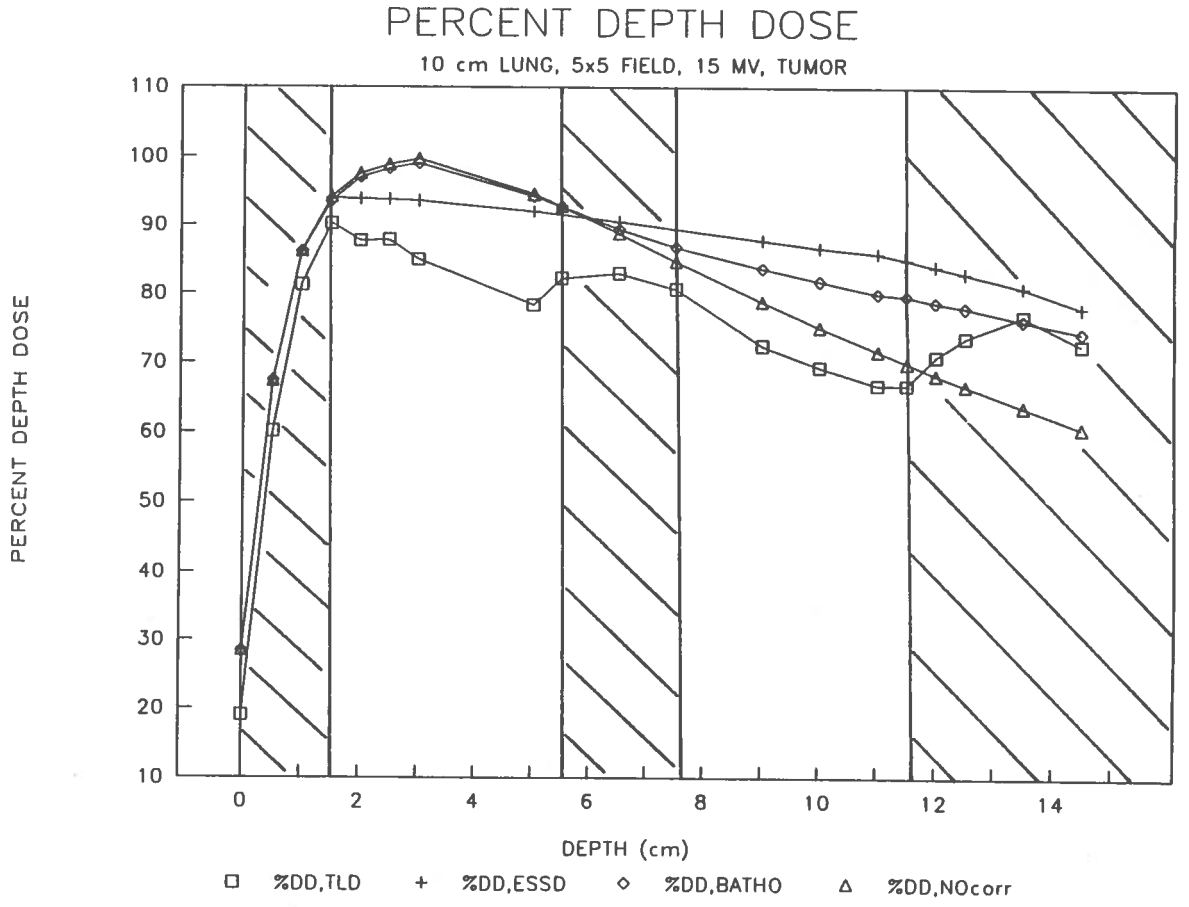

FIGURE A-13. **Measured and calculated central axis percent depth dose for a 15 MV x-ray from a Clinac 20 for a 10 cm thick tumor lung phantom composed of cork with 1.5 cm overlay of build-up. The field size is 5 x 5 cm.**

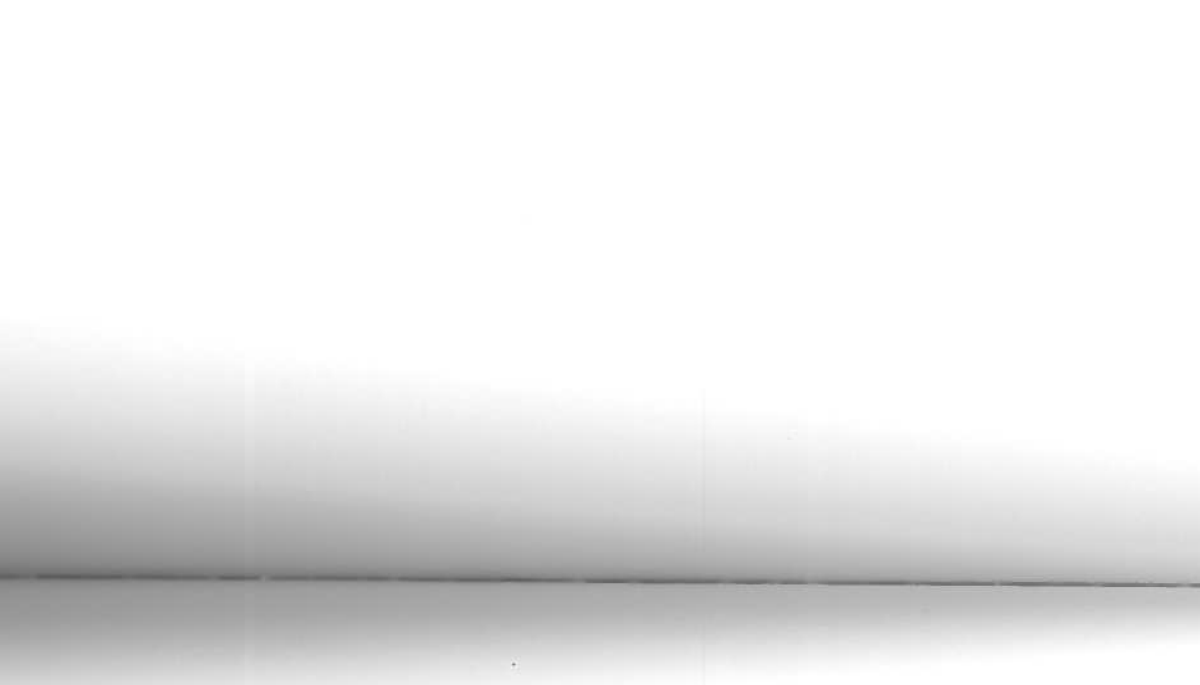

FIGURE A-14. **Measured and calculated central axis percent depth dose for a 15 MV x-ray from a Clinac 20 for a 10 cm thick tumor lung phantom composed of cork with 1.5 cm overlay of build-up. The field size is 20 x 20 cm.**

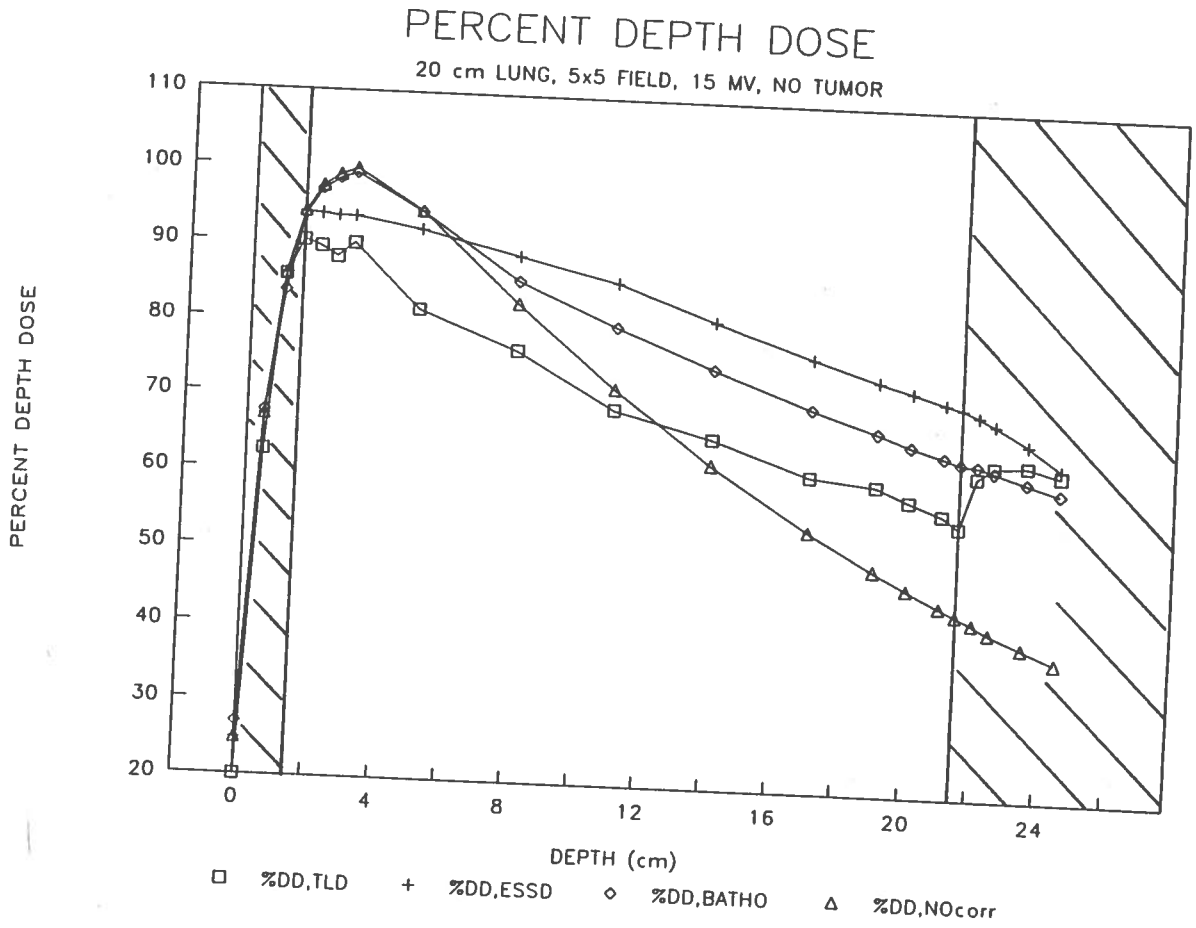

FIGURE A-15. **Measured and calculated central axis percent depth dose for a 15 MV x-ray from a Clinac 20 for a 20 cm thick non-tumor lung phantom composed of cork with 1.5 cm overlay of build-up. The field size is 5 x 5 cm.**

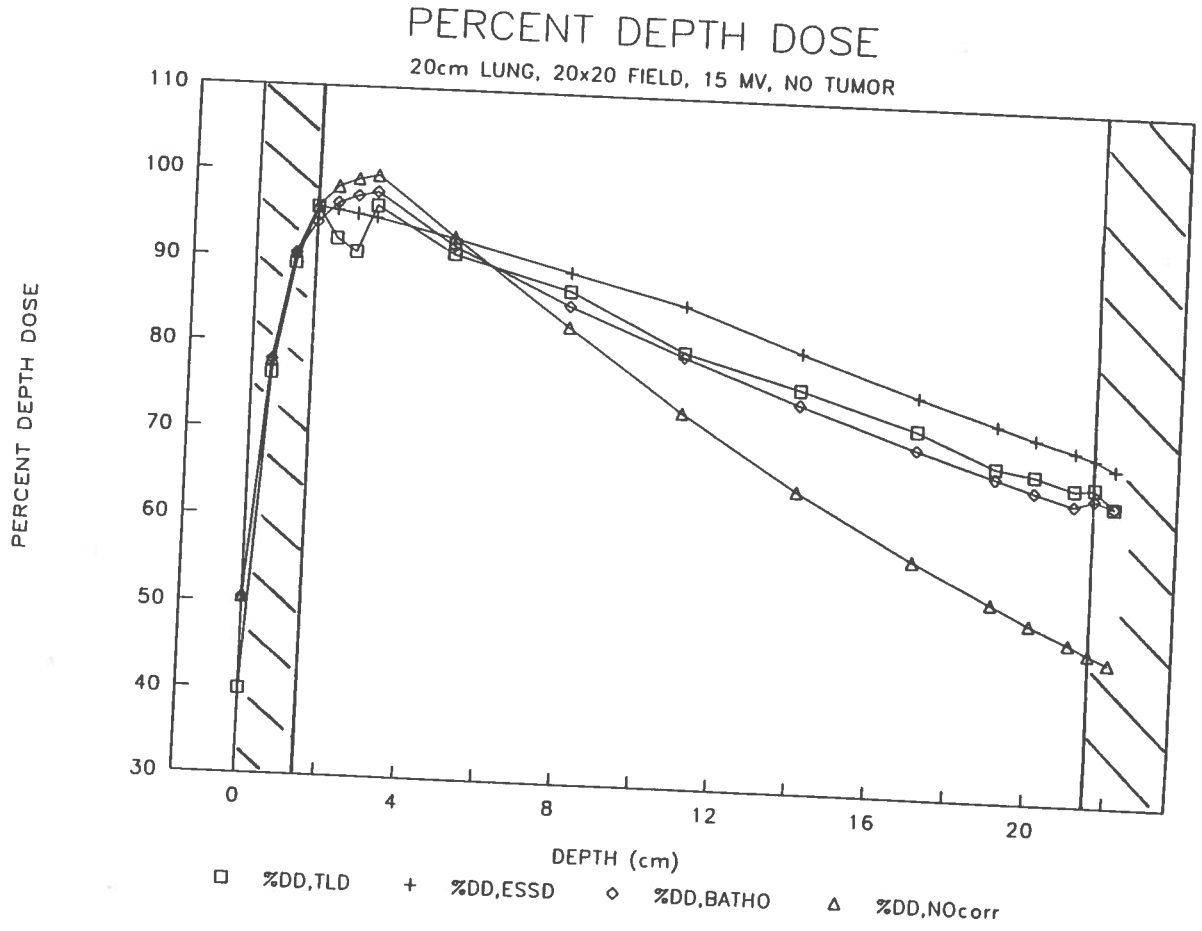

FIGURE A-16. **Measured and calculated central axis percent depth dose for a 15 MV x-ray from a Clinac 20 for a 20 cm thick non-tumor lung phantom composed of cork with 1.5 cm overlay of build-up. The field size is 20 x 20 cm.**

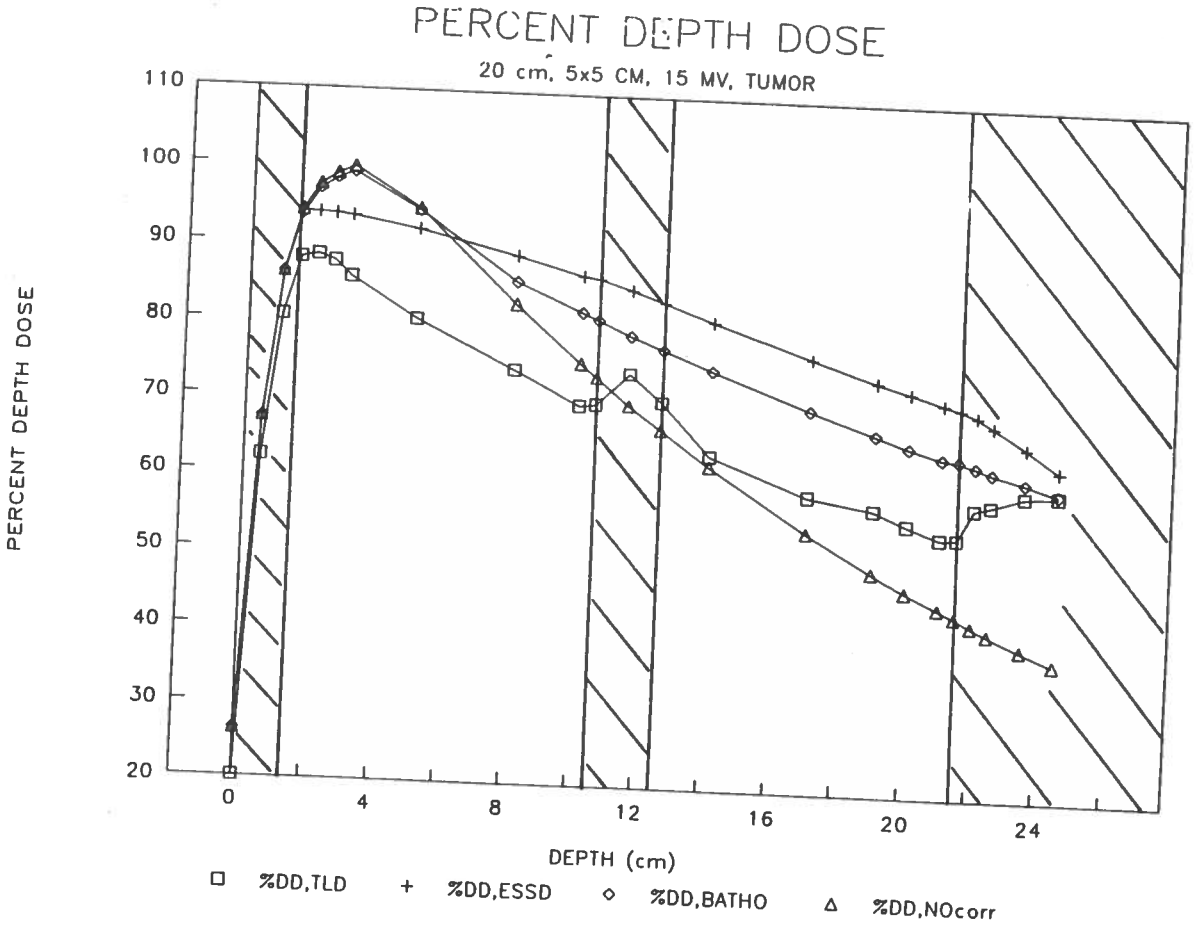

FIGURE A-17. **Measured and calculated central axis percent depth dose for a 15 MV x-ray from a Clinac 20 for a 20 cm thick tumor lung phantom composed of cork with 1.5 cm overlay of build-up. The field size is 5 x 5 cm.**

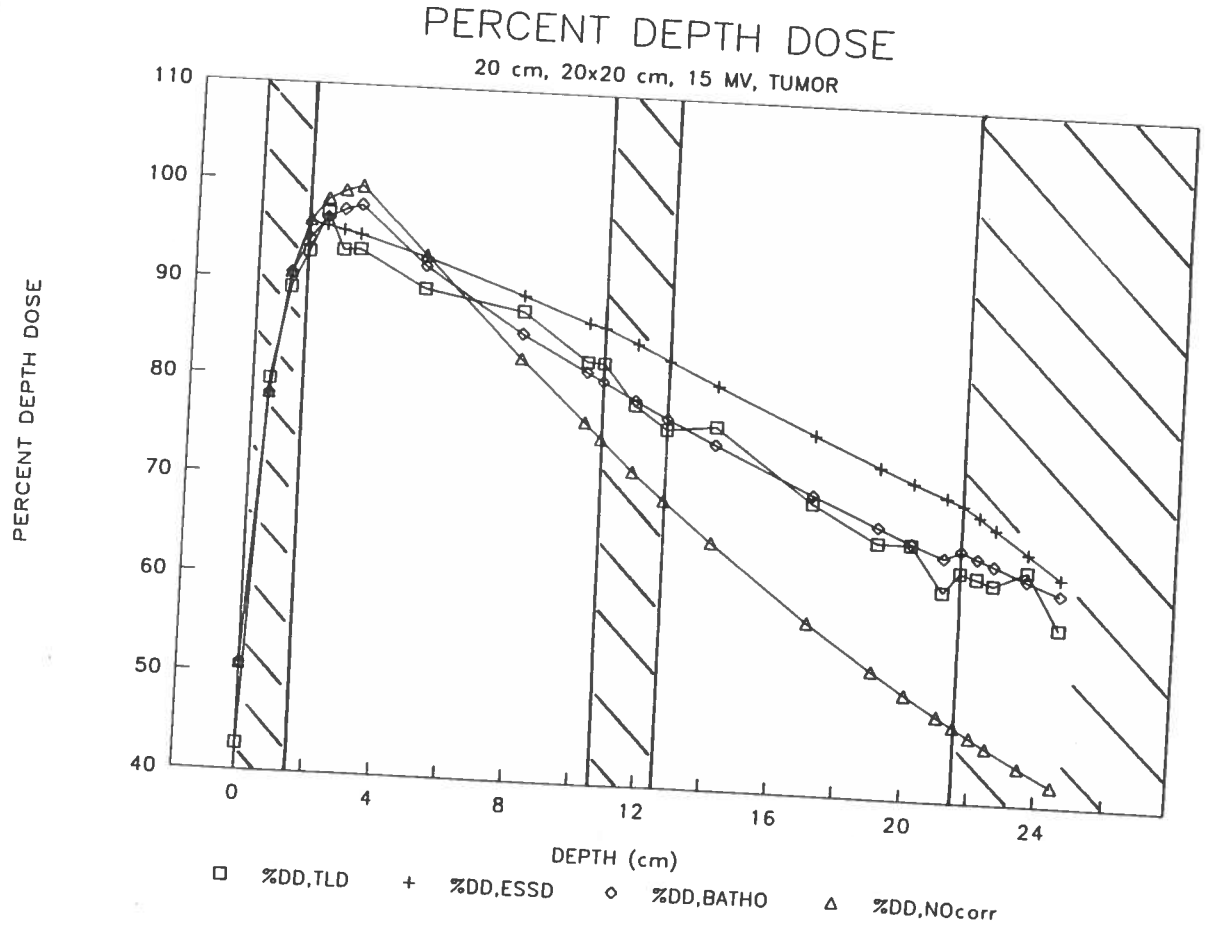

FIGURE A-18. **Measured and calculated central axis percent depth dose for a 15 MV x-ray from a Clinac 20 for a 20 cm thick tumor lung phantom composed of cork with 1.5 cm overlay of build-up. The field size is 20 x 20 cm.**

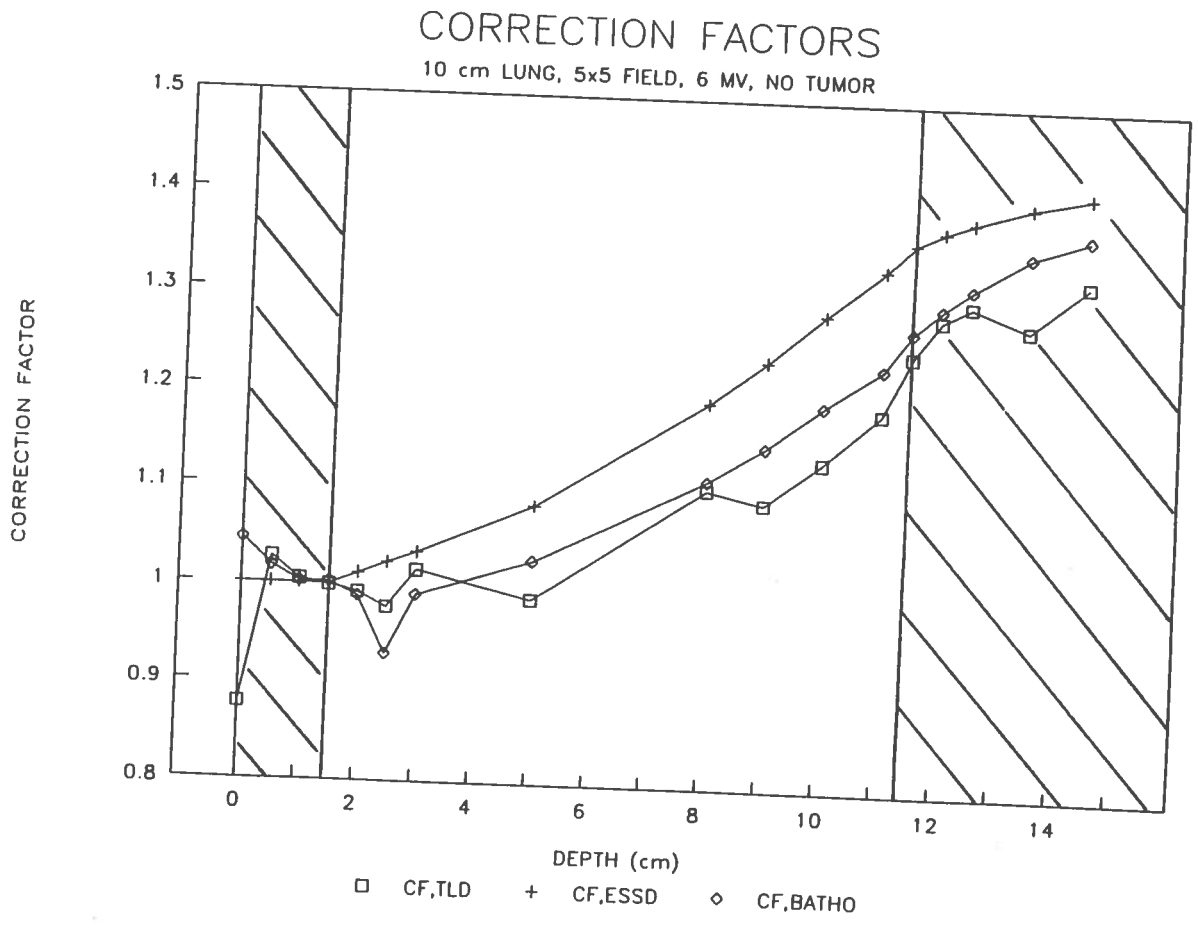

FIGURE A-19. **Measured and calculated correction factor for a 6 MV x-ray from a Clinac 600C for a 10 cm thick non-tumor lung phantom composed of cork with 1.5 cm overlay of build-up. The field size is 5 x 5 cm.**

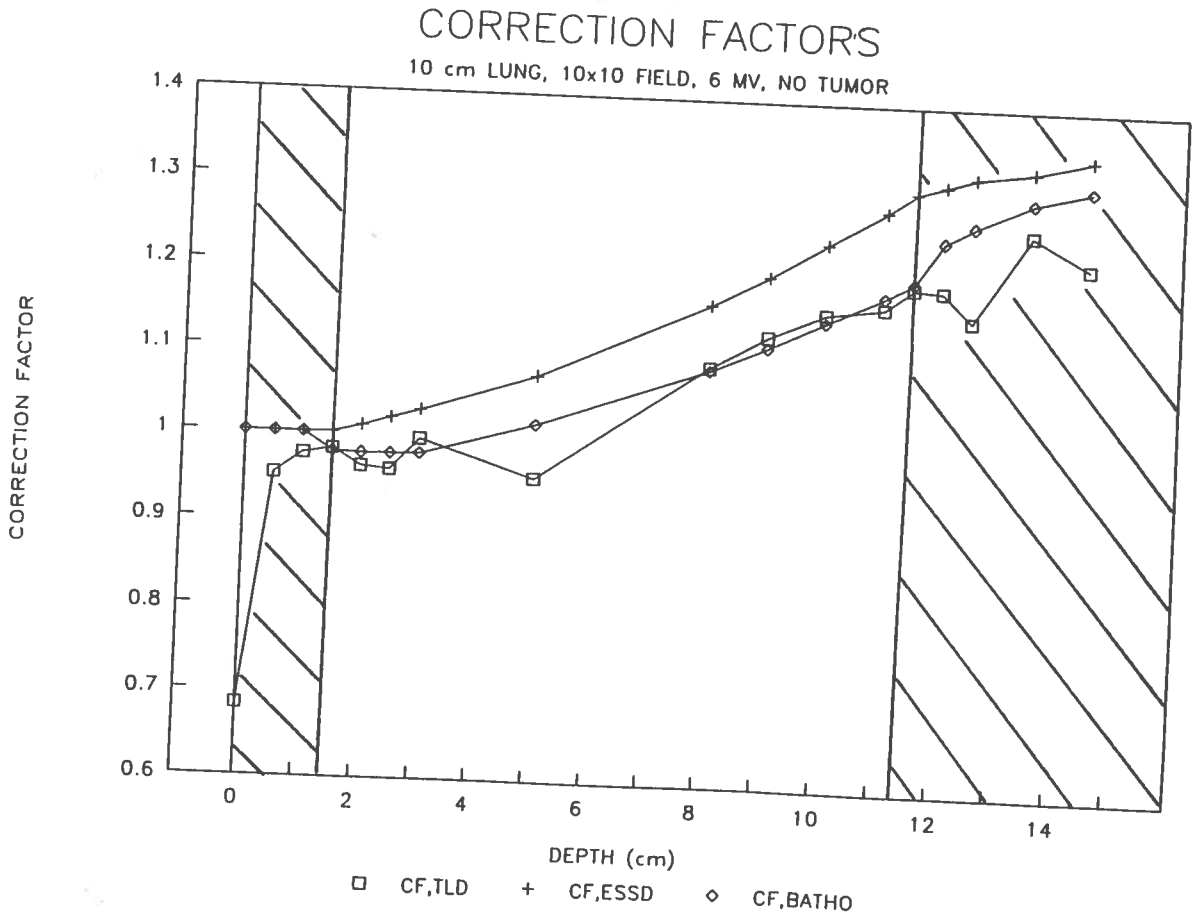

FIGURE A-20. Measured and calculated correction factor for a 6 MV x-ray from a Clinac 600C for a 10 cm thick non-tumor lung phantom composed of cork with 1.5 cm overlay of build-up. The field size is 10 x 10 cm.

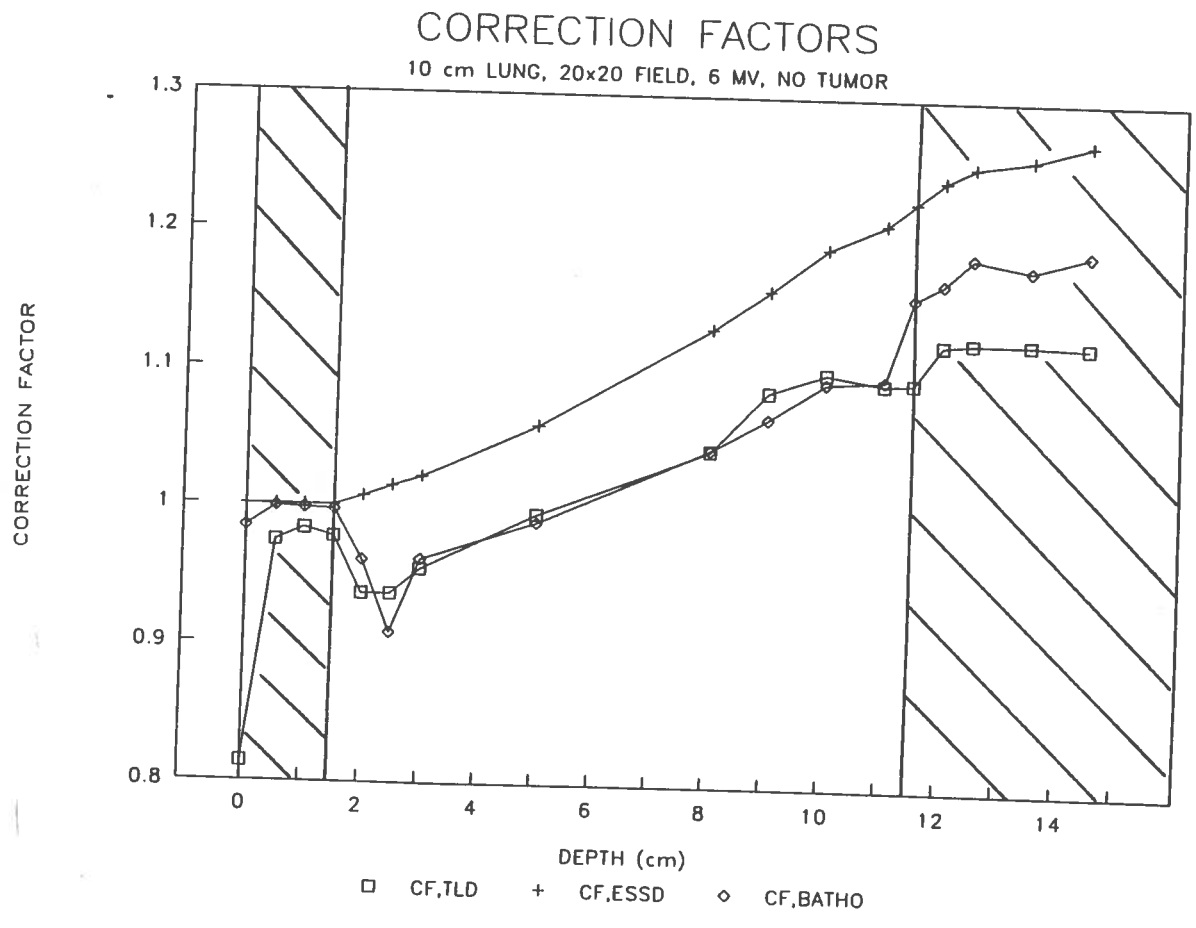

FIGURE A-21. Measured and calculated correction factor for a 6 MV x-ray from a Clinac 600C for a 10 cm thick non-tumor lung phantom composed of cork with 1.5 cm overlay of build-up. The field size is 20 x 20 cm.

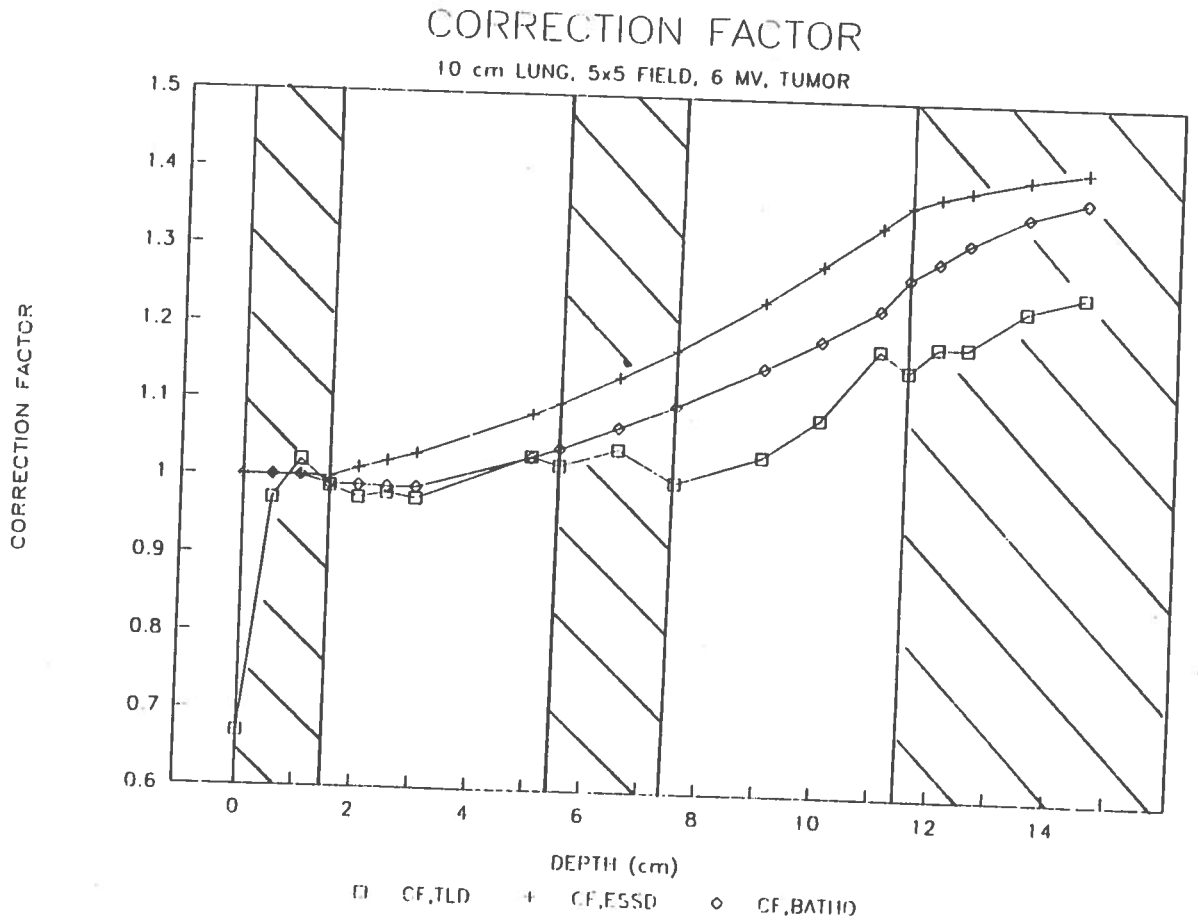

FIGURE A-22. Measured and calculated correction factor for a 6 MV x-ray from a Clinac 600C for a 10 cm thick tumor lung phantom composed of cork with 1.5 cm overlay of build-up. The field size is 5 x 5 cm.

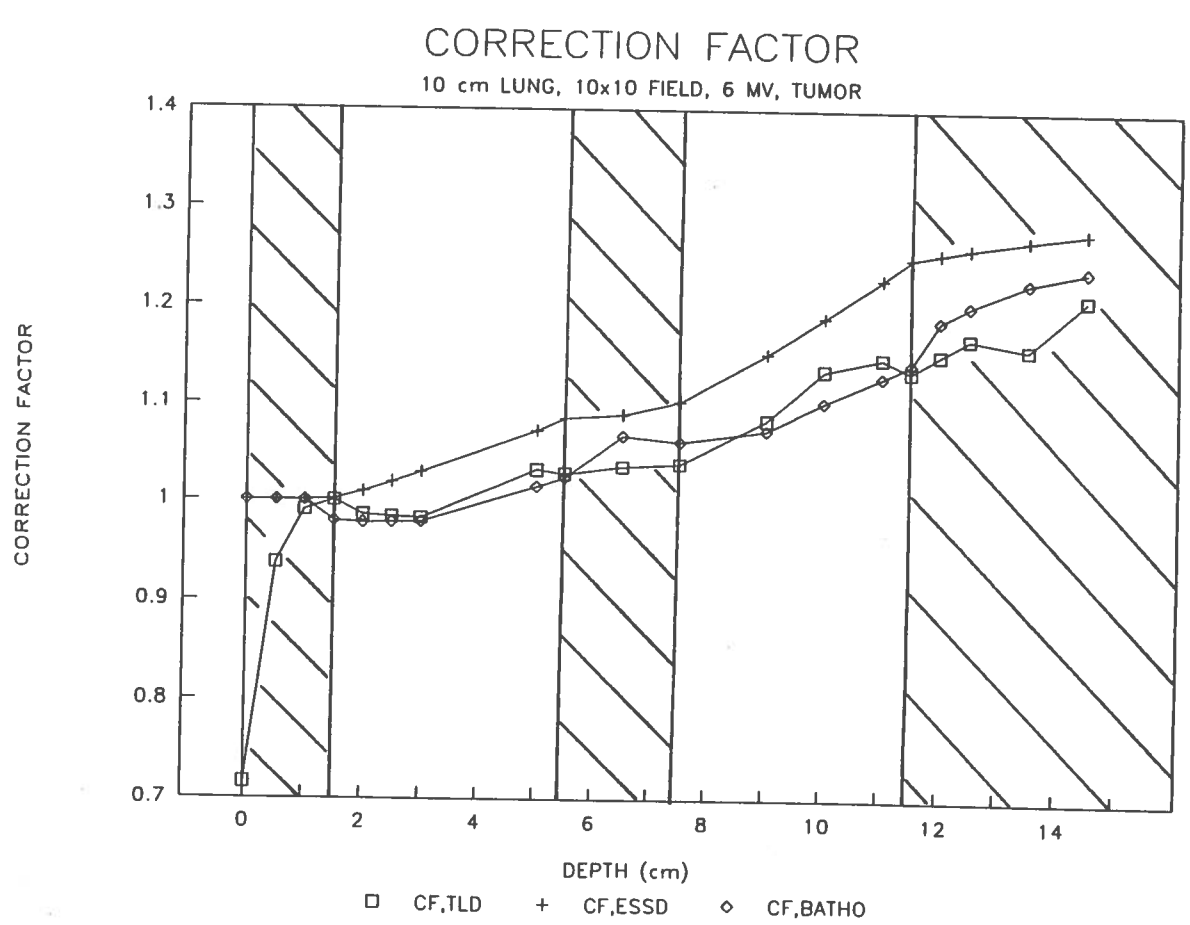

FIGURE A-23. **Measured and calculated correction factor for a 6 MV x-ray from a Clinac 600C for a 10 cm thick tumor lung phantom composed of cork with 1.5 cm overlay of build-up. The field size is 10 x 10 cm.**

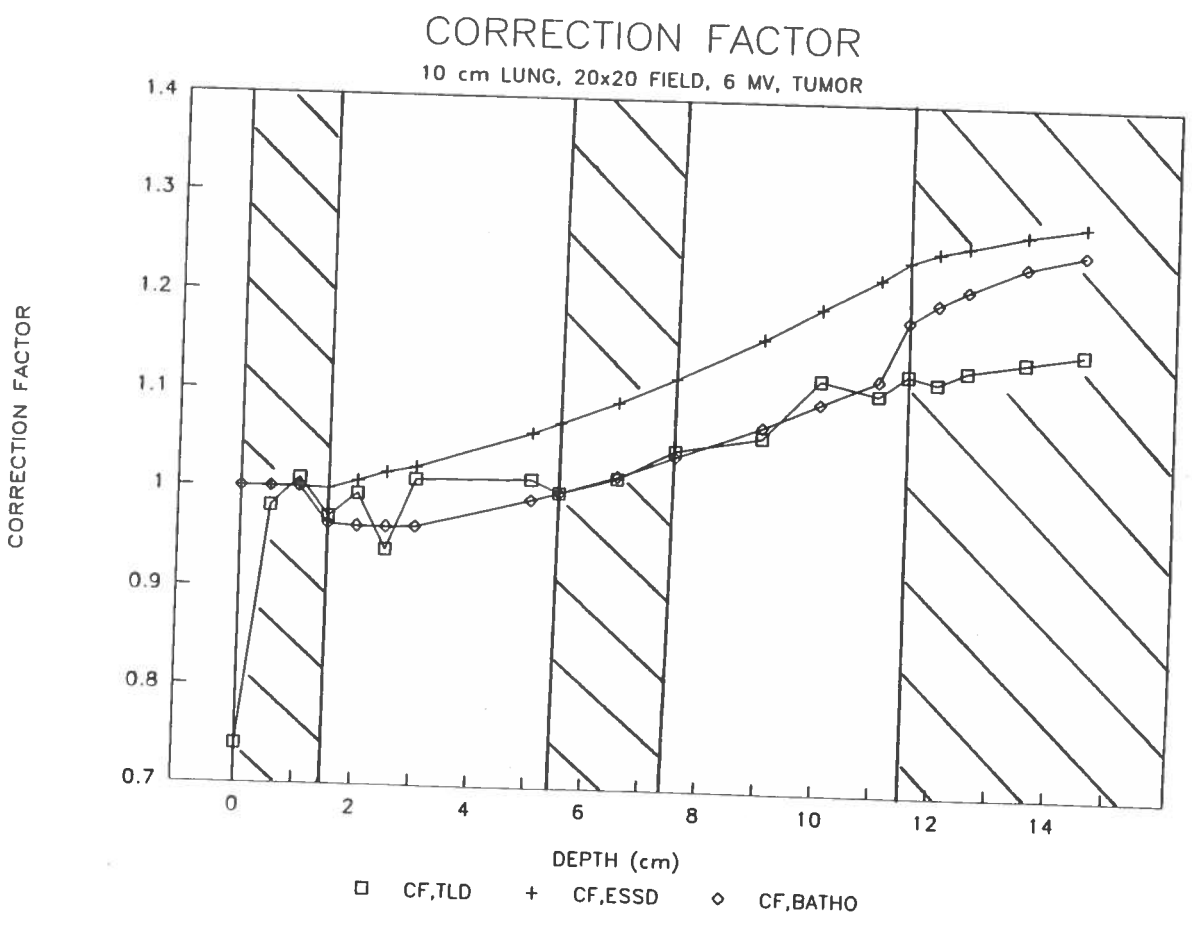

FIGURE A-24. **Measured and calculated correction factor for a 6 MV x-ray from a Clinac 600C for a 10 cm thick tumor lung phantom composed of cork with 1.5 cm overlay of build-up. The field size is 20 x 20 cm.**

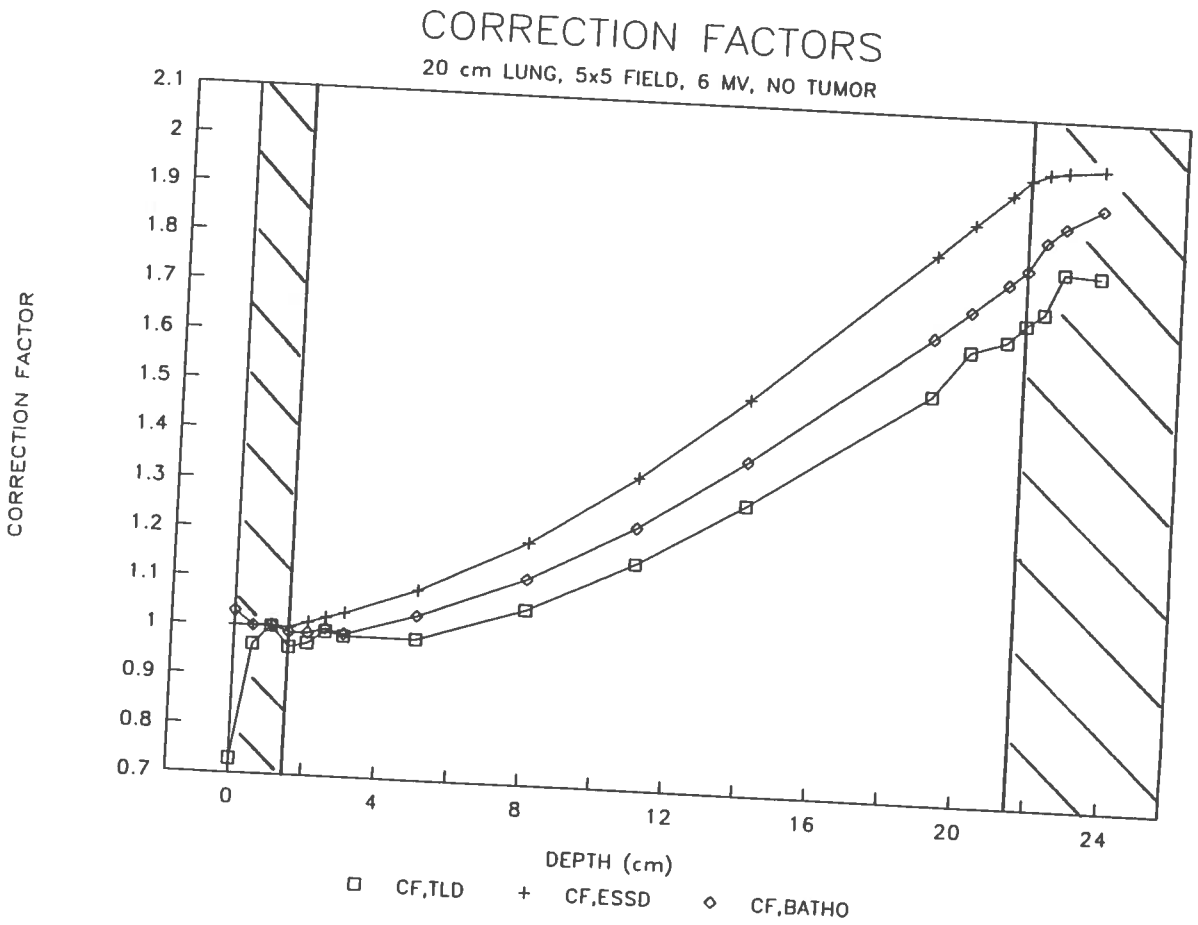

FIGURE A-25. Measured and calculated correction factor for a 6 MV x-ray from a Clinac 600C for a 20 cm thick non-tumor lung phantom composed of cork with 1.5 cm overlay of build-up. The field size is 5 x 5 cm.

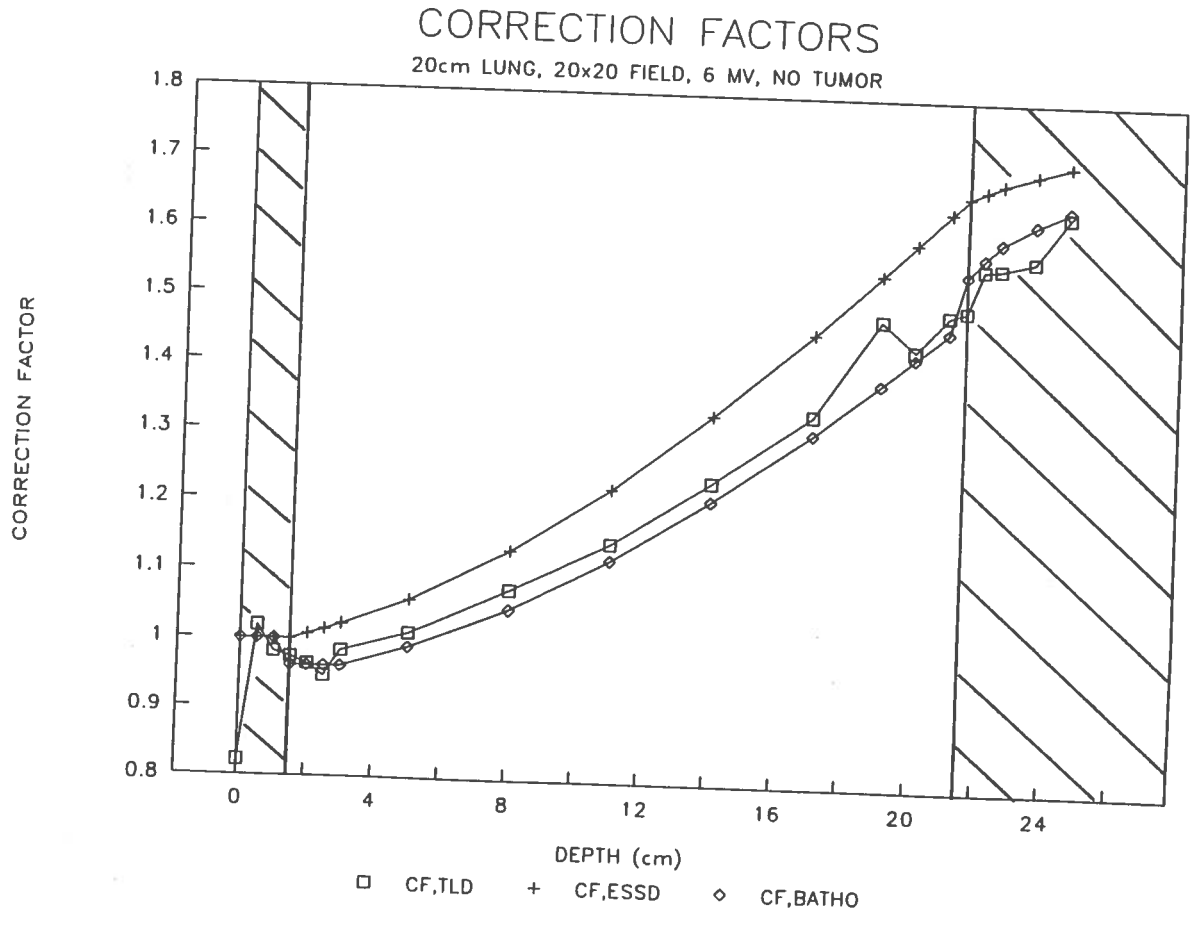

FIGURE A-26. **Measured and calculated correction factor for a 6 MV x-ray from a Clinac 600C for a 20 cm thick non-tumor lung phantom composed of cork with 1.5 cm overlay of build-up. The field size is 20 x 20 cm.**

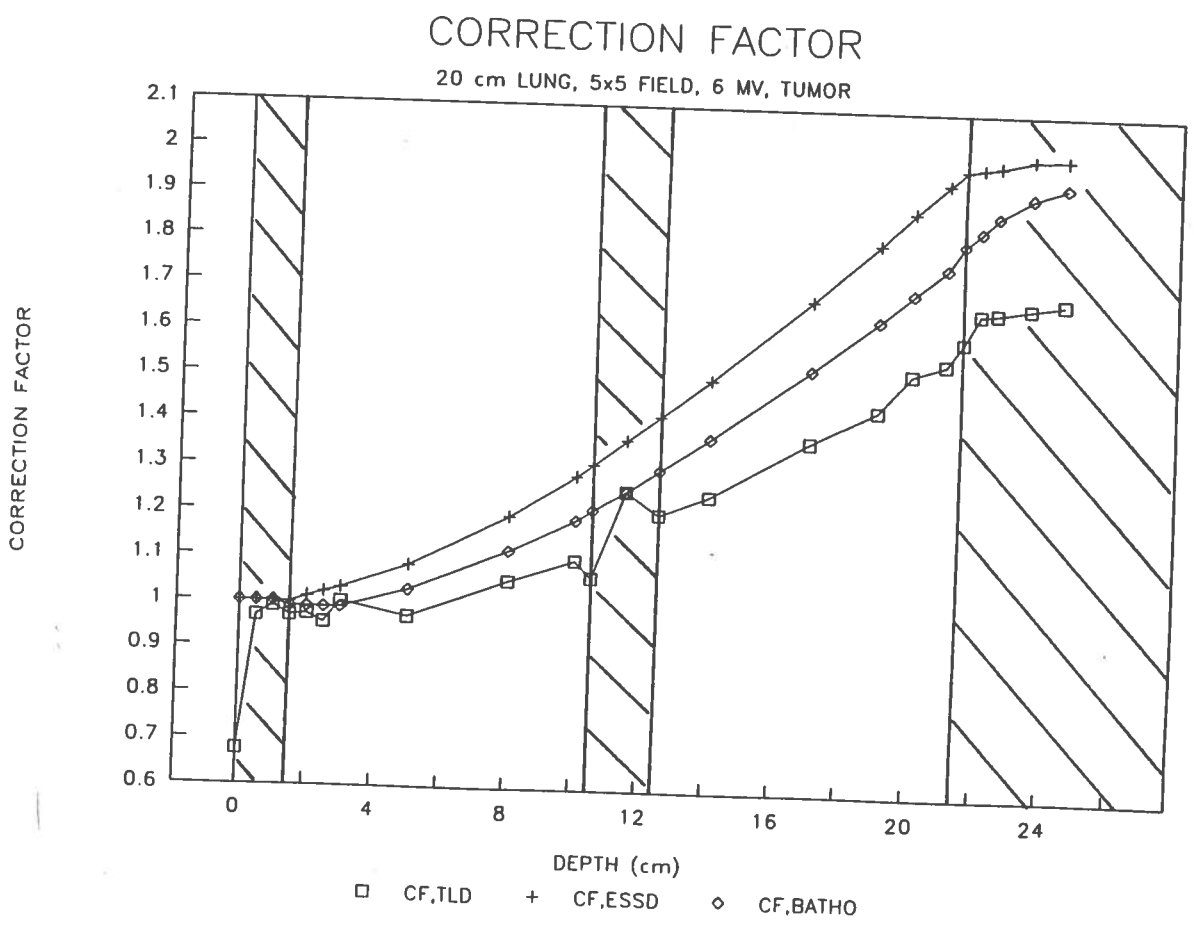

FIGURE A-27. **Measured and calculated correction factor for a 6 MV x-ray from a Clinac 600C for a 20 cm thick tumor lung phantom composed of cork with 1.5 cm overlay of build-up. The field size is 5 x 5 cm.**

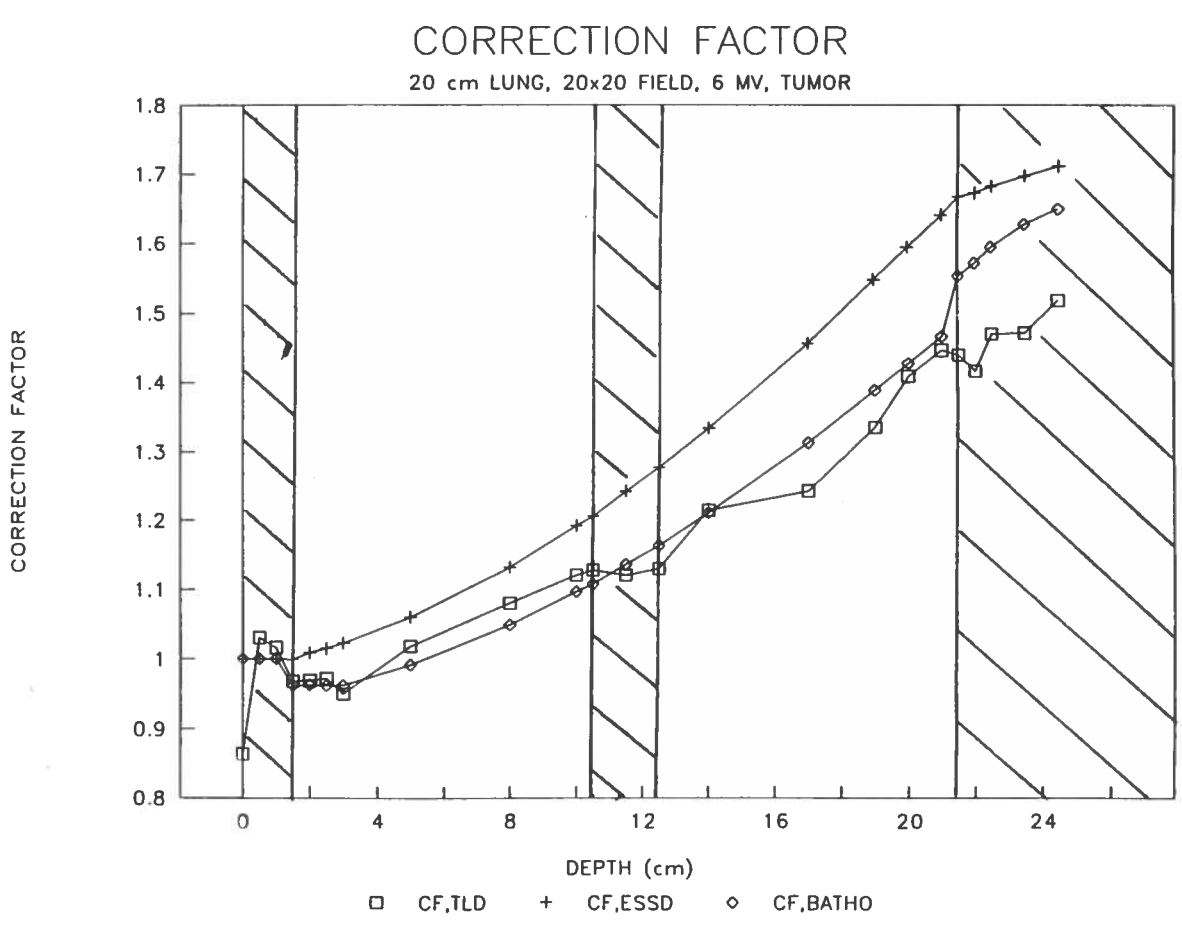

FIGURE A-28. **Measured and calculated correction factor for a 6 MV x-ray from a Clinac 600C for a 20 cm thick tumor lung phantom composed of cork with 1.5 cm overlay of build-up. The field size is 20 x 20 cm.**

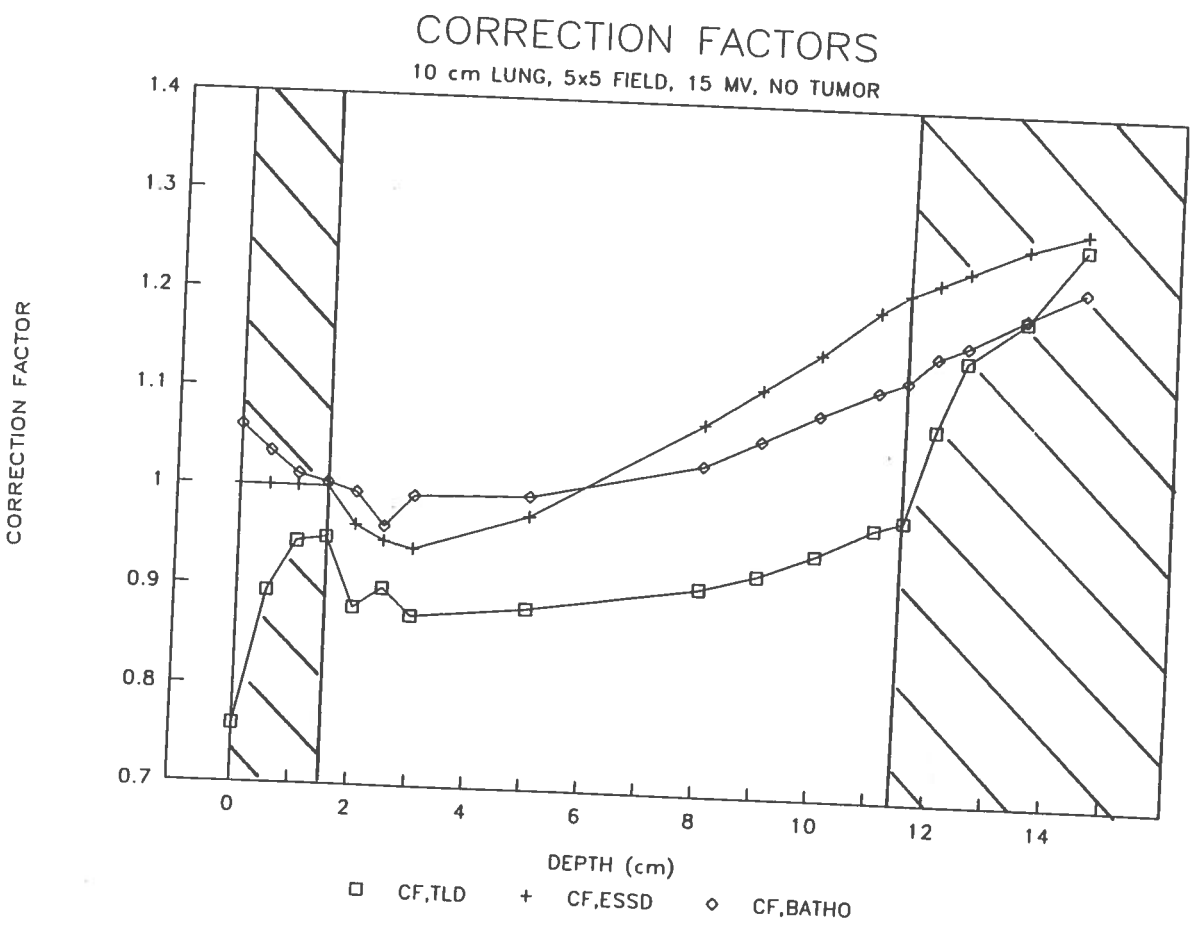

FIGURE A-29. **Measured and calculated correction for for a 15 MV x-ray from a Clinac 20 for a 10 cm thick non-tumor lung phantom composed of cork with 1.5 cm overlay of build-up. The field size is 5 x 5 cm.**

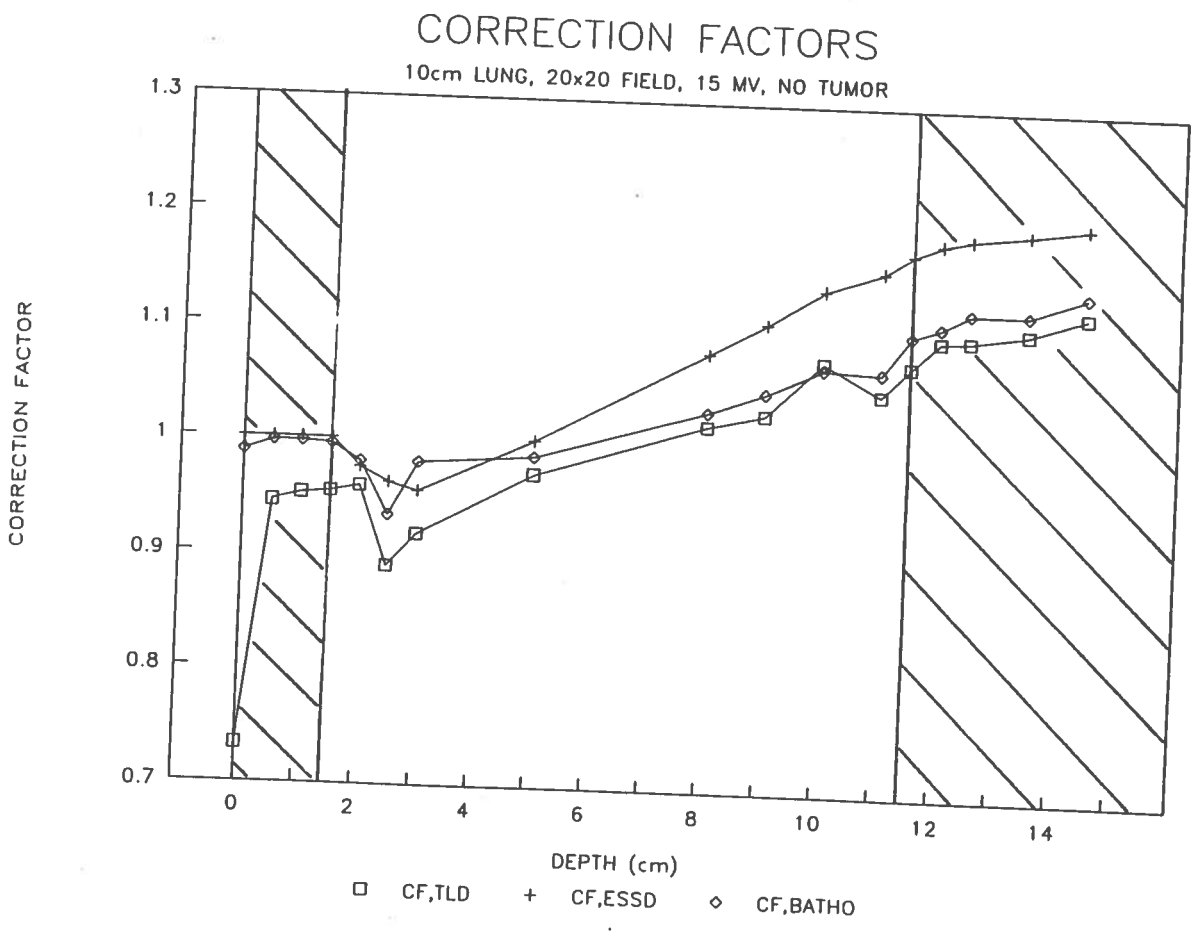

FIGURE A-30. **Measured and calculated correction factor for a 15 MV x-ray from a Clinac 20 for a 10 cm thick non-tumor lung phantom composed of cork with 1.5 cm overlay of build-up. The field size is 20 x 20 cm.**

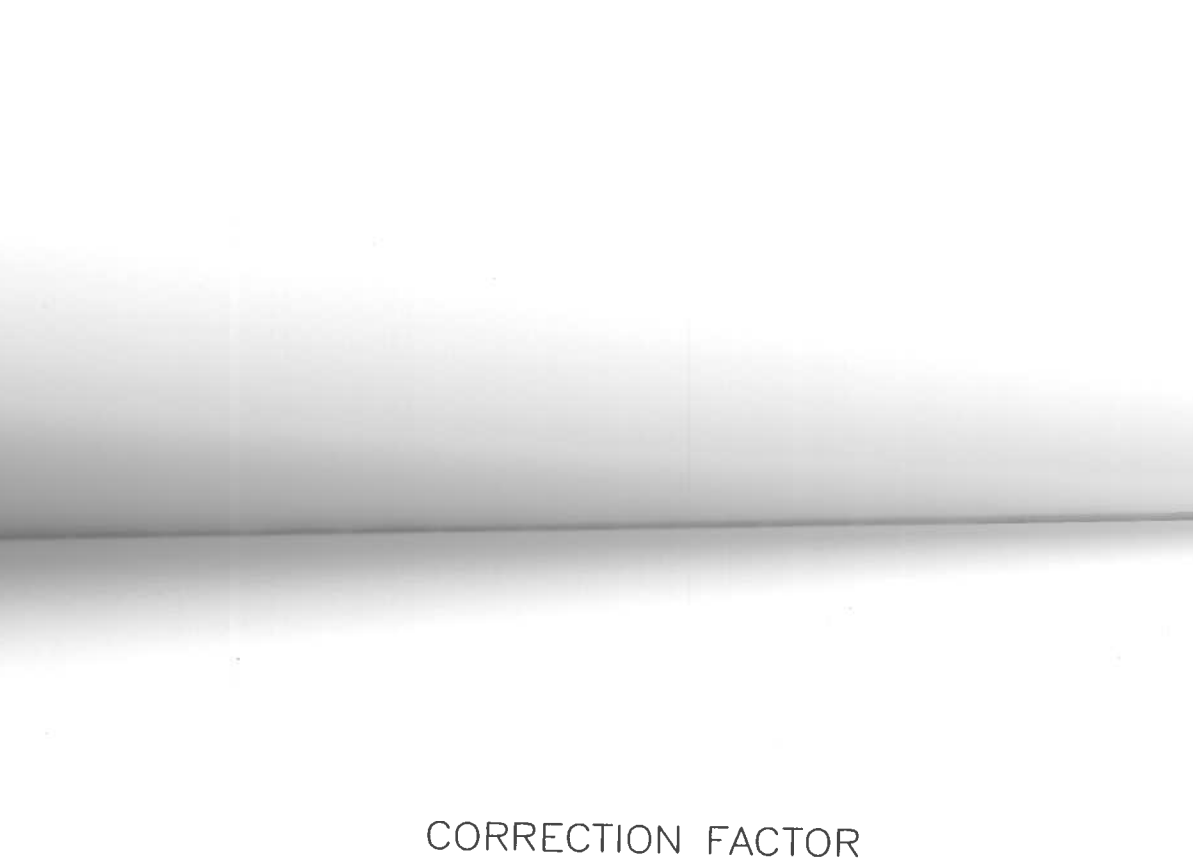

FIGURE A-31. **Measured and calculated correction factor for a 15 MV x-ray from a Clinac 20 for a 10 cm thick tumor lung phantom composed of cork with 1.5 cm overlay of build-up. The field size is 5 x 5 cm.**

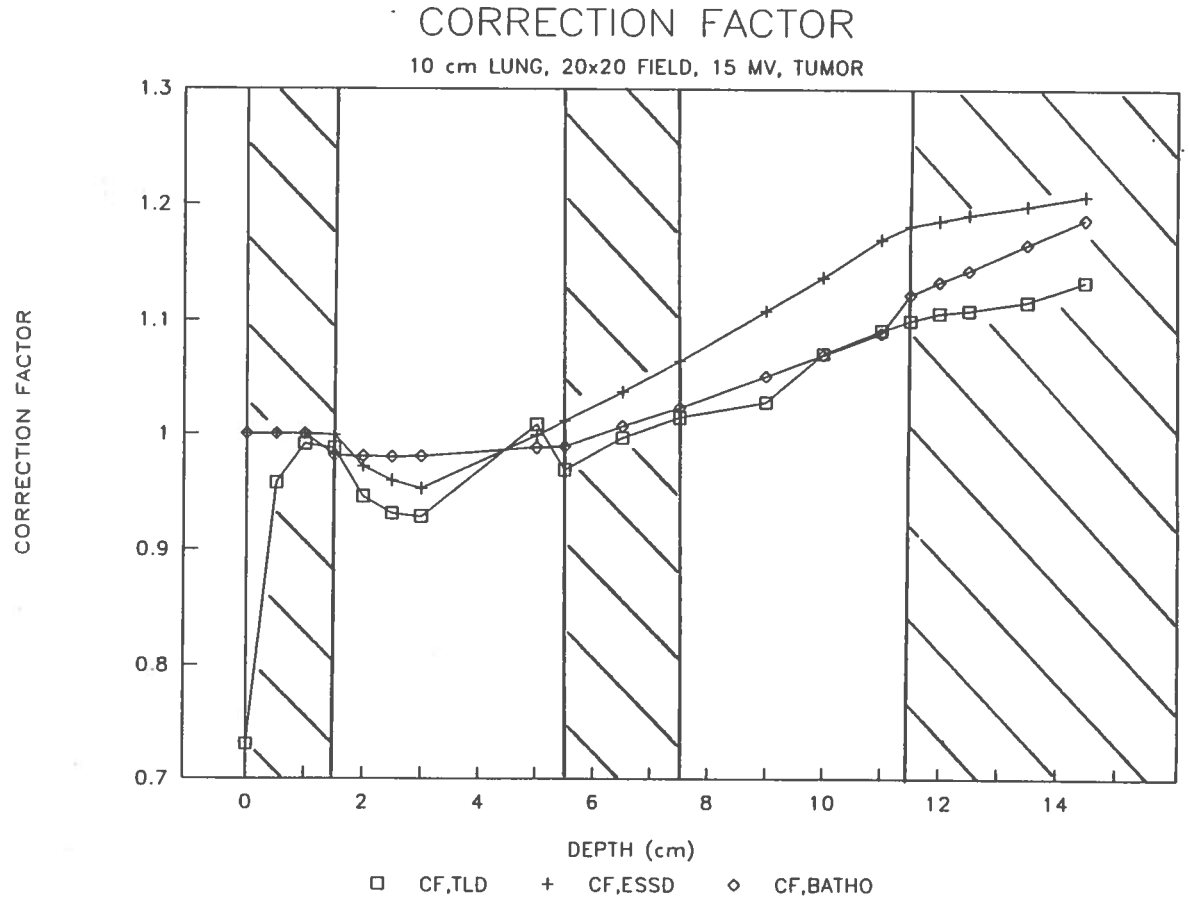

FIGURE A-32. **Measured and calculated correction factor for a 15 MV x-ray from a Clinac 20 for a 10 cm thick tumor lung phantom composed of cork with 1.5 cm overlay of build-up. The field size is 20 x 20 cm.**

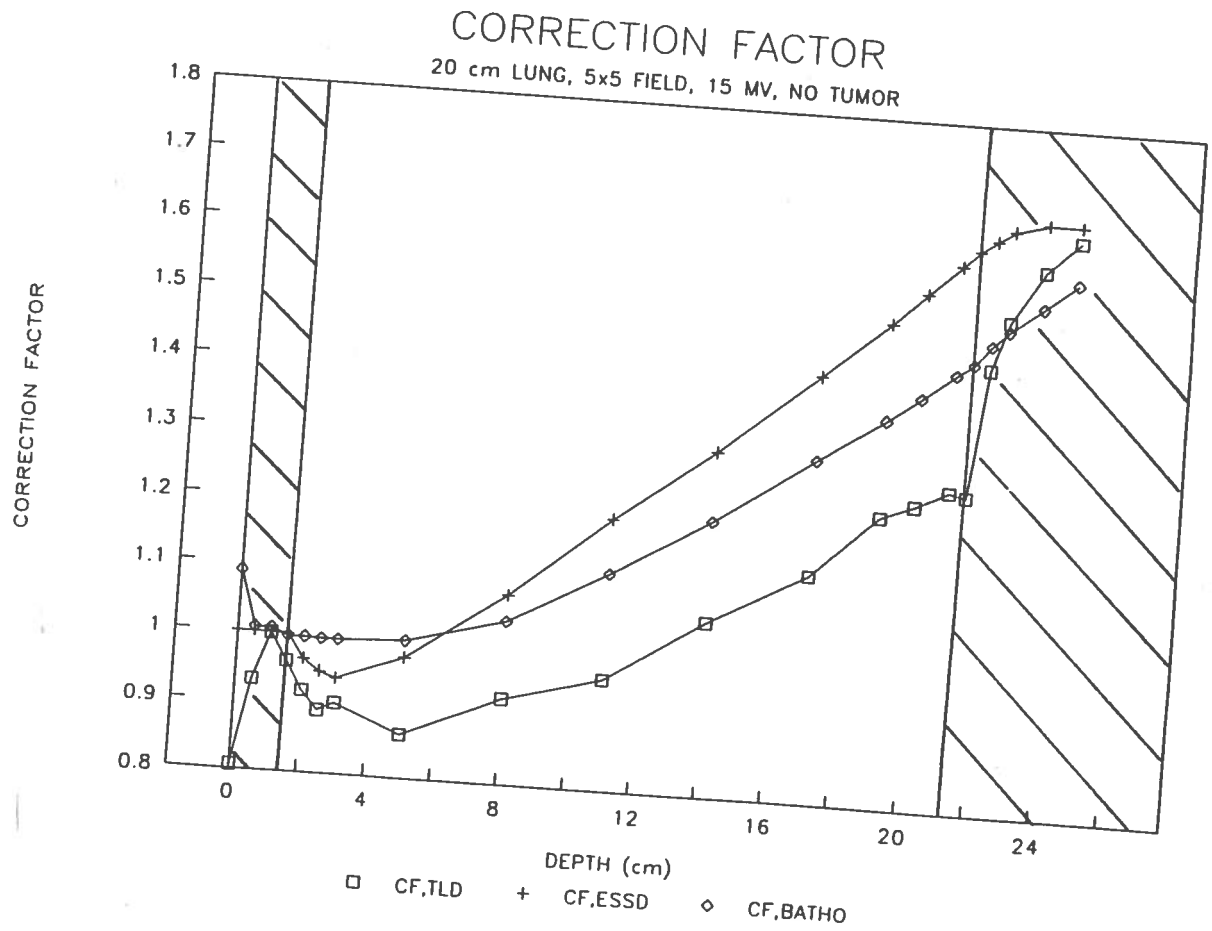

FIGURE A-33. **Measured and calculated correction factor for a 15 MV x-ray from a Clinac 20 for a 20 cm thick non-tumor lung phantom composed of cork with 1.5 cm overlay of build-up. The field size is 5 x 5 cm.**

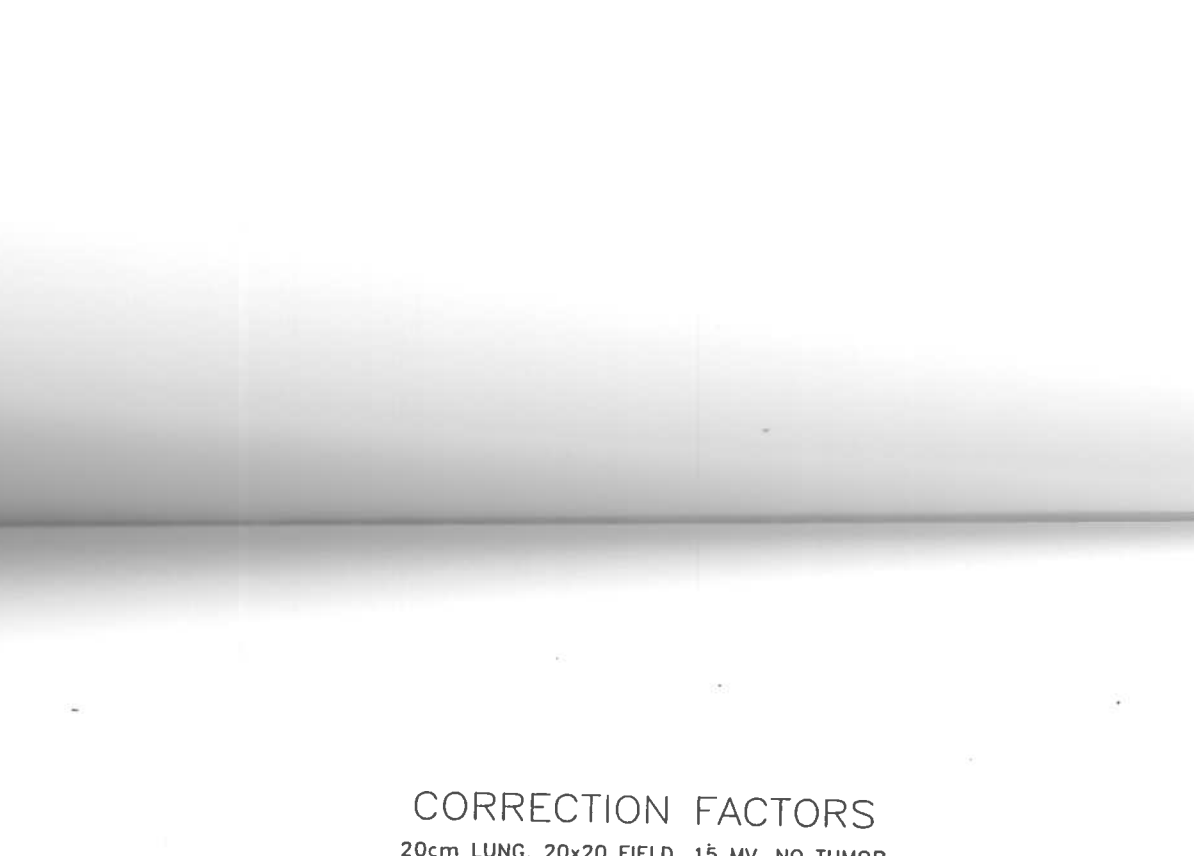

FIGURE A-34. **Measured and calculated correction factor for a 15 MV x-ray from a Clinac 20 for a 20 cm thick non-tumor lung phantom composed of cork with 1.5 cm overlay of build-up. The field size is 20 x 20 cm.**

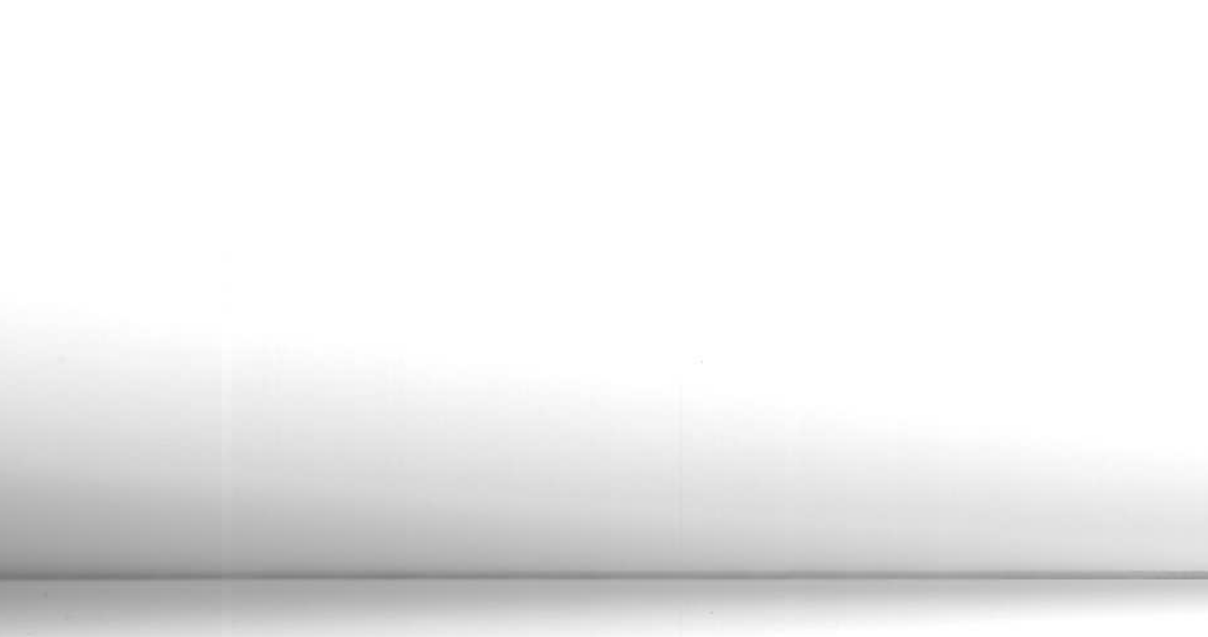

FIGURE A-35. **Measured and calculated correction factor for a 15 MV x-ray from a Clinac 20 for a 20 cm thick tumor lung phantom composed of cork with 1.5 cm overlay of build-up. The field size is 5 x 5 cm.**

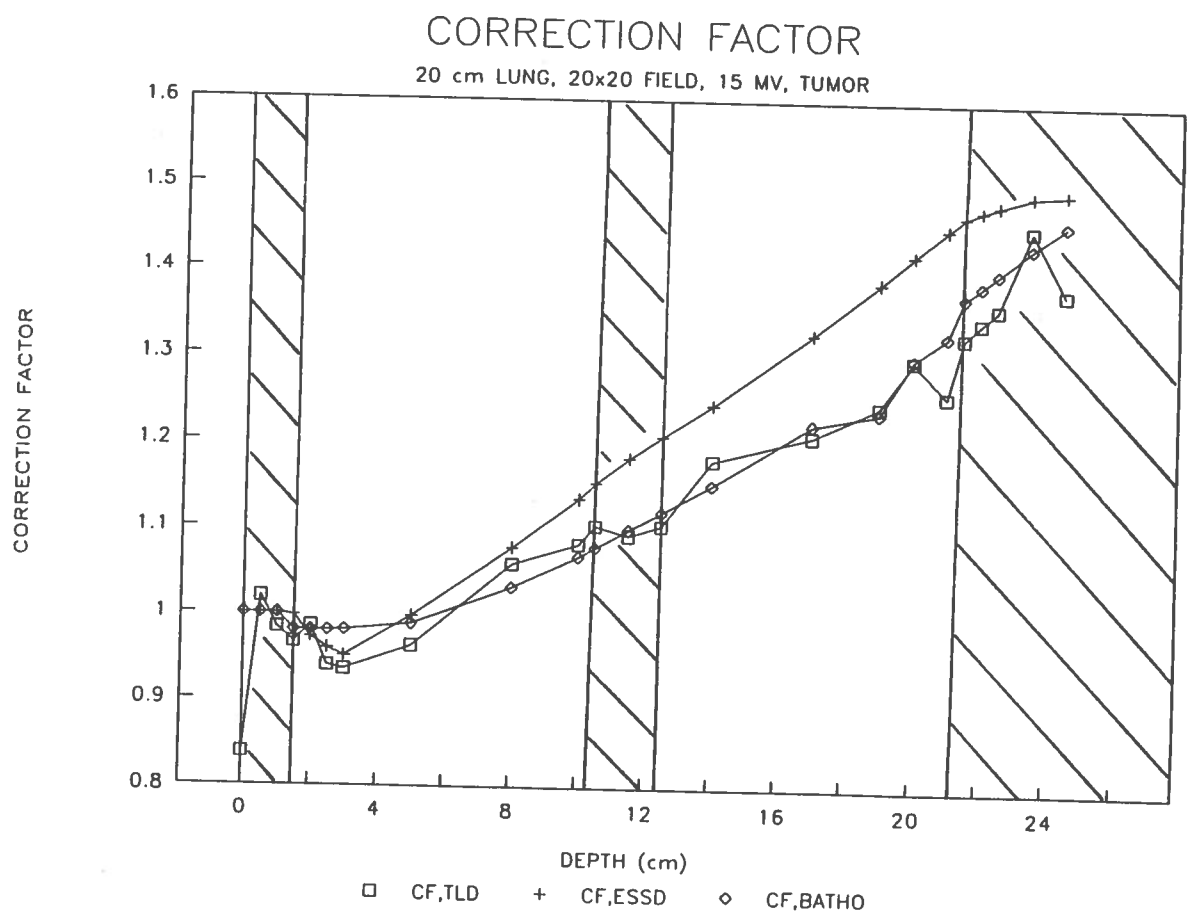

FIGURE A-36. **Measured and calculated correction factor for a 15 MV x-ray from a Clinac 20 for a 20 cm thick tumor lung phantom composed of cork with 1.5 cm overlay of build-up. The field size is 20 x 20 cm.**

APPENDIX B

TABLE B-1

Correction factor (CF) calculated for a 10 cm lung, 5 x 5 cm field, 6 MV x-rays by modified power law (MPL) algorithm at several points of depth. d is the physical depth, d_1 is the distance of the point of calculation to the front of the material, d_2 is the distance of the point of calculation to the front of the overlying material, d_b is the thickness of build-up used in this study.

		THOMAS ALGORITHM				
d (cm)	*CF (measured)*	$d_1 + d_b$	*Field Size (at depth)*	*TMR*	*CF (calculated)*	*RATIO Thomas/Measured*
5[a]	.988	5	5.25	.908	1.0855	1.0987
8[a]	1.104	8	5.4	.812	1.193	1.0806
10[a]	1.134	10	5.5	.745	1.284	1.1323
12.5[b]	1.299	$\frac{d_1 + d_b = 2.5}{d_2 + d_b = 12.5}$	5.6	$\frac{.98}{.67}$	1.3816	1.0636
13.5[b]	1.276	$\frac{d_1 + d_b = 3.5}{d_2 + d_b = 13.5}$	5.7	$\frac{.958}{.642}$	1.405	1.1011

[a]Inside the lung
[b]Beyond the lung

TABLE B-2

Correction factor (CF) calculated for a 10 cm lung, 10 x 10 cm field, 6 MV x-rays by modified power law (MPL) algorithm at several points of depth. d is the physical depth, d_1 is the distance of the point of calculation to the front of the material, d_2 is the distance of the point of calculation to the front of the overlying material, d_b is the thickness of build-up used in this study.

		THOMAS ALGORITHM				
d (cm)	*CF (measured)*	$d_1 + d_b$	*Field Size (at depth)*	*TMR*	*CF (calculated)*	*RATIO Thomas/Measured*
5[a]	.9535	5	10.5	.926	1.0675	1.1196
8[a]	1.089	8	10.8	.846	1.1528	1.0586
10[a]	1.1558	10	11.0	.795	1.2218	1.0571
12.5[b]	1.1533	$d_1 + d_b = 2.5$ / $d_2 + d_b = 12.5$	11.25	.985 / .722	1.3022	1.1291
13.5[b]	1.256	$d_1 + d_b = 3.5$ / $d_2 + d_b = 13.5$	11.35	.966 / .698	1.3181	1.0494

[a]Inside the lung
[b]Beyond the lung

TABLE B-3

Correction factor (CF) calculated for a 10 cm lung, 10 x 10 cm field, 6 MV x-rays by modified power law (MPL) algorithm at several points of depth. d is the physical depth, d_1 is the distance of the point of calculation to the front of the material, d_2 is the distance of the point of calculation to the front of the overlying material, d_b is the thickness of build-up used in this study.

		THOMAS ALGORITHM				
d (cm)	*CF (measured)*	$d_1 + d_b$	*Field Size (at depth)*	*TMR*	*CF (calculated)*	*RATIO Thomas/Measured*
5[(a)]	.995	5	21.0	.936	1.0578	1.0631
8[(a)]	1.044	8	21.6	.872	1.2358	1.1837
10[(a)]	1.101	10	22.0	.824	1.1789	1.0708
12.5[(b)]	1.125	$\frac{d_1 + d_b = 2.5}{d_2 + d_b = 12.5}$	22.5	$\frac{.986}{.765}$	1.2407	1.1028
13.5[(b)]	1.125	$\frac{d_1 + d_b = 3.5}{d_2 + d_b = 13.5}$	22.7	$\frac{.968}{.743}$	1.2521	1.1130

[(a)]Inside the lung

[(b)]Beyond the lung

TABLE B-4

Correction factor (CF) calculated for a 20 cm lung, 5 x 5 cm field, 6 MV x-rays by modified power law (MPL) algorithm at several points of depth. d is the physical depth, d_1 is the distance of the point of calculation to the front of the material, d_2 is the distance of the point of calculation to the front of the overlying material, d_b is the thickness of build-up used in this study.

		THOMAS ALGORITHM				
d (cm)	*CF (measured)*	$d_1 + d_b$	*Field Size (at depth)*	*TMR*	*CF (calculated)*	*RATIO Thomas/Measured*
8[a]	1.055	8	5.4	.815	1.1899	1.1279
14[a]	1.290	14	5.7	.626	1.489	1.1543
20[a]	1.620	20	6.0	.49	1.8337	1.1319
22[b]	1.703	$\frac{d_1 + d_b = 2}{d_2 + d_b = 22}$	6.1	$\frac{.99}{.452}$	1.9473	1.1435
23.5[b]	1.781	$\frac{d_1 + d_b = 3.5}{d_2 + d_b = 23.5}$	6.18	$\frac{.959}{.428}$	1.9853	1.1147

[a]Inside the lung

[b]Beyond the lung

TABLE B-5

Correction factor (CF) calculated for a 20 cm lung, 20 x 20 cm field, 6 MV x-rays by modified power law (MPL) algorithm at several points of depth. d is the physical depth, d_1 is the distance of the point of calculation to the front of the material, d_2 is the distance of the point of calculation to the front of the overlying material, d_b is the thickness of build-up used in this study.

		THOMAS ALGORITHM				
d (cm)	*CF (measured)*	$d_1 + d_b$	*Field Size (at depth)*	*TMR*	*CF (calculated)*	*RATIO Thomas/Measured*
8[a]	1.076	8	21.6	.872	1.1235	1.044
14[a]	1.237	14	22.8	.73	1.3067	1.0563
20[a]	1.436	20	24.0	.60	1.5437	1.075
22[b]	1.558	$\frac{d_1 + d_b = 2}{d_2 + d_b = 22}$	24.4	$\frac{.992}{.564}$	1.616	1.0372
23.5[b]	1.572	$\frac{d_1 + d_b = 3.5}{d_2 + d_b = 23.5}$	24.7	$\frac{.97}{.536}$	1.6556	1.0532

[a]Inside the lung

[b]Beyond the lung

TABLE B-6

Correction factor (CF) calculated for a 10 cm lung, 5 x 5 cm field, 15 MV x-rays by modified power law (MPL) algorithm at several points of depth. d is the physical depth, d_1 is the distance of the point of calculation to the front of the material, d_2 is the distance of the point of calculation to the front of the overlying material, d_b is the thickness of build-up used in this study.

		THOMAS ALGORITHM				
d (cm)	*CF (measured)*	$d_1 + d_b$	*Field Size (at depth)*	*TMR*	*CF (calculated)*	*RATIO Thomas/Measured*
5[a]	.883	6.3	5.25	.948	1.0464	1.1851
8[a]	.909	9.3	5.4	.875	1.1202	1.2325
10[a]	.946	11.3	5.5	.828	1.1740	1.2410
12.5[b]	1.149	$\frac{d_1 + d_b = 3.8}{d_2 + d_b = 13.8}$	5.6	$\frac{.996}{.772}$	1.2418	1.0808
13.5[b]	1.191	$\frac{d_1 + d_b = 4.8}{d_2 + d_b = 14.8}$	5.7	$\frac{.982}{.748}$	1.2603	1.0582

[a]Inside the lung

[b]Beyond the lung

TABLE B-7

Correction factor (CF) calculated for a 10 cm lung, 20 x 20 cm field, 15 MV x-rays by modified power law (MPL) algorithm at several points of depth. d is the physical depth, d_1 is the distance of the point of calculation to the front of the material, d_2 is the distance of the point of calculation to the front of the overlying material, d_b is the thickness of build-up used in this study.

		THOMAS ALGORITHM				
d (cm)	*CF (measured)*	$d_1 + d_b$	*Field Size (at depth)*	*TMR*	*CF (calculated)*	*RATIO Thomas/Measured*
5[a]	.972	6.3	21.0	.95	1.0446	1.0747
8[a]	1.018	9.3	21.6	.894	1.0999	1.0805
10[a]	1.076	11.3	22.0	.856	1.1413	1.0607
12.5[b]	1.098	$\frac{d_1 + d_b = 3.8}{d_2 + d_b = 13.8}$	22.5	$\frac{.993}{.814}$	1.1841	1.0794
13.5[b]	1.106	$\frac{d_1 + d_b = 4.8}{d_2 + d_b = 14.8}$	22.7	$\frac{.978}{.793}$	1.1951	1.0806

[a]Inside the lung

[b]Beyond the lung

VITA

Hasan Murshed was born on September 14, 1962, in Kishoregang, Bangladesh. He attended the Dhaka College, Bangladesh, and graduated in May, 1980. In 1987, he obtained a Bachelor of Medicine and Bachelor of Surgery from the Mymensingh Medical College & Hospital under the University of Dhaka. He practiced medicine for just under one year in Bangladesh. He entered graduate school and received a graduate assistantship in the Nuclear Science Center at Louisiana State University in August, 1989. In August, 1990, his assistantship duties and training were centered at Mary Bird Perkins Cancer Center. He is currently a candidate for the degree of Master of Science in Nuclear Science, Medical Radiation Sciences Option.

MASTER'S EXAMINATION AND THESIS REPORT

Candidate: Hasan Murshed

Major Field: Nuclear Science

Title of Thesis: Heterogeneity Dose Correction: A Dosimetric Analysis of External Photon Irradiation

Approved:

Oscar Hidalgo S.
Major Professor and Chairman

Kathleen de la Peña McCook
Dean of the Graduate School

EXAMINING COMMITTEE:

Ronald M Kruse

Carrie W. Ruddy

Gladden Johnson

Kenneth Lo

Date of Examination:

November 12, 1991